Transmission Electron Microscopy Characterization of Photovoltaic Semiconductor Materials

by

Allison Boley

A Dissertation Presented in Partial Fulfillment
of the Requirements for the Degree
Doctor of Philosophy

Approved April 2020 by the
Graduate Supervisory Committee:

David J. Smith, Co-Chair
Martha R. McCartney, Co-Chair
Jingyue Liu
Peter Bennett

ARIZONA STATE UNIVERSITY

May 2020

ABSTRACT

The research of this dissertation has primarily involved using transmission electron microscopy (TEM) techniques to study several semiconductor materials considered promising for future photovoltaic device applications.

Layers of gallium phosphide (GaP) grown on silicon (Si) substrates were characterized by TEM and aberration-corrected scanning transmission electron microscopy (AC-STEM). High defect densities were observed for samples with GaP layer thicknesses 250nm and above. Anti-phase boundaries (APBs) within the GaP layers were observed at interfaces with the Si surfaces which were neither atomically flat nor abrupt, contradicting conventional understanding of APB formation.

Microcrystalline-Si (*μc*-Si) layers grown on crystalline-Si (*c*-Si) substrates were investigated. Without nanoparticle seeding, an undesired amorphous-Si (*a*-Si) layer grew below the *μc*-Si layer. With seeding, the undesired *a*-Si layer grew above the *μc*-Si layer, but *μc*-Si growth proceeded immediately at the *c*-Si surface. Ellipsometry measurements of percent crystallinity did not match TEM images, but qualitative agreement was found between TEM results and Ultraviolet Raman spectroscopy.

TEM and Xray spectroscopy were used to study metal-induced crystallization and layer exchange for aluminum/ germanium (Al/Ge). Only two samples definitively exhibited both Ge crystallization and layer exchange, and neither process was complete in either sample. The results were finally considered as inconclusive since no reliable path towards layer exchange and crystallization was established.

Plan-view TEM images of indium arsenide (InAs) quantum dots with gallium arsenide antimonide (GaAsSb) spacer layers revealed the termination of some threading

dislocations in a sample with spacer-layer thicknesses of 2nm, while a sample with 15-nm-thick spacer layers showed a dense, cross-hatched pattern. Cross-sectional TEM images of samples with 5-nm and 10-nm spacer-layer thicknesses showed less layer undulation in the latter sample. These observations supported photoluminescence (PL) and Xray diffraction (XRD) results, which indicated that GaAsSb spacer layers with 10-nm thickness yielded the highest quality material for photovoltaic device applications.

a-Si/*c*-Si samples treated by hydrogen plasma were investigated using high-resolution TEM. No obvious structural differences were observed that would account for the large differences measured in minority carrier lifetimes. This key result suggested that other factors such as point defects, hydrogen content, or interface charge must be affecting the lifetimes.

This dissertation is dedicated to everyone who has shown me kindness during my physics journey thus far.

Put down the weight of your aloneness and ease into the

conversation. The kettle is singing

even as it pours you a drink, the cooking pots

have left their arrogant aloofness and

seen the good in you at last. All the birds

and creatures of the world are unutterably

themselves. [Everything, everything,]

everything is waiting for you

.

-excerpt from "Everything is Waiting for You" by David Whyte

ACKNOWLEDGEMENTS

This is my favorite section to write, because this dissertation is only possible because of the support of many whom I want to thank and acknowledge publicly.

Thank you to my sisters, Abby and Andrea, for embodying everything a sister should be.

Thank you to my parents and my late grandparents for creating an environment with a foundation of love in which hard work is valued, knowledge is fun, and girls can do anything.

Thank you to Kim de Beus for understanding me and being my unabridged friend.

Thank you to my fellow M&D Gang members – Dr. Lin Zhou, Dr. David Cullen, Dr. Kai He, Dr. Luying Li, Dr. Wenfeng Zhao, Dr. Lu Ouyang, Dr. Michael Johnson, Dr. JaeJin Kim, Dr. Dinghao Tang, Dr. Desai Zhang, Dr. Zhaofeng Gan, Dr. Xiaomeng Shen, Dr. Ajit Dhamdhere, Dr. HsinWei Wu, Dr. Majid Vaghayenegar, Dr. Jing Lu, Dr. Thomas McConkie, Dr. Brian Tracy, Dr. Sirong Lu, Dr. Abhinandan Gangopadhyay, Dr. Brandon McKeon, Scott Sherman, Dr. Sahar Hihath, Dr. Aram Rezikyam, Dr. Rajeev Reddy, Saiphaneendra Bachu, and Petr Mareš. You are my people, and it is with all of you that I found myself.

Thank you to Colleen Thompson, Jessica Robnett, Michaele Desmond, and Katie Schilling for your friendship and support across two decades and counting.

Thank you to Emily McConkie for keeping me sane with music and friendship.

Thank you to my extended family and friends for your words of encouragement and for understanding when I couldn’t be at every function.

Thank you to my students. Your character gives me strength.

Thank you to my supervisors and mentors at Glendale Community College, Chandler-Gilbert Community College, Benedictine University, and Mesa Community College for your guidance and encouragement.

Thank you to the CM200. I know what it's like to be sick all the time, and I'm thankful you didn't die before I graduated. Thank you to the FIB for allowing me to find great happiness in the act of scientific research.

Thank you to my collaborators (especially Dr. Joe Carpenter), my committee members, and the staff in the John M. Cowley Center for High Resolution Electron Microscopy for your invaluable practical help in accomplishing this work.

Finally, as the capstone of this section, thank you to the two people without whom this dissertation would certainly never have happened, Molly and Dave. In addition to the substantive help and guidance that led to this work, thank you for supporting me, giving me opportunities, allowing me to evolve, and sticking with me. I know how rare each of those is, much less all of them together, and I hope you know how grateful I am.

TABLE OF CONTENTS

Page

LIST OF TABLES………………………………………………………………. x

LIST OF FIGURES…………………………………………………………….... xi

CHAPTER

1 INTRODUCTION…………………………………………………………… 1

1.1 Importance of Photovoltaics…………………………………………… 1

1.2 Solar Radiation…………………………………………………………. 3

1.3 Physics of Materials……………………………………………………. 6

1.4 Physics of Photovoltaics………………………………………………... 8

1.5 Types of Photovoltaic Materials……………………………………….. 10

1.5.1 Silicon…………………………………………………………….. 12

1.5.2 III-V Materials……………………………………………………. 13

1.5.3 Multijunction Cells……………………………………………….. 13

1.5.4 Nanostructures……………………………………………………. 14

1.5.5 Organics…………………………………………………………... 15

1.5.6 Perovskites………………………………………………………... 17

1.6 Overview of Dissertation Research…………………………………….. 20

References…………………………………………………………………….. 23

2 EXPERIMENTAL METHODS……………………………………………… 26

2.1 Growth Methods………………………………………………………... 26

2.1.1 Plasma-Enhanced Chemical Vapor Deposition…………………... 26

2.1.2 Molecular Beam Epitaxy…………………………………………. 27

CHAPTER Page

2.1.3 Migration Enhanced Epitaxy………………………………………... 28

2.1.4 Stranski-Krastanov Growth………………………………………. 29

2.2 Sample Characterization Methods………………………………………. 29

2.2.1 Ellipsometry…………………………………………………… 29

2.2.2 Raman Spectrsocopy…………………………………………... 30

2.2.3 X-Ray Diffraction………………………………………………. 31

2.2.4 Photoluminescence…………………………………………….. 32

2.3 TEM Sample Preparation……………………………………………. 33

2.3.1 Focused-Ion Beam……………………………………………... 33

2.3.2 Polishing/ Dimpling/ Argon Ion Milling…………………………. 36

2.4 Transmission Electron Microscopy…………………………………….. 36

2.4.1 Fundamentals of TEM…………………………………………. 37

2.4.2 Scanning Transmission Electron Micrsocopy……………………. 39

2.4.3 Aberration-Corrected (S)TEM…………………………………… 40

2.4.4 Energy-Dispersive X-Ray Spectroscopy…………………………. 41

References………………………………………………………………….. 42

3 DEFECT AND INTERFACE CHARACTERIZATION IN GaP/Si HETEROSTRUCTURES……………………………………………………. 44

3.1 Introduction and Background…………………………………………... 44

3.2 Experimental Details…………………………………………………… 50

3.3 Results and Discussion………………………………………………… 51

3.3.1 Characterization of Defects………………………………………. 51

CHAPTER Page

3.3.2 Observation of Anti-Phase Boundaries………………………….. 55

3.4 Conclusions……………………………………………………….. 63

References………………………………………………………….. 66

4 MICROCRYSTALLINE Si FOR PASSIVATED Si SOLAR CELLS……… 68

4.1 Role of Microcrystalline Si in Si Heterojunction Solar Cells………….. 68

4.2 Growth and Characterization of Microcrystalline Si…………………… 69

4.3 Experimental Details…………………………………………………. 71

4.4 Results and Discussion………………………………………………. 71

4.5 Conclusions……………………………………………………….. 77

References………………………………………………………….. 79

5 Al-INDUCED CRYSTALLIZATION OF a-Ge AND LAYER EXCHANGE 80

5.1 Utility of Ge-Based Solar Cells and Metal-Induced Crystallization…… 80

5.2 Mechanisms of Metal-Induced Crystallization and Layer Exchange…... 81

5.3 Experimental Details…………………………………………………. 82

5.4 Results and Discussion………………………………………………. 83

5.5 Conclusions……………………………………………………….. 91

References………………………………………………………….. 92

6 InAs QUANTUM DOTS FOR INTERMEDIATE BAND SOLAR CELLS... 93

6.1 Introduction……………………………………………………….. 93

6.2 Experimental Details…………………………………………………. 96

6.3 Results and Discussion………………………………………………. 97

6.4 Conclusions……………………………………………………….. 100

CHAPTER Page

References…………………………………………………………………….. 101

7 INVESTIGATION OF PLASMA-ASSISTED Si SURFACE PASSIVATION……………………………………………………………………… 102

7.1 Introduction…………………………………………………………….. 102

7.2 Experimental Details…………………………………………………… 104

7.3 Results and Discussion………………………………………………… 105

7.4 Conclusions…………………………………………………………….. 112

References…………………………………………………………………….. 113

8 SUMMARY AND FUTURE WORK……………………………………... 114

8.1 Summary………………………………………………………………... 114

8.2 Future Work…………………………………………………………….. 117

8.2.1 Dilute Nitrides…………………………………………………. 117

8.2.2 Electron Holography Characterization of a-Si/c-Si………………. 120

References…………………………………………………………………….. 122

LIST OF REFERENCES………………………………………………………... 124

LIST OF TABLES

Table Page

3.1 Nominal and Observed Thicknesses for GaP Layers in MBE-grown GaP/Si Heterostructures………………………………………………. 51

3.2 Interface Widths Calculated from 10%-90% Intensity of S-curve Fits of HAADF Images of GaP/Si of 250nm GaP Layer……………………….. 59

5.1 Measured Thicknesses (Except Where Noted) of Al and Ge Layers, as well as Annealing and Oxidizing Conditions……………………………. 82

5.2 Ge Layer Crystallization as Observed by TEM and Layer Exchange as Observed by EDX……………………………………………………….. 91

LIST OF FIGURES

Figure		Page
1.1	Schematic Showing Different Avenues of Solar Energy Usage, Ranging from Radiation to End User……………………………………………	3
1.2	AM1.5 Solar Spectral Irradiance (red) Compared to an AM0 Spectrum at the Top of the Atmosphere (Yellow) and a Theoretical Blackbody Curve (Black Line)…………………………………………………………….	4
1.3	(a) A *p*-type Material and an *n*-type Material are Joined, Forming a *p-n* Junction. Electrons Diffuse Across the Junction, Forming (b) a Depletion Layer, which Produces an Electric Field. (c) This Electric Field Shows up as a Slope in a Simple Band Diagram. (d) In a Solar Cell, an Incoming Photon can Transfer the Energy Necessary for an Electron to be Excited From the Valence Band to the Conduction Band…………………………	5
1.4	Current-Voltage Curve (Bold) Showing Maximum Power Point………..	9
1.5	Band-Gap Energies and Lattice Constants of Common Semiconductors. Paths Between Compounds Represent Tertiary Compounds Composed of Incremental Percentages of the Elements of the Endpoints……………….	11
1.6	a) Record Efficiencies of Solar Cell Technologies. The Orange Circles Filled with Yellow Represent Perovskite Solar Cells. The Slope of the Progress of Perovskites is Clearly Greater than the Slope of Other Types of Solar Cells, Prompting Optimism in the Material. b) Magnified Region of a), Showing the Record Efficiency of Perovskite Solar Cells (22.1%) Compared to Si-Based Solar Cells Shown in Blue……………	18

Figure		Page

1.7 (a) Unit Cell of Perovskite Crystal Structure. A Represents the Organic Cation, B Represents the Metal Cation, and X Represents the Oxide or Halide Anion. (b) Schematic of Conventional Perovskite Solar Cell Structure……………………………………………………………………... 19

2.1 Schematic Diagram of Ellipsometry. An Incident Beam Passes through a Polarization Generator and Reflects from the Sample Surface. The Specularly Reflected Beam Passes through a Polarization State Analyzer Before Hitting the Detector………………………………………………. 30

2.2 a) Schematic Showing the Geometry of Electron and Ion Beams in a Dual-Beam FIB-SEM. A Sample on a Stage at Eucentric Height can be Tilted 52° for Ion-Beam Viewing if Required. b) Protective Platinum Bar Deposited on the Sample Surface. c) Sample after Material on Either Side of the Platinum Bar has been Trenched Away. d) Liftout Needle Approaching the Sample for *in-situ* Liftout. e) Specimen Mounted on a TEM Grid and Thinned to Electron Transparency……………………….. 34

2.3 Schematic Showing the Simplified Optics of TEM and STEM Systems. In Conventional TEM (CTEM), Electrons Proceed from Left to Right, from the Source to the Specimen, then through Objective and Magnifying Lenses to form the Final Image. In STEM, the Electrons Proceed from Right to Left, with the Source Demagnified by the Condensor and Objective Lenses to form the Small Probe on the Specimen Surface……………………………………………………… 39

Figure Page

3.1 Schematic of a Polar III/V Material, such as GaP, on a Diamond-Cubic IV Substrate, such as Si. Single, or Monoatomic, Steps Result in Polarity Reversal, which Leads to Anti-Phase Domains (APDs) Separated by APBs. The Si Diatomic Step Would Preserve the Polarity of the GaP Grown Above. The Left Side of the Figure Shows APBs Formed Along [111] Planes that Annihilate when they Intersect………………………… 46

3.2 XTEM Images of GaP/Si Samples with GaP Layer Thicknesses of: a) 37nm, b) 250nm, c) 1000nm, and d) 2µm……………………………….. 52

3.3 XTEM Images of the GaP/Si Interface of Samples with GaP Layer Thicknesses: a) 250nm, and b) 1000nm………………………………….. 53

3.4 DC ω-2θ RCs for Si Substrate and GaP Layer Thicknesses of: a) 37nm, 110nm, and 250nm; and c) 500nm, 1µm, and 2µm. TC ω RCs for: b) 37nm, 110nm, and 250nm; and d) 500nm, 1µm, and 2µm……………….. 54

3.5 a) Large-Angle BF STEM of GaP/Si Interface for Sample with GaP layer Thickness 37nm, b), c) DF STEM Images of Same Area, with GaP Polarity and Line Profiles along the Indicated Rows, d) DF STEM of Same Area with APB Location Indicated……………………………….. 56

3.6 a) HAADF Image of GaP/Si Interface for GaP Layer Thickness 250nm, b) Locations of Intensity Line Profiles with Average Shown in c) and Fitted to an S-curve. d) average intensity line profile across most of a), also fitted to an S-curve…………………………………………………... 58

Figure Page

3.7 HAADF Image of GaP/Si Sample Grown by MEE. In this Projection, the Si Surface was Nominally Flat. The GaP Layer was P-polar in all Observed Images.......... 61

3.8 HAADF Image of GaP/Si Sample Grown by MEE Showing the Si Surface Miscut by 4º in this Projection.......... 62

3.9 a) HAADF Image of GaP/Si Sample Grown by MEE. In this Direction, the Si Surface was Intentionally Miscut by 4º. b) and d) also Show Line Profiles which Reveal the GaP to be Ga-polar. The Line Profile in c) Shows a P-polar Region Near the Interface Followed by an APB Followed by a Ga-polar Region. e) Boxes that Contain APBs as Determined by the Method Shown in c). The Red Dashed Triangle in e) Indicates the Minimum Ratio of Horizontal to Vertical Distance of an APB in this Region, with the APB Given by the Hypotenuse of the Triangle.......... 64

4.1 Structures of (a) Typical SHJ Solar Cell,[3] and (b) Modified SHJ Solar Cell with a *μc*-Si (*p*+) Layer Replacing the *a*-Si (*p*+) Layer.......... 69

4.2 Laser Light Penetration Depths for Crystalline, Polycrystalline, Microcrystalline, and Amorphous Si as a Function of Wavelength. 532nm is the Customary Wavelength used in Raman Spectroscopy. However, due to the Reduced Penetration Depth, Light of Wavelength 325nm is more Appropriate to Probe Thin Films such as Those in this Study.......... 70

Figure Page

4.3 Microcrystalline Si Samples (a) A and (b) B, Grown on *a*-Si on *c*-Si. The C and Pt Layers were Deposited in the FIB to Protect the Surface………. 72

4.4 HRTEM Images of the μc-Si Layer of Samples (a) A and (b) B. Mulitple Nanocrystalline Grains, Some of which are Indicated by Yellow Arrows, are Visible above Amorphous Material…………………………………... 73

4.5 (a) Nominal Growth Structure and (b), (c) Cross-Sectional TEM Images of Sample D, with Nanoparticle Seed Layer to Induce Microcrystalline Growth Immediately at the *μc*-Si/*a*-Si Interface………………………….. 74

4.6 (a) UV Raman and Ellipsometry Measurements of Percent Crystallinity as a Function of Location Corresponding to (b) Cross-Sectional TEM Image of Sample C. UV Raman Spectroscopy Provides a Better Qualitative Match than Ellipsometry to the TEM Image………………… 76

5.1 Nominal Structure and TEM Image of as-Grown *a*-Ge/Al/SiO_2/Si Sample…………………………………………………………………. 83

5.2 (a) and (b) TEM Images of *a*-Ge/Al/SiO_2/Si Sample in Figure 5.1 After Annealing at 400ºC for 2 Hours. (c) STEM Image Showing Location of EDX Line Scan in (d). The Direction of the Arrow in (c) Indicates the Direction of the Scan, and the Black Line in (d) Marks the Position of the Red Dot in (c)……………….. 84

5.3 (a) XRD Scan of BEG 3A9 A30, Annealed at 400ºC for 4 Hours, and (b) TEM Image Showing Polycrystalline Ge Layer………………………….. 85

Figure Page

5.4 (a)-(c) EDX Line Profiles of Sample BEG3A9 A30 Taken at the Locations Indicated by the Arrows in (d) Dark-Field STEM Image. The Arrowheads Indicate the End of the Scan, and the Red Squares on the Arrows in (d) Indicate the Positions of the Black Lines in (a)-(c). The Initial Structure Before Annealing is Inset in (d)………………………… 86

5.5 (a) XTEM Image of Sample BEG2A8 A30, with Initial, Pre-Annealing Structure Inset. The Top Layers are Protective Carbon and Platinum Layers Deposited During Focused-Ion-Beam Sample Preparation. (b) XTEM Image of the Same Sample in a Different Lateral Location, where the Image Contrast is Different from that in (a)………………………….. 87

5.6 (a) HAADF Image of Thin Region of BEG2A8 A30, Indicating Layer Exchange, with the Exception of the Lighter Region within the Al Layer in the Red box. (b) An EDX Map of the Region in the Red Box in (a). Red Represents Ge, Green Al, and Blue O. The Lighter Region in the Al Layer in (a) is Shown by (b) to be an Al/Ge Mixture…………………….. 88

5.7 (a) and (b) HAADF Images of Sample BEG2A8 A30. The Z-Contrast Indicates that Layer Exchange is Incomplete in Some Regions………….. 90

6.1 Energy Diagram of an IBSC, with Possible Electronic Transitions Labeled by (1), (2), and (3)……………………………………………….. 94

6.2 Structure of Samples, with Varying Thicknesses of $GaAs_{0.83}Sb_{0.17}$ Spacer Layers…………………………………………………………………... 96

Figure Page

6.3 XRD TC ω RCs for: (a) GaAs Capping Layers, and (b) GaAsSb Spacer Layers of $GaAs_{0.83}Sb_{0.17}$/InAs QD Samples. The FWHMs of RCs of the Capping Layers in (a) Show Small Increases from 2-nm to 5-nm to 10-nm Spacer Layers, and a Dramatic Increase for the 15-nm Spacer Layer. The FWHM of the RC of the 10-nm Spacer Layer is the Smallest in (b)... 97

6.4 Plan-View TEM Images of $GaAs_{0.83}Sb_{0.17}$/InAs QD Samples with Spacer Layer Thicknesses of: (a) 2nm, and (b) 15nm……………………………. 98

6.5 XTEM Images of $GaAs_{0.83}Sb_{0.17}$/InAs QD Samples with Spacer Layers: (a) 5nm and (b) 10nm…………………………………………………….. 99

6.6 Integrated PL Intensities vs. Temperature for Multi-Stack QD Samples. Inset Illustrates Schematic Band Diagram for Type-II InAs/GaAsSb QD Structure…………………………………………………………………... 100

7.1 Carrier Lifetimes of Plasma-Treated *a*-Si/*c*-Si Samples. The Solid Red Circles Represent Samples with a SiO_x Capping Layer, and the Solid Black Squares Represent Samples with no Capping Layer. Samples a-e Circled in Blue Were Examined by TEM………………………………… 104

7.2 Diffraction-Contrast TEM Micrographs of Samples a and c-e. Samples d and e were Grown with an SiO_x Capping Layer, and Samples a and c were not. A Thin Layer can be Distinguished above the *c*-Si Surface before the *a*-Si Layer. The *c*-Si Surface of each Sample is Uneven, and the Local Regions Imaged in this Figure Show Greater Surface Roughness in Samples a and c Relative to Samples d and e……………... 106

Figure | Page

7.3 High-Magnification Images of Sample a, the Untreated Sample, Illustrating Local Variability in Surface Roughness……………………… 108

7.4 High Resolution XTEM Images of *a*-Si/*c*-Si Interface for Samples a-e. The *c*-Si Surface in each Sample is Uneven but Without Visible Defects, Indicating no Significant Differences Between the Crystalline Layers that Might Possibly Correlate with the Observed Differences in Carrier Lifetimes……………………………………………………………….. 109

7.5 Amorphous Si Layer Thicknesses of Samples a, c, and e. The Thickness is Greatly Reduced for Sample c. However, Sample e, with Minority Carrier Lifetimes the Same as for Sample c, has a Thickness Equal to the Nominally Deposited Thickness………………………………………….. 110

CHAPTER 1

INTRODUCTION

1.1 Importance of photovoltaics

Energy, primarily incident as solar radiation, enables life, and life is also enhanced by the energy that is used in artificial lighting, computers, air conditioning, transportation, and other technologies. As technology usage increases, so does the demand for energy. In the United States, total energy consumption in the residential sector increased by almost 3.5 times between 1950 and 2015. In the commercial sector, the increase was more than 4.5 times.[1] Moreover, the energy produced domestically in 2017 constituted only 89% of the energy consumed in the US, necessitating dependence on imported petroleum.[2] On a global scale, energy consumption is expected to increase by 48% from 2012 to 2040, especially in India and China,[3] and global energy production will need to keep pace with this consumption.

Renewable energy, which is obtained and used without depletion of the source, stands poised to halt the increase of economic, geopolitical, and environmental problems that are created by dependence on non-renewable energy sources.[4] Local harvesting of renewable energy creates jobs[5] and eliminates the possibility of international conflict over foreign sources of fossil fuels. Because such renewable energy sources as sunlight, wind, water, and heat from the earth are naturally occurring, they do not produce the toxic byproducts and global climate change caused by fossil fuels.[4]

In the Climate Action Plan, the Obama administration set the goal of doubling the United States' electricity generation from renewable energy sources between 2013 and 2020.[6] The Department of Energy responded to the President's challenge with an

emphasis on solar power. The DOE Office of Energy Efficiency & Renewable Energy requested a 2016 budget for solar energy technologies of more than $300 million, which was larger than that of wind, water, and geothermal projects combined.[7]

Solar energy possesses inherent advantages over other forms of renewable energy. The amount of energy in solar radiation incident on the surface of the earth is thousands of times greater than the amount of energy that humans consume.[8] Because of the (almost) global accessibility to sunlight, solar-powered devices enable access to life-saving and life-enhancing technology in regions where none previously existed. For example, portable solar cells enable such medical services as fetal Dopplers[9] and dental chairs in remote parts of the world.[10] The World Food Programme's Mobile Vulnerability Analysis and Mapping Initiative also harnesses solar power in remote villages to charge mobile phones that collect survey data related to food security.[11] Solar-powered lights provided relief to Puerto Rican survivors of Hurricane Maria when their power grid was destroyed.[12]

Technically, the sun is responsible even for fossil fuels, but direct collection of solar radiation can be divided into categories shown in figure 1.1. Primary products of solar energy include biomass, hydrogen, electricity, and heat. These, in turn, can be stored in batteries or storage tanks. Photovoltaics, which involves the direct conversion of photons to electricity,[13] is the subject of the research in this dissertation.

Despite drastic cutbacks proposed by the current U.S. administration,[14] utility-scale photovoltaics have already reached the 2020 goal of $0.06 per kilowatt-hour, with residential and commercial more than 85% of the way there.[15] Such competitive costs

make photovoltaics an economical, not just ecological, alternative to current energy sources.

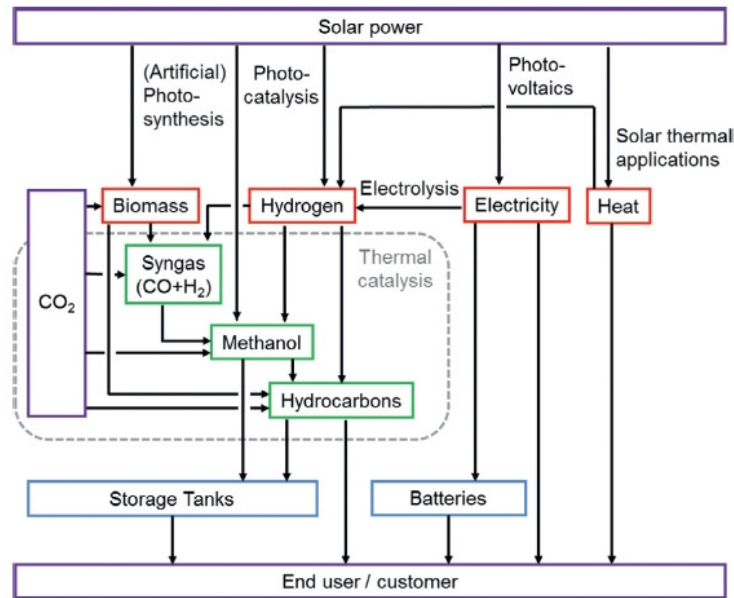

Figure 1.1: Schematic showing different avenues of solar energy usage, ranging from radiation to end user.[13]

1.2 Solar radiation

The relevant physics of solar radiation includes blackbody radiation and wave-particle duality. The sun is the classical real-world approximation of a blackbody, which is an object that emits electromagnetic radiation at all wavelengths. The temperature of a blackbody determines the distribution of emitted wavelengths: at 5760K, the sun emits primarily in the infrared, visible, and ultraviolet regions of the electromagnetic spectrum.[16] Atmospheric constituents absorb solar radiation at characteristic wavelengths, so that sunlight reaching the earth's surface is reduced from the ideal blackbody curve.[17] The extent of this reduction depends on how far the light travels through the earth's

atmosphere, and is identified by the quantity air mass (AM). Air mass is given by the expression

$$n_{AirMass} = \frac{optical\ path\ length\ to\ the\ sun}{optical\ path\ length\ if\ sun\ is\ directly\ overhead} \tag{1.1}$$

where n_{AirMass} is an index used for convenience in labeling spectra of various air mass.[16] The standard AM1.5 (n_{AirMass}=1.5) corresponds to sunlight traveling through the atmosphere when the sun is at an angle of elevation of 42º.[16] The extraterrestrial AM0 spectrum is approximated by the yellow area of Figure 1.2, and an AM1.5 spectrum by the red area.[17]

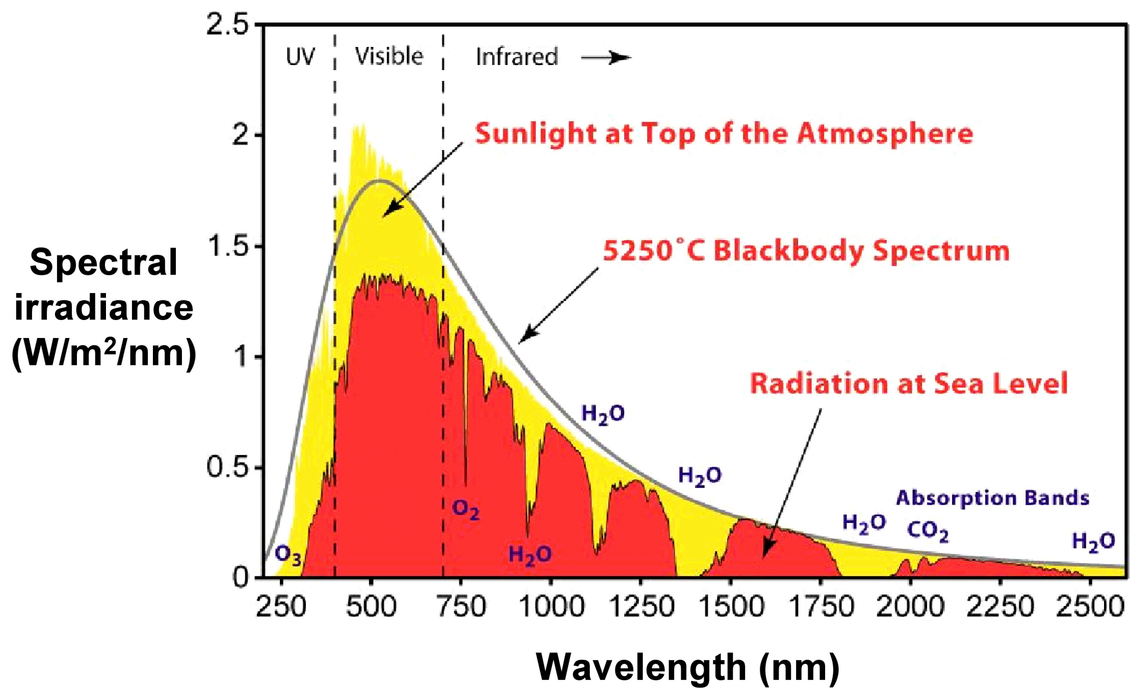

Figure 1.2: AM1.5 solar spectral irradiance (red) compared to an AM0 spectrum at the top of the atmosphere (yellow) and a theoretical blackbody curve (black line).[17]

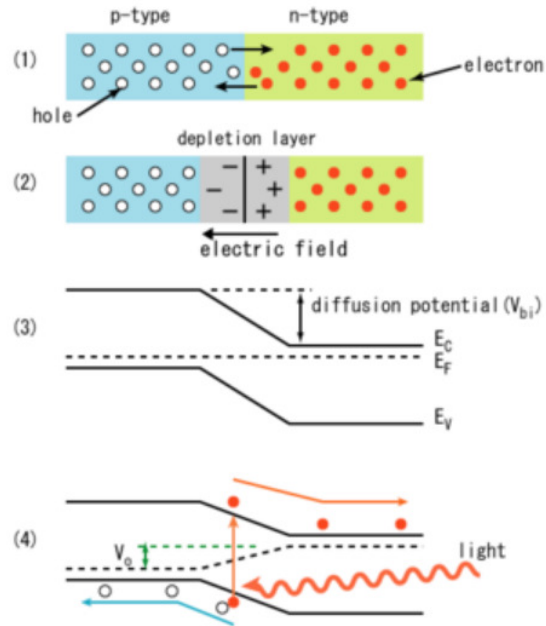

Figure 1.3: (a) A *p*-type material and an *n*-type material are joined, forming a *p*-*n* junction.[20] Electrons diffuse across the junction, forming (b) a depletion layer, which produces an electric field. (c) This electric field shows up as a slope in a simple band diagram. (d) In a solar cell, an incoming photon can transfer the energy necessary for an electron to be excited from the valence band to the conduction band.

Light from the sun exhibits wave-particle duality and thus it exhibits the properties of both waves and particles. As a wave, light is governed by wave optics. At a boundary between two media, light is reflected and transmitted according to the reflection and transmission coefficients, respectively, both determined by the indices of refraction of the media on either side of the boundary.[18] Maximizing absorption of light and minimizing its transmission out of a solar cell is an important consideration in solar cell design, [19] as is maximizing the internal reflection of light within the cell. As a particle, light is composed of photons, or discrete packets of electromagnetic energy. A photon

has no mass, but does have momentum and energy that is inversely proportional to its wavelength. When this energy is equal to or slightly greater than the difference between energy levels of a single atom or the band gap of a semiconductor, the photon can excite electrons from one level or band to another, leaving behind a positively-charged hole, as shown in figure 1.3d.[20] This generation of electron-hole pairs, also known as excitons, represents the foundation of photovoltaic technology.[21]

1.3 Physics of materials

Designing materials for photovoltaic use requires careful consideration of materials properties in order to ensure maximum efficiency.

In order to absorb the maximum number of photons, as required to increase short circuit current density, and consequently cell efficiency, the absorption coefficient is important. This material- and wavelength-dependent parameter provides a measure of the average thickness at which incident light is absorbed. The larger the absorption coefficient, then the greater is the probability of absorbing light, and thus the depth at which the incident light is absorbed is also smaller.[22] If light is absorbed in a layer where the material properties result in recombination of electron-hole pairs, then the wavelength of light corresponding to that layer is less likely to contribute to the quantum efficiency of the cell.[23]

Recombination, which is detrimental to the short circuit current and open circuit voltage of a solar cell, can result from several material factors. The three main types of recombination are radiative, Shockley-Reed-Hall (SRH), and Auger. Radiative recombination is the reverse of the fundamental mechanism of photovoltaic energy

generation as illustrated in figure 1.3: the electron falls back to the valence band from the conduction band, recombining with a hole and emitting a photon.[24]

Shockley-Read-Hall (SRH) recombination occurs because of a "trap" with energy in between the valence and conduction bands. Recombination may occur within the trap, or the trap may facilitate recombination in the valence band by electron capture, the process of an electron deexciting from the conduction band to the trap, when it can again de-excite to the valence band.[25] Traps that enable SRH recombination can be created by defects within the material. One important source of defects is lattice mismatch between materials. Each material in a crystal has a characteristic lattice parameter, which is a measure of the separation of its constituent atoms.[26] When one material is grown on another, the first few atomic layers may be stretched or compressed to match the lattice constant of the underlying layer, known as pseudomorphic growth. As the thickness of the upper layer increases, the strain is relaxed and defects will be formed.[27]

In Auger recombination, when electrons and holes recombine, instead of energy being released in the form of radiation as for radiative recombination, the energy is transferred to another carrier. In highly doped or small band-gap materials, Auger recombination is a significant factor contributing to shorter carrier lifetimes.[28]

Another important factor in the physics of photovoltaic materials is whether the band gap is direct or indirect. For materials with a direct band gap, the conduction band minimum is directly above the valence band maximum, meaning that the material only needs to absorb a photon in order to excite an electron. In materials with an indirect band gap, the valence band maximum and conduction band minimum are offset, requiring

absorption of a photon and a phonon. A disadvantage of materials with an indirect band gap is that the absorption coefficients are small, thus requiring larger thicknesses.[28]

1.4 Physics of photovoltaics

The fundamental mechanism of photovoltaic energy generation is relatively straightforward, as shown in figure 1.3: an incoming photon from the sun incident on a semiconductor material excites a valence band electron to the conduction band, simultaneously creating a hole in the valence band. When the semiconductor contains a *p-n* junction, then charge separation occurs. Connection to an external circuit allows energy to be stored, and work can then be done.[29] The probability that an electron will be excited by an incoming photon and used to do work is known as the quantum efficiency, which depends on the photon wavelength and on the materials that form the *p-n* junction.[16]

On the macro-scale, the cell efficiency, or power conversion efficiency, measures the percent of incoming power from sunlight that is utilized. To calculate this performance metric, short circuit current density and open circuit voltage are measured.[16] Open circuit voltage is the voltage measured across the terminals of the cell, and short circuit current is the current measured in series with the cell, both with no additional circuit components connected. Short circuit current density is short circuit current per unit area. The short circuit current is maximized when the absorption of photons above the band gap and the quantum efficiency are both maximized. The open circuit voltage is maximized when the dark current is minimized. Recombination of electrons and holes decreases both short circuit current and open circuit voltage.[30]

In a real cell, the maximum power point, identified on a sample current-voltage curve as shown in figure 1.4, is reduced from the idealized product of the short circuit current and open circuit voltage.[16] The extent of this reduction is measured by the fill factor: the actual maximum power point, identified in figure 1.4, divided by the product of short circuit current and open circuit voltage.[28] The ratio of the maximum power density of the cell to the power density of incoming solar radiation is the cell efficiency, or power conversion efficiency, which differs from the cell quantum efficiency described earlier.[16] In terms of the fill factor, the power conversion efficiency (η) is given by

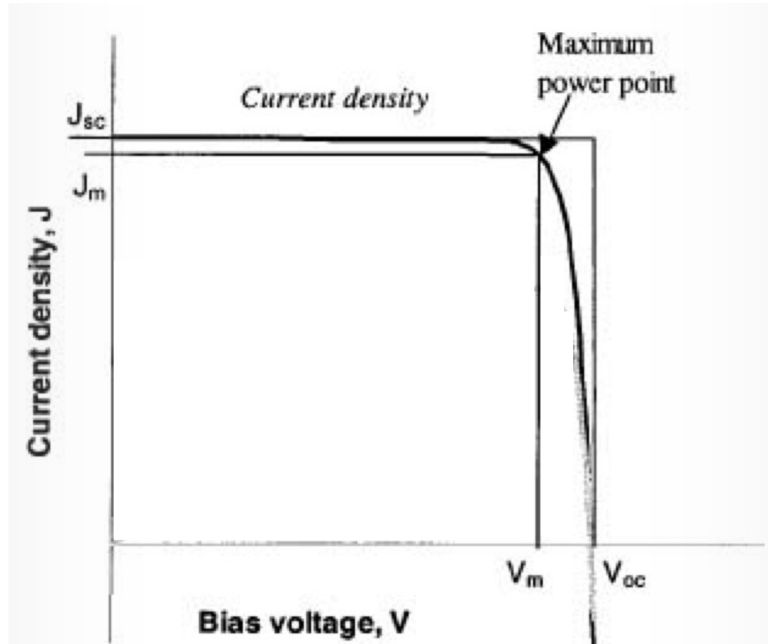

Figure 1.4: Current-voltage curve (bold) showing maximum power point.[16]

$$\eta = \frac{FF \times J_{SC} \times V_{OC}}{P_{in}} \quad (1.2)$$

where FF is the fill factor, J_{SC} is the short circuit current, V_{OC} is the open circuit voltage, and P_{in} is the incoming power from solar radiation.[28]

The maximum theoretical power conversion efficiency of a solar cell can be calculated via the method known as "detailed balance" developed by Shockley and Queisser.[31] The Shockley-Queisser efficiency approximates the Sun and a *p-n* junction solar cell as blackbodies, and takes all radiative flux into account. It assumes that the

blackbody radiation from the cell is due to radiative recombination, so non-radiative recombination is not considered. The detailed balance depends on the temperatures of the blackbodies and on the band gap of the solar cell. Shockley and Queisser calculated the maximum efficiency of a 1.1eV band-gap solar cell under one Sun approximated as a blackbody to be 30%,[31] and other workers have used the same approach to understand the maximum efficiency limits for other material combinations.[32]

1.5 Types of photovoltaic materials

Any serious discussion of collecting and utilizing energy from the sun must recognize that nature successfully accomplished this task via photosynthesis, literally millions of years before human-engineered technology. While the mechanism of photovoltaic energy generation differs from photosynthesis, there are some similarities. For example, chlorophyll, which absorbs certain wavelengths of sunlight plays a role in genetic engineering.[33] Similarly, the band-gap energies of solid-state photovoltaic materials can be tuned to match the predominant photon energies of the incident solar spectrum.

Such band-gap engineering is achieved primarily by suitable combinations of materials and/or nanostructures. Figure 1.5 shows the lattice constants and band-gap energies of common semiconductors.[34]

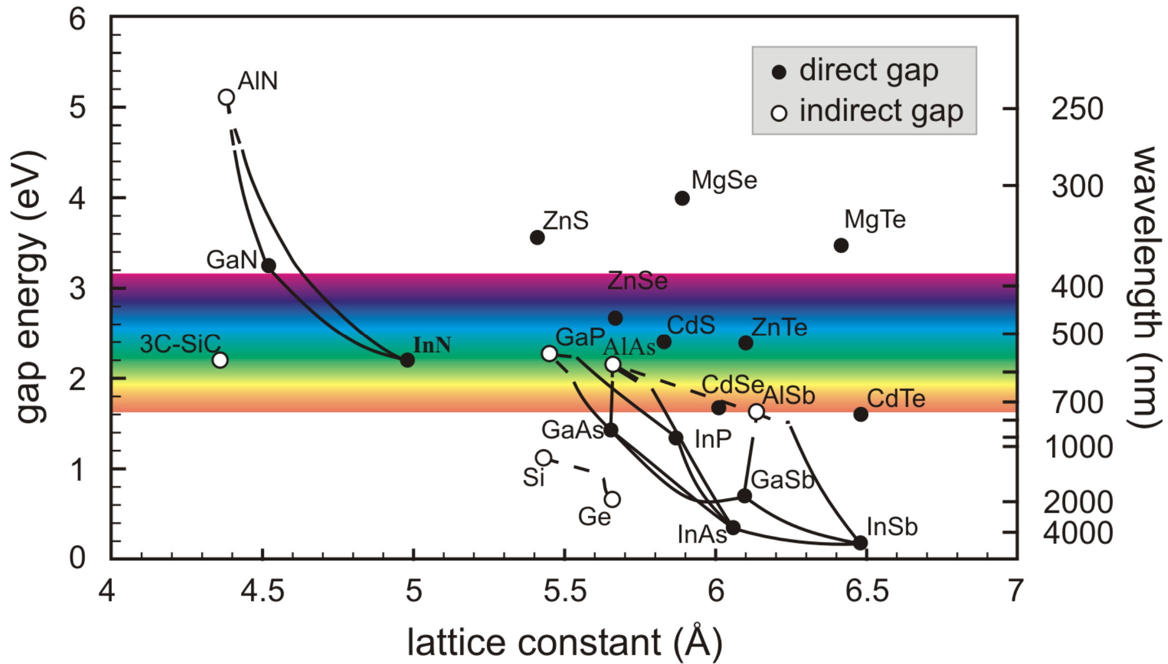

Figure 1.5: Band-gap energies and lattice constants of common semiconductors. Paths between compounds represent tertiary compounds composed of incremental percentages of the elements of the endpoints.[34]

For a solar cell, the most desirable band gaps are in the region of the electromagnetic spectrum where the sun emits the most photons. As can be seen from the peak of the blackbody curve in figure 1.2, this corresponds to the visible light region. The visible spectrum is denoted in figure 1.5 by the horizontal rainbow. The horizontal axis shows lattice constant. As discussed in section 1.3, it is desirable to pair semiconductors with similar lattice constants, directly above each other in figure 1.5, to avoid electron-hole pair recombination associated with defects. For example, the lattice mismatch between GaP and Si is 0.36%, so that GaP growth on Si should be promising as an approach to achieve low defect density.

1.5.1 Silicon

The first crystalline Si (*c*-Si) solar cell was created in 1955,[35] and Si continues to dominate the global photovoltaic market.[36] A typical Si solar cell consists of a thick *p*-type Si layer sandwiched between a thin *n*-type Si layer and a thin *p*+-type Si layer. These latter layers are both passivated with amorphous Si. The top surface is covered with a textured antireflective coating, and both surfaces are connected to metal contacts.[37] The current 25.8% laboratory record efficiency of *c*-Si without a concentrator[38] is close to the Shockley-Queisser limit of ~29%. However, while improvements in manufacturing have raised efficiencies of industrial panels to near 20%, diminishing returns have steered research to other materials as well as multijunction cells to yield greater efficiency.[35]

Amorphous Si (*a*-Si) has the advantage over *c*-Si of being a direct band-gap material, and an *a*-Si *p*-*i*-*n* junction, passivated via hydrogenation, can form another type of solar cell.[37] The efficiency of such cells is low, with an eventual goal of 15%, and there are degradation issues that reduce long-term stability. However, the ability to use thinner layers of *a*-Si rather than *c*-Si means that cost and energy payback time are less than for *c*-Si. Moreover, *a*-Si can be grown on flexible substrates.[35]

Nanocrystalline Si (*nc*-Si) has demonstrated higher efficiency than *a*-Si as well as less degradation.[35] Although the growth process is still a subject of investigation, *a*-Si/*nc*-Si cells are already on the market. For both *a*-Si and *nc*-Si, there is potential for significant improvements in efficiency before the Shockley-Queisser limit is reached. Challenges include reduction of crystalline defects as well as increases in carrier mobility.[34]

1.5.2 III-V Materials

GaAs is the III-V material most widely used in solar cells, and record efficiencies of these cells surpass those of Si.[38] The advantages of GaAs over Si include a direct band gap, increased electron mobility, and higher breakdown voltage. The band gap (1.42eV) is also closer to the optimal single-junction solar cell for collecting AM1.5 radiation (1.34eV) than Si (1.12eV). Conversely, GaAs is more expensive and more difficult to grow than Si. Thus, GaAs solar cells lag well behind Si solar cells in industrial production.[8] A typical GaAs cell has the same basic structure as a *c*-Si cell, just with the different material.[36]

Tertiary III/V materials are often grown to tune both the band gap and the lattice constant.[8] The curved lines connecting binary materials in Figure 1.5 represent the band gaps and lattice parameters of tertiary compounds of varying composition.[36] For example, the curve between InAs and InSb represents $InAs_xSb_{1-x}$, where x decreases with movement towards the right on the curve.

Anti-phase domains are a major problem associated with growth of III/V materials. In the case of Si, there is only one type of atom occupying each site in the crystal lattice. However, replacing two atoms of Si with one partially positive atom and one partially negative atom results in crystal polarity within the structure. Anti-phase domains are formed when the polarity within the material switches during growth, and the location of the plane is known as an anti-phase boundary.[39]

1.5.3 Multijunction cells

Regardless of material, solar cells composed of a single *p-n* junction are limited because they can only absorb radiation with energies that are equal to or greater than the

band gap of the material.[8] To collect a larger range of the solar spectrum, it is necessary to stack multiple materials with different band gaps. Such multijunction solar cells (MJSCs) exceed the power conversion efficiency of single-junction solar cells and have already found a place in the market.[40]

In multijunction cells, different materials are grown one on another. A common goal in heteroepitaxial growth is to match lattice constants as closely as possible in order to minimize the formation of material defects which lead to recombination. Alternatively, metamorphic growth allows for optimizing combinations of band gaps, regardless of lattice mismatch.[41] Materials are grown separately and then combined afterwards, or grown together with the aid of buffer layers.[42] Whether lattice-matched or metamorphic, the material with the largest band gap should be located closest to the front surface of the cell, with decreasing band gaps at increasing distance below the surface. This order of materials is due to the inverse relationship between energy and absorption depth, as described by the absorption coefficient.[36]

Since these junctions are connected in series, reduction in the efficiency in one junction negatively impacts the entire device.[41] The technique known as "current matching" seeks to optimize material parameters, with the goal of generating and mobilizing the same number of carriers in each junction.[8]

1.5.4 Nanostructures

Although the properties of the photovoltaic materials discussed so far originate at the nanoscale, decreasing the sizes of the active materials results in nanostructures which often have different properties from the bulk materials. These differences arise in part because the number of atoms decreases, and the resulting band structure then exhibits

narrower bands and wider band gaps. Another consequence of reduced size is the increased surface area to volume ratio. One major advantage of this ratio is a decreased distance for electron-hole pairs to travel, leading to increased carrier collection. However, a major disadvantage is that more dangling bonds at the surfaces act as recombination centers.[14] From a cost standpoint, another advantage is that, similar to thin films, nanostructures use less material than traditional bulk Si cells.[19]

Nanostructures investigated for potential photovoltaic applications include nanopillars, nanowires, nanorods, nanocones, and quantum dots.[14] The first four types are considered one-dimensional structures. In addition to improved carrier collection, they minimize reflection and maximize absorption of photons due to their shapes.[19] Quantum dots are considered zero-dimensional structures and are being investigated because their intermediate bands, located between the valence and conduction bands, allow for possible absorption of longer wavelengths.[43] These structures are often from of the same inorganic materials as the planar photovoltaics described earlier, but they also can be composed of organic materials.[19]

1.5.5 Organics

Organic solar cells currently operate with relatively low efficiency, but offer the potential for low-cost, non-toxic materials that can be used in innovative and integrative applications such as transparent photovoltaic windows.[44]

Organic solar cells operate slightly differently from the inorganic photovoltaic materials described previously. In inorganic semiconductors, energy bands are formed by the merging of energy levels of individual atoms.[21] In organic solar cells, orbitals split and form band-like structures.[44] A *p*-orbital is composed of two lobes of opposite phase.

In conjugated compounds, in which alternating single and double bonds result in electron delocalization, the atoms share *p*-orbitals to produce molecular orbitals. When multiple *p*-orbitals are arranged so that like phases overlap, the result is a bonding (π) molecular orbital. Conversely, when opposite phases overlap, the result is an antibonding (π*) molecular orbital. Usually, the highest energy π molecular orbital is the highest occupied molecular orbital (HOMO), and the lowest energy π* molecular orbital is the lowest unoccupied molecular orbital (LUMO).[45] When a sufficiently large number of these molecules come together, the splitting and overlap of the HOMO and LUMO of each molecule provide a valence and conduction band-like structure, respectively.[44] However, the electron and hole in the exciton generated when an electron is excited from the HOMO to LUMO are much more strongly attracted than they are in inorganic solar cells. Moreover, the binding energy is at least 10 times greater than thermal energy at room temperature.[46] Thus, the diffusion length is relatively short in organic solar cells, and they require nearly atomically abrupt heterojunctions between donor and acceptor materials.[44,46] It is unknown exactly how charges separate at these interfaces.[46] However, because of the short diffusion length, the active layers in organic solar cells are known as bulk heterojunctions, and consist of a mixture of organic donor and acceptor materials. Thus, interfaces between the two are never far from any given position where an exciton might be generated.[44]

To reach and exceed a current goal of 15% efficiency, it is necessary to reduce the binding energy of the excitons, which can be accomplished with materials of higher dielectric constant. Other areas of focus in organic solar-cell research include improving

charge transport to increase the fill factor, and achieving a better understanding of the physics of energy loss.[46]

1.5.6 Perovskites

There has been much excitement generated over the recent advances in perovskite technology. Since its beginnings in 2009 as an outgrowth of dye-sensitized solar cells,[47] perovskites have achieved conversion efficiencies of more than 22%.[38] Such a rapid rise in performance, as shown in figure 1.6a, is outpacing the growth of other photovoltaic technologies and is a source of optimism for future development.[38]

One problem in determining the efficiency of perovskite solar cells results from a hysteresis behavior: two different current-voltage curves result depending on whether the scan is performed from positive to negative voltage or from negative to positive voltage. Migration of ionic defects within the perovskite material has been identified as the likely cause of this hysteresis. However, current-voltage curves of perovskite devices have also been shown to depend on the scan rate of the performance test.[48] With no single reliable current-voltage curve, identifying a maximum power-point is problematic. Prior to 2014, this hysteresis was not taken into account in efficiency measurements, and thus efficiencies reported before 2014 are considered suspect.[48] Since then, such methods as slow scan rates and maximum power-point tracking enable more reliable measurements, so that the current record of 22.1%, as shown in figure 1.5b,[38] appears trustworthy and is comparable with current solar cells in the market.[48]

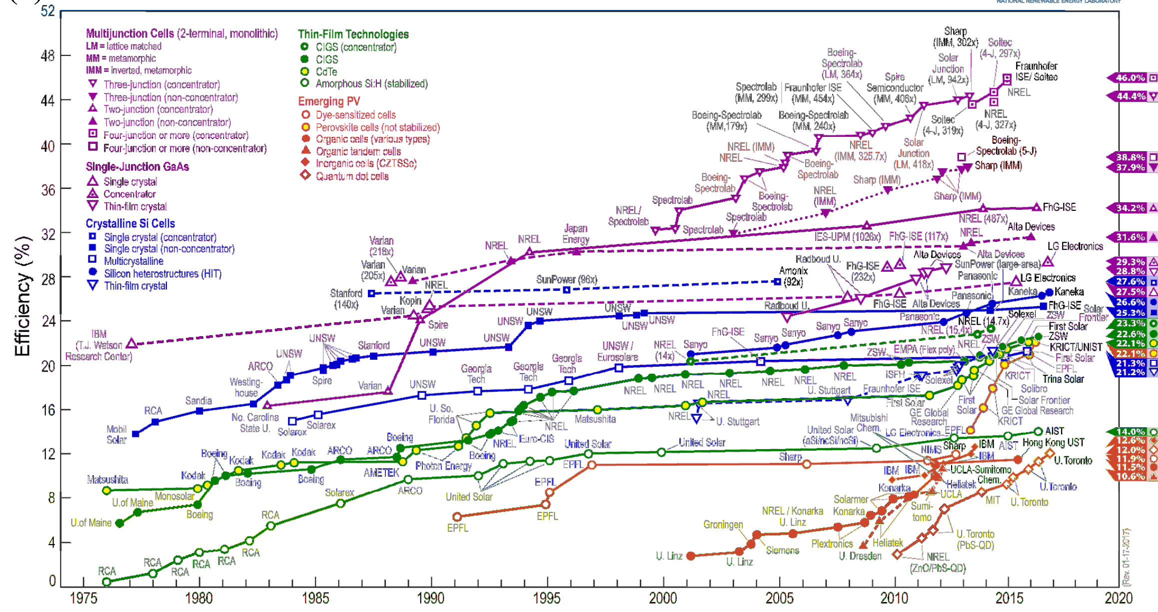

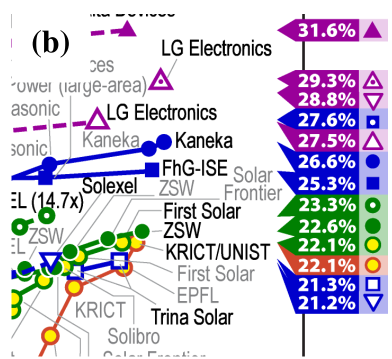

Figure 1.6: a) Record efficiencies of solar cell technologies. The orange circles filled with yellow represent perovskite solar cells. The slope of the progress of perovskites is clearly greater than the slope of other types of solar cells, prompting optimism in the material.[38] b) magnified region of a), showing the record efficiency of perovskite solar cells (22.1%) compared to Si-based solar cells shown in blue.[38]

The term perovskite refers to a common crystal structure. Perovskite solar cells consist of a (usually) organic cation in a cubo-octahedral site, a metal cation – often Pb – in an octahedral site, and three times as many halide or oxygen anions in the corners of the unit cell, as shown in figure 1.7a.[47,49] The ideal unit cell is cubic, but in reality is often

tetragonal, orthorhombic, or rhombohedral, and the perovskite will often undergo phase transitions at varying temperatures.[48] The morphology of the perovskite is important, affecting band gap,[48] and possibly even carrier diffusion length.[47] Additionally, because the perovskites are ionic compounds, they may dissolve in polar solvents like water. Thus, perovskite solar cells exhibit instability in humid environments unless they are encapsulated.[48] Ionic migration and segregation can also cause problems if ions reach the perovskite surface where they may form a space charge layer at the interface with neighboring device layers.[48]

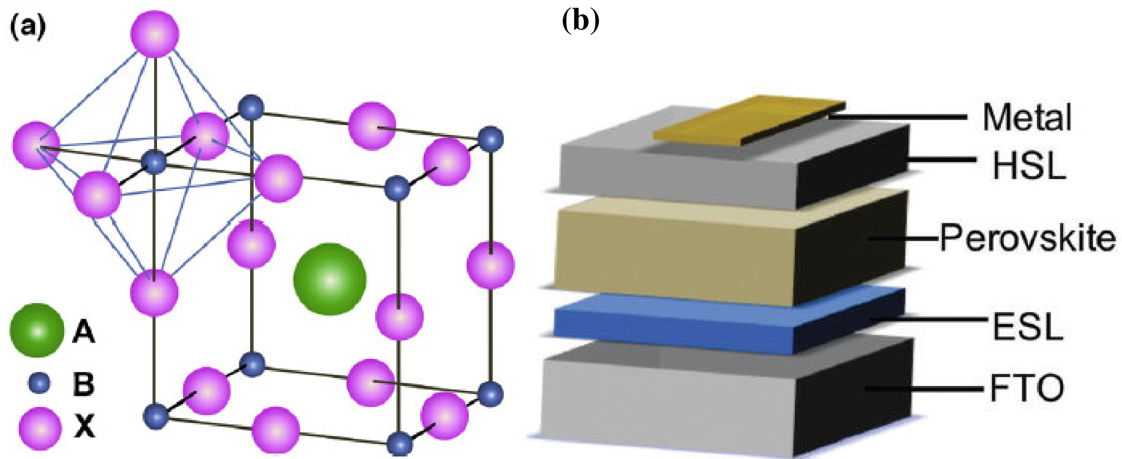

Figure 1.7: (a) Unit cell of perovskite crystal structure. A represents the organic cation, B represents the metal cation, and X represents the oxide or halide anion.[47] (b) Schematic of conventional perovskite solar cell structure.[48]

Perovskites were initially used as sensitizers in dye-sensitized cells, but once it was demonstrated that perovskites worked on their own, it became clear that the method of electron-hole pair generation differed not only from the inorganic solar cells previously discussed, but also from dye-sensitized cells.[47] Much of the physics of

perovskite solar cells is still the subject of investigation, but it is known that solar radiation causes the splitting of quasi-Fermi levels inside the material.[48] Perovskites are direct band-gap materials, and antibonding within the valance band results in “defect tolerance,” in which dangling bonds at the surface are not problematic. Grain boundaries have been found not to be significant sites of recombination, but rather impediments to charge transport, thus reducing the fill factor of the device but not the open-circuit voltage.[48]

The “traditional” structure of solar cells based on perovskites is shown in figure 1.7b. The electrons and holes separated in the perovskite are transported by the neighboring electron- and hole-selective layers (ESL and HSL), respectively. A metal contact provides outlet to an external load.[48]

One real-world problem is that Pb cations often used in perovskite solar cells are toxic to humans.[50] Sn has been studied as a replacement for Pb, but it easily oxidizes. A metal-organic cation with Sn as the metal has demonstrated improved stability, but determining the best replacement for Pb is still a widely investigated issue.[50]

Future challenges for perovskite-based solar cells include finding a suitable replacement for the toxic lead, and gaining a better understanding of the effect of chemical impurities and properties of device interfaces in order to improve the open-circuit voltage and fill factor.[48]

1.6 Overview of dissertation research

The research of this dissertation relates to the characterization of several combinations of materials that were being actively explored as the potential basis for solar cells with higher levels of efficiency. The materials were of particular interest to our

collaborators at Arizona State University and elsewhere who were members of the NSF/DOE Engineering Research Center entitled Quantum Energy and Sustainable Solar Technologies (QESST).

In chapter 2, the methods used to grow the samples characterized in this dissertation research are introduced. The characterization tools used by collaborators are summarized, followed by a discussion of transmission electron microscopy (TEM) specimen preparation and imaging.

In chapter 3, a study of the defects and anti-phase boundaries (APBs) in GaP/Si samples is presented. GaP has the potential to act as a virtual substrate for III-V growth on Si, due to the small lattice mismatch between the two materials. The defects of GaP/Si samples grown by molecular beam epitaxy (MBE) were correlated with GaP layer thickness, and direct imaging of anti-phase boundaries samples grown by MBE and migration-enhanced epitaxy (MEE) was used to understand the basis of APB formation.

In chapter 4, characterization of microcrystalline silicon (*μc*-Si) grown on *a*-Si is presented. Microcrystalline Si is a promising alternative to the front *a*-Si layer in silicon heterojunction solar cells, and transmission electron microscopy (TEM) was used here to monitor the growth of *μc*-Si with and without nanocrystals to seed the crystalline growth. TEM was also used to help identify a method to determine the percent crystallinity in the microcrystalline layer.

In chapter 5, a study of Al/Ge layer exchange and metal-induced crystallization is briefly described. Layer exchange and metal-induced crystallization comprise an inexpensive method to grow *c*-Ge, and the purpose of this work was to understand the mechanism of the crystallization and layer exchange.

In chapter 6, structural characterization of InAs quantum dots with GaAsSb spacer layers of varying thickness is presented. The structure is an intermediate band solar cell, with potential to collect photons with wavelengths larger than the band gap, and the effect of the structure on the performance is investigated.

In chapter 7, the surface structures of hydrogen-plasma-treated (HPT) Si samples are characterized and compared to sample lifetimes. HPTs can increase the passivation of *a*-Si layers on *c*-Si. However, they can also etch the *c*-Si surface. *a*-Si/*c*-Si specimens with and without oxide capping layers were treated for varying lengths of time, and HRTEM images were used to determine whether structural differences had caused differing minority carrier lifetimes.

In chapter 8, the outlook of each project and possible future work are discussed.

References

1. U.S. Energy Information Administration. 2017. Monthly Energy Review, December 2017. p 3.

2. U.S. Energy Information Administration. 2018. Monthly Energy Review, March 2018. p 3.

3. U.S. Energy Information Administration. 2016. International Energy Outlook 2016. pp 7-9.

4. Tiwari, G.N. and Mishra, R.K. 2011. *Advanced Renewable Energy Sources*. Cambridge: Royal Society of Chemistry.

5. Environmental Defense Fund. 2017. Now Hiring: The Growth of America's Clean Energy & Sustainability Jobs. p 4.

6. Executive Office of the President. 2013. The Presdient's Climate Action Plan. p 6.

7. Office of Chief Financial Officer. 2015. Department of Energy FY 2016 Congressional Budget Report. p 15.

8. Bosi, M. and Pelosi, C. 2007. *Progress in Photovoltaics: Research and Applications* **15**: 51.

9. Youth with a Mission Medical Ships. 2013. Using Solar Power to Bring Light and Life into the Delivery Room.

10. Youth with a Mission Medical Ships. 2013. Solar Powered Dental Chair.

11. World Food Programme. mobile Vulnerability Analysis Mapping (mVAM).

12. Brown, M. 2017. "Solar Lanterns Serve as Beacon of Hope for Puerto Rico," Sierra. Sierra Club.

13. Buller, S. and Strunk, J. 2016. *Journal of Energy Chemistry* **25**: 171.

14. Office of Chief Financial Officer. 2018. Department of Energy FY 2018 Congressional Budget Request. p 1.

15. Fu, R., et al. 2017. U.S. Solar Photovoltaic System Cost Benchmark: Q1 2017. National Renewable Energy Laboratory. p 49.

16. Nelson, J. 2003. *The Physics of Solar Cells*. London: Imperial College Press.

17. National Renewable Energy Laboratory. Reference Solar Spectral Irradiance: Air Mass 1.5.

18. Griffiths, D.J. 2017. *Introduction to Electrodynamics, 4th Edition*. Cambridge: Cambridge University Press.

19. Yu, M., Long, Y.-Z., and Sun, B. 2012. *Nanoscale* **4**: 2783.

20. Diodes, LEDs and Solar Cells. 2015. *Inorganic Chemistry LibreTexts*

21. Halliday, D., et al. 2008. *Fundamentals of Physics, 8th Edition*. [city]: John Wiley & Sons, Inc.

22. Honsberg, C. and Bowden, S. 2017. Absorption Coefficient. PVEducation.org

23. Feifel, M. 2017. *IEEE Journal of Photovoltaics* **7**: 502.

24. Würfel, P. and Würfel, U. 2016. *Physics of Solar Cells: From Basic Principles to Advanced Concepts*. Weinheim: Wiley-VCH Verlag GmbH & Co.

25. Shockley, W. and Read, W.T., Jr. 1952. *Physical Review* **87**: 835.

26. McCluskey, M.D. and Haller, E.E. 2012. *Dopants and Defects in Semiconductors*. Boca Raton: CRC Press.

27. Maros, A., Faleev, N., King, R.R., Honsberg, C., Convey, D., Xie, H., and Ponce, F.A. 2016. *Journal of Vacuum Science and Technology* **34**: 02L113.

28. Fahrenbruch, A.L. and Bube, R.H. 1983. *Fundamentals of Solar Cells*. New York: Academic Press.

29. Pagliaro, M., Palmisano, G., and Ciriminna, R. 2008. *Flexible Solar Cells*. Palermo: Wiley-VGH, Weinheim.

30. Siebentritt, S. 2017. In Eds. Reinders, A., Verlinden, P., van Sark, W., and Freundlich, A. *Photovoltaic Solar Energy: From Fundamentals to Applications*. West Sussex: Wiley.

31. Shockley, W. and Queisser, H.J. 1961. *Journal of Applied Physics* **32**: 510.

32. Luque, A. and Martí, A. 1997. *Physical Review Letters* **78**, 5014.

33. Chen, M. and Blankenship, R.E. 2011. *Trends in Plant Science* **16**: 427.

34. Ibach, H. and Lueth, H. *Solid-State Physics*. Springer Verlag, 2003

35. Ramanujam, J., 2016. *Progress in Materials Science* **82**: 294.

36. Bye, G. and Ceccaroli, B. 2014. *Solar Energy Materials & Solar Cells* **130**: 634.

37. Płaczek-Popko, E. 2017. *Opto-Electronics Review* **25**: 55.

38. National Renewable Energy Laboratory. 2017. Best Research-Cell Efficiencies.

39. Kroemer, H. 1987. *Journal of Crystal Growth* **81**: 193.

40. Friedman, D.J. 2010. *Current Opinion in Solid State and Materials Science* **14**: 131.

41. Luque, A. 2011. *Journal of Applied Physics* **110**: 031301.

42. Garcia, I., France, R.M., Geisz, J.F., McMahon, W.E., Steiner, M.A., Johnston, S., and Friedman, D.J. 2016. *IEEE Journal of Photovoltaics* **6**: 366.

43. Luque, A., Marti, A., and Stanley, C. 2012. *Nature Photonics* **6**, 146.

44. Stephen, M., Genevicius, K., Juska, G., Arlauskas, K., and Hiorns, R.C. 2017. *Polymer International* **66**: 13.

45. Bruice, P.Y. 2004. *Organic Chemistry, 4th Edition*. Upper Saddle River: Prentice Hall.

46. Zhang, J., Zhu, L., and Wei, Z. 2017. *Small Methods* **1**: 1700258.

47. Park, N.-G. 2015. *Materials Today* **18**: 65.

48. Correa-Baena, J.P., Abate, A., Saliba, M., Tress, W., Jacobsson, T.J., and Grätzel, M., Hagfeldt, A. 2017. *Energy & Environmental Science* **10**: 710.

49. Song, Z., Watthage, S.C., Phillips, A.B., and Heben, M.J. 2016. *Journal of Photonics for Energy* **6**: 022001.

50. Abate, A. 2017. *Joule* **1**: 659.

CHAPTER 2

EXPERIMENTAL METHODS

This chapter briefly describes the growth methods that were used by our colleagues to produce the samples studied during the research of this dissertation, which included plasma-enhanced chemical vapor deposition (PECVD), molecular beam epitaxy (MBE), and migration enhanced epitaxy (MEE). Characterization methods utilized by our colleagues, including ellipsometry, Raman spectroscopy, x-ray diffraction (XRD), and photoluminescence (PL), are also outlined. Sample preparation methods for transmission electron microscopy (TEM), including focused-ion-beam (FIB) milling and polishing/dimpling/argon-ion milling, are then detailed. Finally, TEM, scanning transmission electron microscopy (STEM) including high-angle annular dark-field STEM (HAADF), aberration-corrected (AC) electron microscopy, and energy dispersive x-ray spectroscopy (EDX/EDS) are described in detail.

2.1 Growth methods

This section summarizes the fundamental principles of the growth methods which were used to produce samples studied in this research.

2.1.1 Plasma-enhanced chemical vapor deposition

Chemical vapor deposition (CVD) is a growth method in which gaseous reactants undergo chemical reaction on or near a heated substrate, followed by the removal of the byproducts.[1] For example, silane (SiH_4) is a commonly used reactant which undergoes thermal decomposition when it reaches a heated substrate, forming solid Si and H_2 gas.

The Si forms a coating on the substrate surface, and H_2 is removed. A gaseous boundary layer forms above the substrate due to fluid dynamics, and reactions may take place above, within, or below this boundary layer. The system itself consists of a reactant-gas dispensing system, reactor, and exhaust system. Commonly employed CVD processes include metal-organic chemical vapor deposition, vapor-phase epitaxy, atomic layer deposition, and plasma-enhanced chemical vapor deposition (PECVD).[1]

In PECVD, a weakly ionized plasma is introduced into the CVD reactor.[2] The electrons of the plasma collide with gaseous reactants, providing the activation energy necessary for chemical reactions to proceed. In addition, radiation from plasma discharge can change the surface chemistry of the substrate and subsequently grown films.[2] The *μc*-Si/*a*-Si/*c*-Si samples described later were grown using PECVD by Joe Carpenter in the group of Professor Zachary Holman at Arizona State University.

2.1.2 Molecular beam epitaxy

Molecular beam epitaxy (MBE) is a growth technique in which "beams" of gaseous atoms or particles are deposited on a heated substrate in an ultra-high vacuum (UHV) chamber.[3] The substrate is heated in order to facilitate migration of the vapor-phase atoms across the substrate surface before they finally adsorb, and it is continuously rotated in order to achieve uniform surface coverage. The gas sources may originate from evaporation or sublimation from ribbons, wires, or crucibles (which may or may not be connected to a needle valve to improve flow consistency). Gas flow into the growth chamber is "switched" on and off by means of a shutter.[3] The purpose of the UHV is primarily to promote growth that is effectively free from any unintentional doping. The

UHV also increases the mean free path of gas molecules, thereby eliminating the boundary layer of other gas-phase growth techniques such as CVD.[3] This boundary layer covers the solid surface during growth and can act as a receptacle for gas atoms or molecules intended for deposition, leading to a broadening of the interface. Without the boundary layer, gases in the MBE chamber can be quickly turned on and off to produce more abrupt interfaces.[3] Two separate growth chambers are often used, one for the II/IV materials and another for the III/V materials, in order to avoid accidental doping from cross-contamination.[3]

The GaP/Si samples studied here were grown using MBE by Dr. Chaomin Zhang and Dr. Nikolai Faleev at Arizona State University.

2.1.3 Migration enhanced epitaxy

The advantage of MBE of switching gases on and off quickly can also be applied to different species of gases, and this approach is the basis of migration enhanced epitaxy (MEE).[3] In traditional MBE growth of III/V materials, both the III- and V-species are introduced into the chamber simultaneously. In MEE, the shutters for the different species are alternately open and closed, so that only one gas is being deposited onto the substrate at any time.[3]

In MBE, the finite migration of adatoms leads to the growth of small islands which eventually coalesce.[4] This growth method naturally results in a surface roughness of several monolayers. In contrast, the alternating deposition of species in MEE leads to coverage of the entire surface by one species before deposition of the next. Thus the surface roughness should ideally be one monolayer or less.[4] Another advantage of

depositing one monolayer at a time is the possibility of using lower growth temperatures, which serves to decrease interdiffusion between layers and possibly result in more abrupt interfaces.[3]

Additional GaP/Si samples were grown using MEE by Dr. Chaomin Zhang and Dr. Nikolai Faleev at Arizona State University.

2.1.4 Stranski-Krastanov growth

The Stranski-Krastanov (SK) growth mode describes a process whereby quantum dots (QDs) may be formed. In SK growth, heteroepitaxial deposition initially proceeds monolayer-by-monolayer. At a critical thickness depending on the lattice mismatch between materials, the growth mode changes from two dimensional to three-dimensional. Continued growth beyond the critical thickness results in the formation of QDs.[5] InAs QDs with GaAsSb spacer layers to produce SK growth were grown using MBE by Yeongho Kim and Keun-Yong Ban in the group of Professor Christiana Honsberg at Arizona State University.

2.2 Sample characterization methods

2.2.1 Ellipsometry

When linearly polarized incident light is reflected from a material surface, the s-polarized component is perpendicular to the plane of incidence, and the p-polarized component is parallel to the plane.[6] Once the beam is reflected, the amplitudes and phases of each component may change, and consequently, the reflected beam may be elliptically polarized.[6,7]

A schematic of an ellipsometer is shown in figure 2.1.[7] A polarization state generator (PSG) linearly polarizes the incident beam. Generally, a rotating compensator is placed after the PSG so that multiple directions of incident polarization can be measured as a function of time. The specularly reflected beam passes through a polarization state analyzer (PSA), often a linear polarizer in a fixed position.[7] The detected light wave can yield the ratio of reflection coefficients of p-polarized to s-polarized light.[6] From these values, further calculations can determine the specimen layer thickness(es), index of refraction, dielectric permittivity, and other parameters.[6]

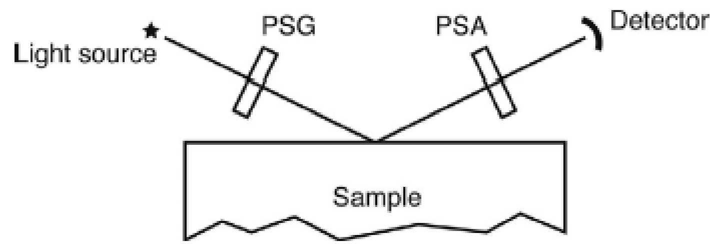

Figure 2.1: Schematic diagram of ellipsometry.[7] An incident beam passes through a polarization generator and reflects from the sample surface. The specularly reflected beam passes through a polarization state analyzer before hitting the detector.

In this work, ellipsometry was used to determine thickness of *μc*-Si layers, and the technique was compared to UV Raman spectroscopy for determining the percent crystallinity of those layers.

2.2.2 Raman spectroscopy

Raman scattering is the inelastic scattering of electromagnetic radiation from particles smaller than the wavelength of incident light.[8] Radiation scattered to longer

wavelengths (lower frequencies) is known as Stokes, and conversely, shorter wavelengths (higher frequencies) comprise anti-Stokes lines.[8] Energy is transferred to (Stokes) or from (anti-Stokes) the specimen as the electric field component of the incident radiation interacts with chemically bonded electrons, causing electronic vibrations within the specimen.[8,9] The energy shift associated with a particular vibration in a semiconductor is dependent on the specific material, its crystal and electronic structure, and its phonon properties.[9,10]

Raman spectroscopy involves irradiating a specimen with laser light and then reflecting the scattered radiation onto a grating to separate constituent wavelengths.[8] Since elastic Rayleigh scattering dominates, and Raman scattering constitutes only a small percentage of scattered light, a photomultiplier is used before recording the spectrum. The energy peaks are analyzed to provide information about the composition and structure of the specimen, such as strain, band structure, and composition.[8-10]

In this work, UV Raman spectroscopy was compared to ellipsometry in determining the percent crystallinity of μc-Si layers.

2.2.3 X-ray diffraction

When radiation in the x-ray region of the electromagnetic spectrum diffracts from a crystal lattice, the resulting constructive interference is described by Bragg's Law:

$$2d\sin\theta = n\lambda \tag{2.1}$$

where the path length difference, $2d\sin\theta$, is determined by the azimuthal distance d between atomic planes and the angle θ that the incident ray makes with specific lattice

planes of the crystal. As for other instances of interference, n is an integer, and λ is the wavelength of the radiation.[11]

XRD utilizes a monochromatic x-ray beam incident onto a crystal specimen.[11] The intensity of the diffracted beam is recorded as a function of angle of incidence. This spectrum can then be compared to standard spectra to determine composition, crystal lattice, orientation, and crystal quality.[11]

In this work, various samples of GaP/Si, Al/Ge, and InAs quantum dots were characterized using XRD.

2.2.4 Photoluminescence

When electrons in a semiconductor are excited from the valence band to conduction band, electron-hole pairs are formed.[12] This pair can recombine to emit photons. In device performance considerations, such radiative recombination is undesirable since it decreases the device efficiency. Conversely, this emission, or luminescence, can be used to characterize the semiconductor. There are several different types of luminescence, depending on the source of energy for formation of the electron-hole pair. In photoluminescence, this energy source is an incident photon.[12]

A laser beam that is incident on the sample produces photoluminescence, which is then dispersed by a spectrometer, and strikes a photomultiplier tube detector.[12] The collected photons can be used to determine specimen composition, layer thicknesses, information about impurities, and efficiency.[12]

In this work, InAs quantum dots with GaAsSb spacer layers were characterized by photoluminescence.

2.3 TEM sample preparation

The specimen thickness for TEM imaging is on the order of or less than the electron mean-free path, which depends on accelerating voltage.[13] Thicknesses of less than 10nm are generally considered preferable for high-resolution studies, though thicker specimens of up to ~100nm can be appropriate for other TEM analysis.[14] In the research described in this dissertation, two methods of sample preparation were used: i) focused-ion beam; and ii) conventional polishing, dimpling, and argon ion milling. This section briefly describes both methods.

2.3.1 Focused-ion beam

Focused Ion Beam (FIB) milling is a TEM sample preparation technique where an ion beam in a vacuum chamber is focused onto a selected area of the specimen and used to mill the sample away to a specified depth, in the end leaving behind a specimen of suitable TEM-imaging thickness.[15] As illustrated in figure 2.2a,[16] the FIB instrument is often combined with a scanning electron microscope (SEM), to enable simultaneous milling and viewing. Thus, the FIB is especially useful to produce site-specific specimens.[15] The FIB technique is also advantageous over conventional mechanical polishing and dimpling for samples that break or undergo damage during the latter process, or samples that react with water or other chemicals used in polishing/dimpling.[17]

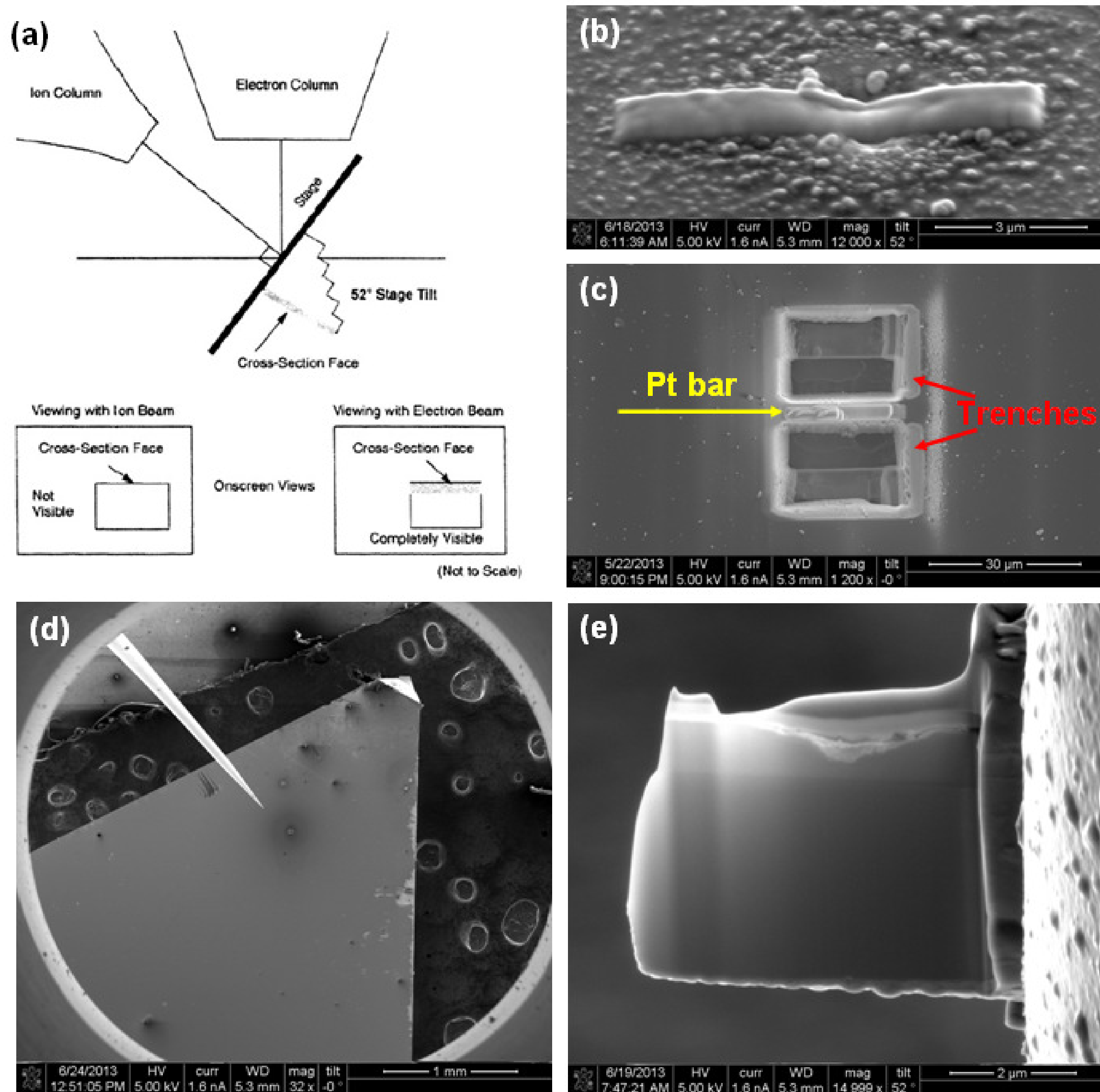

Figure 2.2: a) Schematic showing the geometry of electron and ion beams in a dual-beam FIB-SEM. A sample on a stage at eucentric height can be tilted 52° for ion-beam viewing if required.[7] b) Protective platinum bar deposited on the sample surface. c) Sample after material on either side of the platinum bar has been trenched away. d) Liftout needle approaching the sample for *in-situ* liftout. e) Specimen mounted on a TEM grid and thinned to electron transparency.

Typical FIB preparation begins with deposition of protective carbon and platinum "bars" covering the area where the specimen area of interest is located,[18] as shown in figure 2.2b. The carbon layer can be deposited either *ex situ* or *in situ*, although the platinum layer is preferably deposited *in situ*. The material on either side of the long edges of the bar is then milled or "trenched" away with the focused ion beam, as shown in figure 2.2c. Next, the stage is tilted to mill under the desired area, and on either side of the short edges of the bar, often leaving only a small area of connection between the specimen and the bulk material next to one of the short edges of the bar.[18]

The subsequent liftout process can be performed *in situ* (as shown in figure 2.2d) or *ex situ*, and involves attaching a needle to the specimen, either through platinum deposition (*in situ*) or electrostatic attraction (*ex situ*).[18] The needle is then used to transport the sample to a TEM grid, and to attach it using the same method as originally used to attach the needle. If welding is involved, the needle is cut free from the specimen with the ion beam. If the specimen is not already electron transparent, it can be thinned on the grid, as shown in figure 2.2e.[18]

The FIB specimens in the work described in this dissertation were prepared with an FEI NOVA200 dual-beam FIB-SEM, using gallium ions. The general procedure was to deposit a "generous" layer of C *ex situ* using an Electron Microscopy Sciences EMS950 carbon coater; deposit a 200-300nm-thick, 15-µm x 1.2µm Pt bar using a 5keV, 1.6nA electron beam in the NOVA; continue the Pt bar 2-3µm, but reducing the width to 1µm, using a 30keV, 0.1nA Ga ion beam; mill a rectangle of 20µm x 6µm on either side of the bar, each approximately 3µm away from the bar, using a 30-keV, 7-nA Ga ion beam; using the "cleaning cross-section" setting on the NOVA, step down in current to

3nA and then 1nA, gradually coming closer to the bar until the bar is reached; perform undercuts at a -62º angle relative to the ion beam, using a 30-keV, 1-nA gallium ion beam; lift out the sample *in situ* using a 0.1nA ion beam to deposit the Pt that welds the needle to the specimen and to cut the specimen away from the bulk; weld the specimen to the TEM grid with ion-beam Pt, at 0.1nA; thin the specimen to desired thickness using the "cleaning cross-section" setting, first with a 0.3nA ion beam on both sides of the specimen, then 0.1nA; perform final cleaning to remove redeposited material using a 5-keV, 79-nA ion beam. Small adjustments to this procedure were sometimes made to address difficulties on the day, since sample preparation often proves to be more of an art than a science.

2.3.2 Polishing/ dimpling/ argon ion milling

The hand-prepared specimen in this work was polished on both sides using diamond lapping films of successively finer grade until the specimen thickness was approximately 100µm. The specimen was then dimpled with a copper wheel followed by a cloth wheel so that the thickness after dimpling was approximately 10µm. The specimen was then transferred to a copper TEM grid and argon-ion-milled at 2keV-3keV until a small hole was visible, so that the area around the hole was sufficiently thin for TEM imaging.

2.4 Transmission electron microscopy

Transmission electron microscopy accelerates high-energy electrons through a vacuum column, and focuses the beam onto the sample with electromagnetic lenses.[14]

These electrons interact with a thin specimen. Those which are transmitted through the specimen form an image which is magnified with additional electromagnetic lenses, and the electrons finally strike a phosphorescent screen or a detector which converts the signal to a digital image or an image on film. Other results of the interactions of electrons and matter can be detected and measured to provide additional information about the specimen.[14]

2.4.1 Fundamentals of TEM

The electron source is commonly known as the electron gun, and it is positioned near the top of the column. Some (often older) electron guns operate using thermionic emission from a filament source such as W or LaB_6. A field emission gun (FEG) uses an electric field as well as thermionic emission, and a cold FEG relies solely on an electric field to free the electrons.[14] Electron beams from FEGs, cold or otherwise, are considered as coherent,[19] although monochromators are sometimes used to further reduce the range of electron wavelengths for aberration-corrected studies (see section 2.4.3).[19] Electrons are accelerated from the filament to the anode at typical energies of 100keV or more, and this energy is the primary determinant of the electron wavelength.[19] Structural resolution depends in large part on the wavelength, as understood from the equation

$$d=AC_s^{1/4}\lambda^{3/4} \tag{2.2}$$

where d is the structural resolution, A is a constant, C_s is the spherical aberration coefficient of the objective lens, and λ is the electron wavelength.[20]

Electrons from the gun proceed at relativistic speeds through magnetic lenses designed to focus the electrons.[13,19] These lenses incorporate currents in annular coils,

which induce magnetic fields between iron pole-pieces. The magnetic force exerted on free electrons in the column causes these electrons to proceed down the column in a spiral trajectory.[13]

When electrons reach the specimen, they interact as both a particle and a wave. As a particle, electrons collide with atoms in the specimen, and geometric optics can be used to approximate electron paths as rays.[19] Diffraction contrast imaging reveals differences in amplitude after electrons pass through different regions of the specimen.[14] As a wave, the phase of the electron is changed as a result of its interaction with the specimen. High-resolution, or phase-contrast, imaging thus relies on having a coherent electron source,[19] especially in aberration-corrected imaging.[21]

After passing through the specimen (or slightly before, in the case of lenses with some pre-field), the electrons pass through the magnetic field of the objective lens.[19] The diffraction pattern of the specimen appears at the back focal plane of the objective lens, and an objective aperture is placed at this plane to select particular diffraction spots. Additional lenses after the objective lens serve to magnify the image that is eventually formed on a phosphorescent screen at the end of the lens column. Photographic film or preferably a CCD camera can be used to record the image for later analysis.[19] A simplified schematic of the electron-optical elements of TEM are shown in figure 2.2.[13]

In this work, an FEI-Phillips CM200 FEG TEM operated at 200kV was used to characterize specimens of GaP/Si, *μc*-Si/*a*-Si/*c*-Si, *a*-Si/*c*-Si, Al/Ge, and InAs quantum dots with GaAsSb spacer layers.

2.4.2 Scanning transmission electron microscopy

The geometrical optics of a scanning transmission electron microscope (STEM) can be considered as the reciprocal of a conventional TEM, as shown in figure 2.3.[13] The electron source is demagnified by the condensor and objective lenses so that it consists of a fine probe when it reaches the specimen. This probe is scanned across the specimen surface.[13] Transmitted electrons that have been scattered to different angles can provide different types of information.[14] In bright-field (BF) STEM imaging, the direct beam is detected as well as electrons scattered to angles defined by outer aperture. The phase-contrast image is formed by interference between the direct beam and diffracted beams.[22] Dark-field STEM is the result of electrons detected between an inner and outer aperture, thus excluding the direct beam.[14] These two types of images can be collected simultaneously.

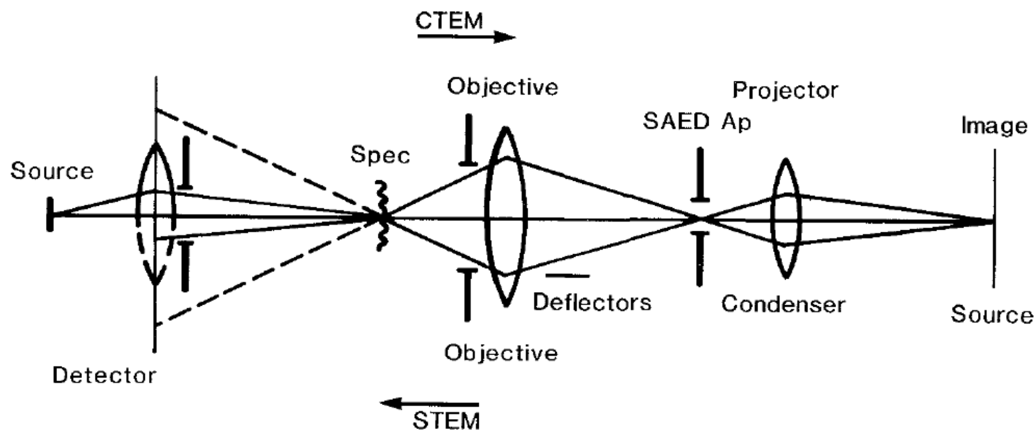

Figure 2.3: Schematic showing the simplified optics of TEM and STEM systems.[13] In conventional TEM (CTEM), electrons proceed from left to right, from the source to the specimen, then through objective and magnifying lenses to form the final image. In

STEM, the electrons proceed from right to left, with the source demagnified by the condensor and objective lenses to form the small probe on the specimen surface.

In high-angle annular-dark-field imaging, incoherent electrons that experience Rutherford scattering are collected. Thus, diffraction contrast due to coherent electron beams is minimized for thin specimens.[21] Instead, detection of this thermal diffuse scattering results in contrast proportional to Z^x, where Z is the atomic number of each respective imaged atom, and $1.5 \leq x \leq 2$, depending primarily on the inner and outer detector angles.[23]

2.4.3 Aberration-corrected (S)TEM

The two primary methods used to achieve atomic-resolution imaging are high-voltage microscopy (HVEM) and aberration correction.[24] The higher accelerating voltages of the HVEM correspond to shorter electron wavelength, and thus better resolution is achieved when compared with medium-voltage instruments.[20] However, the likelihood of specimen damage is greatly increased, and greater costs become an important consideration.[24]

Aberration correction does not have the drawbacks of high-voltage microscopy.[24] Aberration correction improves resolution by reducing or eliminating lens aberrations through online (hardware) or offline (software) methods,[24] so that spherical aberration in particular is no longer resolution-limiting.[20] Spherical aberration is a direct result of the rotational symmetry of the objective lens. Thus, a rotationally asymmetric field, in conjunction with automatic digital analysis of a tableau of diffractograms from an

amorphous region of the specimen (a process known as "autotuning"), can be used to reduce spherical aberration and achieve structural resolutions of less than 1.0Å.[20,24]

In this research, a probe-corrected JEOL ARM-200F was used to collect HAADF STEM images of GaP/Si specimens.

2.4.4 Energy-dispersive x-ray spectroscopy

When high-energy electrons collide with an atom, core-shell electrons may be ejected. In order to return to the ground state, an electron from a higher energy level de-excites to fill the hole, emitting an x-ray in the process. The energy of this x-ray is equal to the difference between energy levels and thus is characteristic of the element from which the photon is emitted.[11] A detector inside the microscope is used to collect x-rays and these will identify elements present in the specimen and also quantify the elemental composition based on the energy distribution of the x-rays detected.[14]

In part of this work, a KEVEX EDS detector installed on an FEI-Phillips CM200 FEG STEM operated at 200kV was used to study possible layer exchange in Al/Ge heterostructure specimens.

References

1. Carlsson, J.-O., Martin, P.M. 2009. “Chemical vapor deposition,” in Ed. Martin, P.M. *Handbook of Deposition Technologies for Films and Coatings: Science, Applications and Technology*. Elsevier.

2. Hess, D.W. 1986. *Annual Review of Materials Research* **16**: 163.

3. Franchi, S. 2013. “Molecular beam epitaxy: fundamentals, historical background and future prospects,” in Ed. Henini, M. *Molecular Beam Epitaxy*. Elsevier.

4. “Flow Rate Modulated Vapor Epitaxy.” 2001. In *Encyclopedia of Materials: Science and Technology*. Elsevier.

5. Ayers, J. E. 2007. *Heteroepitaxy of Semiconductors: Theory, Growth, and Characterization*. Boca Raton: CRC Press.

6. Toudert, J. 2014. *Nanotechnology Reviews* **3**: 223.

7. Podraza, N.J. and Jellison, G.E., Jr. 2017. In Eds. Lindon, J.C., Tranter, G.E., and Koppenaal, D.W. *Encyclopedia of Spectrsocopy and Spectrometry, 3rd Ed.* Oxford: Elsevier Ltd.

8. John, N., and George, S. 2017. “Raman Spectroscopy,” in Eds. Thomas, S., Thomas, R., Zachariah, A.K., and Mishra, R.K. *Spectroscopic Methods for Nanomaterials Characterization*. Cambridge: Elsevier.

9. Zhang, X., Tan, Q.-H., Wu, J.-B., Shi, W., and Tan, P.-H. 2016. *Nanoscale* **8**: 6435.

10. Wu, J.-B., Lin, M.-L., Cong, X., Liu, H.-N., and Tan, P.-H. 2018. *Royal Society of Chemistry* **47**: 1822.

11. Leng, Y. 2013. *Materials Characterization: Introduction to Microscopic and Spectroscopic Methods, 2nd Ed.* Weinheim: Wiley-VCH.

12. Gilliland, G.D. 1997. *Materials Science and Engineering* **R18**: 99.

13. Cowley, J.M. 1988. “Imaging,” in Ed. Cowley, J.M. *High-Resolution Transmission Electron Microscopy and Associated Techniques.* New York: Oxford University Press.

14. Williams, D.B., and Carter, C.B. 2009. *Transmission Electron Microscopy*. New York: Springer.

15. Phaneuf, M.W. 2005. “FIB for materials science applications – a review,” in Eds. Giannuzzi, L.A. and Stevie, F.A. *Introduction to Focused Ion Beams: Instrumentation, Theory, and Practice*. Boston: Springer.

16. Holdford, B. 2005. “Uses of dualbeam FIB in microelectronic failure analysis,” in Eds. Giannuzzi, L.A. and Stevie, F.A. *Introduction to Focused Ion Beams: Instrumentation, Theory, and Practice*. Boston: Springer.

17. Anderson, R. and Klepeis, S.J. 2005. “Practical aspects of FIB TEM specimen preparation,” in Eds. Giannuzzi, L.A. and Stevie, F.A. *Introduction to Focused Ion Beams: Instrumentation, Theory, and Practice*. Boston: Springer.

18. Gianuzzi, L.A., Kempshall, B.W., Schwartz, S.M., Lomness, J.K., Prenitzer, B.I., and Stevie, F.A. 2005. “FIB lift-out specimen preparation techniques: ex-situ and in-situ methods,” in Eds. Giannuzzi, L.A. and Stevie, F.A. *Introduction to Focused Ion Beams: Instrumentation, Theory, and Practice*. Boston: Springer.

19. Spence, J.C.H. 2013. *High Resolution Electron Microscopy. 3rd Ed*. Oxford: Oxford University Press.

20. Smith, D.J. 2008. *Microscopy & Microanalysis* **14**: 2.

21. Pennycook, S.J. 2012. *Ultramicroscopy* **123**: 28.

22. Nellist, P.D. 2011. In Eds. Pennycook, S.J. and Nellist, P.D. *Scanning Transmission Electron Microscopy: Imaging and Analysis*. New York: Springer.

23. Kim, S., Jung, Y., Kim, J.J., Lee, S., and Lee, H. 2015. *Journal of Alloys and Compounds* **518**: 545.

24. Smith, D.J., Aoki, T., Mardingly, J., Zhou, L., and McCartney, M.R. 2013. *Microscopy* **62**(Supplement 1): S65.

CHAPTER 3

DEFECT AND INTERFACE CHARACTERIZATION IN GaP/Si HETEROSTRUCTURES

This chapter describes the characterization of GaP/Si heterostructures that are of potential interest as the basis for multijunction solar-cell devices. The work was carried out in collaboration with Dr. Chaomin Zhang and Dr. Nikolai Faleev at Arizona State University, who were responsible for the sample growth and x-ray diffraction measurements. Results from this collaborative work have been published.[1]

3.1 Introduction and background

The 0.36% lattice mismatch between GaP and Si means that GaP/Si represents a promising candidate for photovoltaic devices, as well serving as a virtual substrate for subsequent epitaxial growth of other III/V materials.[2-4] Due to the finite lattice mismatch, there will inevitably be a certain critical thickness at which epitaxial growth of the GaP layer will no longer be pseudomorphic, and strain relaxation will result in defect formation.[5] Some growth defects in metamorphic III-P/Si systems have been shown to originate at the top surface, forming 60º misfit dislocations and threading defects as they glide down {111} planes to the III-P/Si interface.[6] These various defects can act as recombination centers,[6] which will adversely impact device applications, and thus it is important to determine how these defects are formed in order to minimize their formation.

A previous study of epitaxial GaInAs/GaAs and GaAsSb/GaAs heterostructures suggested that the onset of dislocation formation was actually at a different – and smaller – thickness than the onset of strain relaxation.[5] Moreover, three stages of defect

formation were observed: 1) the epitaxial layers were fully strained but no growth defects had formed; 2) the layers were fully strained but 60º misfit dislocations had formed; and 3) the layers experienced strain relaxation and a much higher density of defects had formed.[5] The proposed explanation was that not only did the 60º misfit dislocations relieve strain, but they also introduced some strain along the line of the dislocation, and strain relaxation only occurred when the relieved strain exceeded the created strain by critical amounts.[5,7] This explanation was originally postulated for the Si-Ge material system,[7] so that its application to GaInAs/GaAs and GaInSb/GaAs suggested possible wider applicability. However, the exact onset of these different stages depends on a variety of growth parameters, especially substrate temperature,[5,7,6] and it appeared that there was still much more to be learned. One of the goals of this current study of GaP/Si heterostructures is to advance fundamental knowledge of defect formation, in particular by studying the types of defects visible at different GaP layer thicknesses (different amounts of strain).

In addition to threading dislocations, defects that occur during epitaxial growth of polar-on-nonpolar materials include antiphase boundaries (APBs).[6] The polarity of GaP grown on Si substrates when grown by MOCVD[8] and MOVPE[9] has been shown to depend on the detailed structure of the Si surface. When the Si surface is flat, or its unevenness is manifest only in double steps (or *2n* steps), an entire GaP pair of atomic columns can fit adjacent to the step, and the GaP layer will be single domain,[10] as illustrated in figure 3.1.[6] Conversely, single steps (or *2n+1* steps) on the Si surface will result in GaP dumbbells that are out of phase because they will have in effect switched sublattices. Thus APBs will appear where regions of opposite phase meet.[6,9,10] When

these APBs propagate through the entire layer, they are likely to contribute to recombination and consequently lower open-circuit voltage (V_{OC}).[9, 11] In particular, the presence of an APB along a {110} direction will raise the valence band maximum, and consequently reduce the band gap energy.[12]

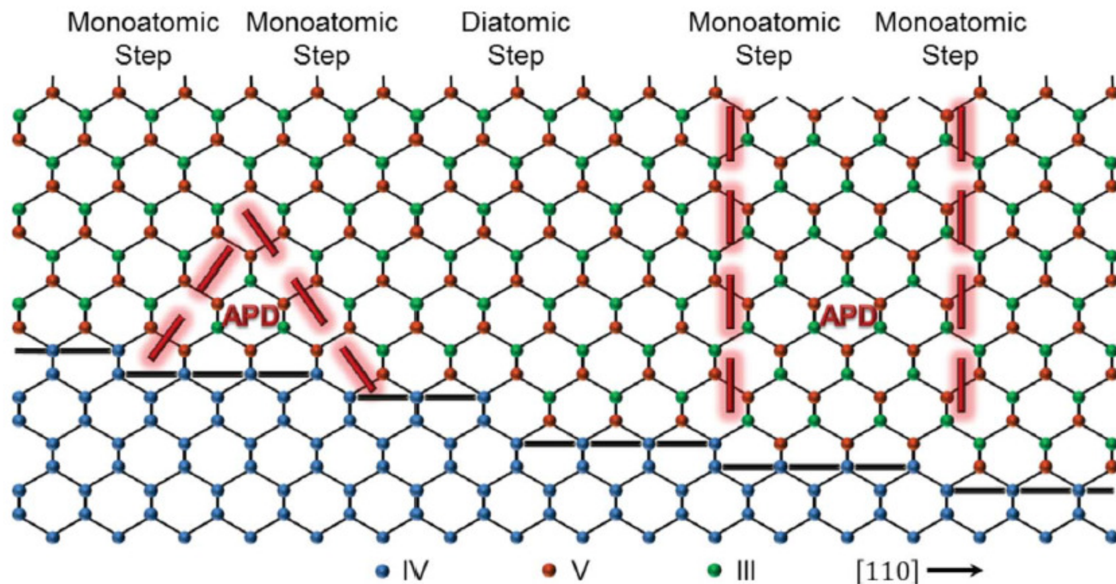

Figure 3.1: Schematic of a polar III/V material, such as GaP, on a diamond-cubic IV substrate, such as Si. Single, or monoatomic, steps result in polarity reversal, which leads to anti-phase domains (APDs) separated by APBs. The Si diatomic step would preserve the polarity of the GaP grown above.[6] The left side of the figure shows APBs formed along [111] planes that annihilate when they intersect.[6,14,15]

It has been shown that using a 4-6º miscut of the Si surface in a {110} direction, combined with high temperature annealing, will reduce the density of APBs, since the miscut causes Si atoms in single steps on the surface to rearrange into energetically favorable double steps.[6,10] A lesser miscut, even as small as 0.1º, in a direction other than

{110}, resulted in a primarily single-stepped Si surface,[13,14] causing a higher concentration of APBs that propagated to the GaP surface.[13] A Si(211) substrate has been shown to prevent APB formation altogether in GaAs growth.[10] This result occurs because the Si(211) surface consists of Si atoms with nonidentical bonding arrangements, which are consequently nonequivalent bonding sites for the III and V atoms.[10] Si(001) substrates are much more common, so that most studies have focused on GaP growth directly on Si(001).

Changes in growth conditions have been shown to reduce the formation of APBs. An MOVPE study showed that pre-treatment of the Si substrate, consisting of exposure to SiH_4 for 45 minutes followed by another 45 minutes of H_2, produced a smaller number of APBs than a pretreatment with only 30 minutes of SiH_4.[11] Moreover, these APBs were more likely after the former treatment to terminate within the GaP layer, instead of extending to the surface.[11] An increase in the H_2 pressure during annealing of a homoepitaxial Si buffer was found to increase the ratio of double steps to single steps on the Si surface, whereas an N_2 atmosphere favored formation of single steps.[16]

APBs can propagate vertically upwards along {110} planes, as shown on the right side of figure 3.1, thereby reproducing the shape of the Si surface.[6,13] Alternate APBs can be formed on {111} planes as shown on the left of the figure.[6] A benefit of these {111} APBs is that they annihilate when they intersect, as indicated in figure 3.1.[6,14,15] However, formation of {110} APBs is more energetically favorable.[17] As shown in figure 5.1, Ga-Ga bonds alternate between P-P bonds in APBs along {110} planes, whereas APBs along {111} planes exhibit only Ga-Ga or P-P bonds.[6,17] Therefore, the excess negative charge created by the P-P bond in {110} APBs is balanced by the nearby excess positive charge

created by the Ga-Ga bond. Conversely, there is only one type of excess charge in a {111} APB, which will be unbalanced unless another nearby {111} APB has the other type of bond.[17] APBs have also been shown to kink from {110} to {111} and {112} under high-temperature continuous growth conditions.[16] A scanning tunneling microscopy study of GaP grown at 525ºC found that APBs forming along {111} planes kinked to {112} and {113} long enough to shift to another {111} plane.[15]

Understanding the basic physical and chemical processes occurring at the GaP/Si interface during initiation of growth is important in order to reduce the density of APBs, and continues to be the subject of ongoing investigations.[4,10,13,16,18-20] The single-step explanation for APB formation means that APBs will occur whenever Ga and P atomic columns are present in the same atomic plane. However, when the epitaxial layer bonded to an atomically flat Si surface consisting entirely of either Ga or P, then heterovalent bonding would produce charge imbalance at the interface.[4,10] Such "abrupt" interfaces have been shown to be thermodynamically unfavorable.[4] In addition, a GaP/Si interface that consists entirely of Si-P bonds is believed to contribute to stacking faults and twins,[16] though it may produce fewer APBs.[18,19] Kroemer first hypothesized that in order to avoid both charge imbalance and APBs, Si atoms might migrate to neighboring layers so that Ga and P would be bonded to Si in equal numbers, but the atomic planes would still be entirely Ga or P.[10] Density functional theory calculations showed that the lowest energy configuration consists of a Si/Ga "intermixed" layer immediately above the Si substrate.[4] Since the activation energy for lateral diffusion is lower for Ga than for Si (and both are lower than P),[13] it has also been hypothesized that Ga, rather than Si, could be the atomic species that migrates in order to achieve charge neutrality and APB-free growth. [13,20]

However, kinetic factors such as fast pulsed deposition can prevent rearrangement even when it is thermodynamically favorable.[4]

A recent study has cast doubt on the entire single-step explanation for APBs, since plan-view scanning tunneling microscopy (STM) revealed that the average width of single-domain GaP (between APBs) across the substrate significantly exceeded the distance between monatomic Si surface steps.[21] Another recent study, this time using Monte Carlo simulations and TEM, claimed that GaP/Si heterostructures grown at low temperatures by MOVPE exhibited pyramidal features at the GaP/Si interface, with the Si(001) surface rearranging along {111} and {112} planes.[22] However, the validity of the DFT methodology used in this particular study has been called into question.[4] Nevertheless, APBs have been shown to form in GaP even on double-stepped Si surfaces, suggesting the importance of additional factors beyond double steps, such as controlling initial Ga or P coverage of the Si surface.[23]

Several experimental methods have been used to characterize APBs in GaP grown on Si, as well as the GaP/Si interfacial structure. Atomic force microscopy (AFM),[8,13,14,16] low-energy electron diffraction (LEED),[8] convergent beam electron diffraction (CBED),[8,24] reflection anisotropy spectroscopy (RAS),[11,13] cross-sectional and plan view transmission electron microscopy (TEM),[1,8,11,13,14,16] scanning transmission electron microscopy (STEM, including HAADF),[1,22,25] scanning electron microscopy (SEM),[18] secondary ion mass spectrometry (SIMS),[11] scanning tunneling microscopy (STM),[15] and x-ray diffraction (XRD),[1,18,25] have all contributed to the body of knowledge of APBs in GaP on Si and the GaP/Si interface. However, except for the results described later in this chapter and one figure in an additional study which identified the presence of APBs

despite double-steps on the Si surface,[23] no published study appears to have systematically characterized APBs with atomic-resolution TEM/STEM. Unlike other techniques, aberration-corrected STEM (AC-STEM) can directly image APBs as well as features of the GaP/Si interface at the atomic level.

3.2 Experimental details

The first set of GaP samples studied here were grown on Si(001) substrates using molecular beam epitaxy (MBE). The substrates were chemically etched, then preheated at 820ºC for 5 minutes. The GaP growth proceeded at 580ºC, and the nominal GaP layer thicknesses were 37nm, 250nm, 500nm, 1µm, and 2µm. All these samples except the one with 500-nm thickness were prepared for TEM observation by FIB (FEI Nova-200), and then characterized with TEM (Philips-FEI CM200) and AC-STEM (ARM-200F).[1]

Another GaP/Si(001) sample was grown by migration-enhanced epitaxy (MEE) at a substrate temperature of 440ºC on a Si substrate that was miscut at an angle of 4° towards a single <110> direction. The nominal GaP layer thickness was 50nm. Before growth, the Si substrate was pretreated in the same way as the samples grown by MBE. This GaP layer was grown with an initial P flux of 30 seconds, with subsequent 12 seconds of closed sources, followed by 184 cycles of the deposition loop: 1) 5 seconds Ga flux, 2) 1 second closed sources, 3) 8 seconds P flux, 4) 5 seconds closed sources. Cross-sections were prepared in two orthogonal directions by FIB (FEI Nova-200) so that the incident TEM beam direction would be either parallel and perpendicular to the miscut. These samples were imaged using AC-STEM (ARM-200F).[14]

All samples were also characterized by XRD using an X'Pert diffractometer. Coherent double-crystal (DC) ω-2θ and triple-crystal (TC) ω rocking curves (RCs) were taken around the Si (004) and GaP (004) reflections.[1]

3.3 Results and discussion

3.3.1 Characterization of defects

Table 3.1 compares the nominal MBE-grown GaP layer thicknesses to those measured from TEM images. When the layers were thin enough to be measured accurately from high magnification images, thicknesses were slightly less than their respective nominal values, with typical differences of ~3-4%.

Nominal Thickness (nm)	**Observed Thickness (nm)**
37	36±1
250	240±5
1000	965±5
2000	2000±100

Table 3.1: Nominal and observed thicknesses for GaP layers in MBE-grown GaP/Si heterostructures.

XTEM images of the entire GaP layer of the samples listed in table 3.1 are shown in figure 3.2, and figure 3.3 shows higher magnification images of the interfaces of samples with GaP layer thickness of 250nm and 1000nm. The defect density increases with increasing thickness, although there is variability across the field of view and thicker films show falloff with thickness, in agreement with XRD. However, even the sample with the thinnest GaP layer is not entirely defect-free. These results suggest that all

samples have entered either the second or third stage of defect formation, when the layer is either fully strained or partially relaxed, respectively, and defects have started to form. Thinner layers of GaP should be grown to determine the critical thickness for transition from the first stage to the second.

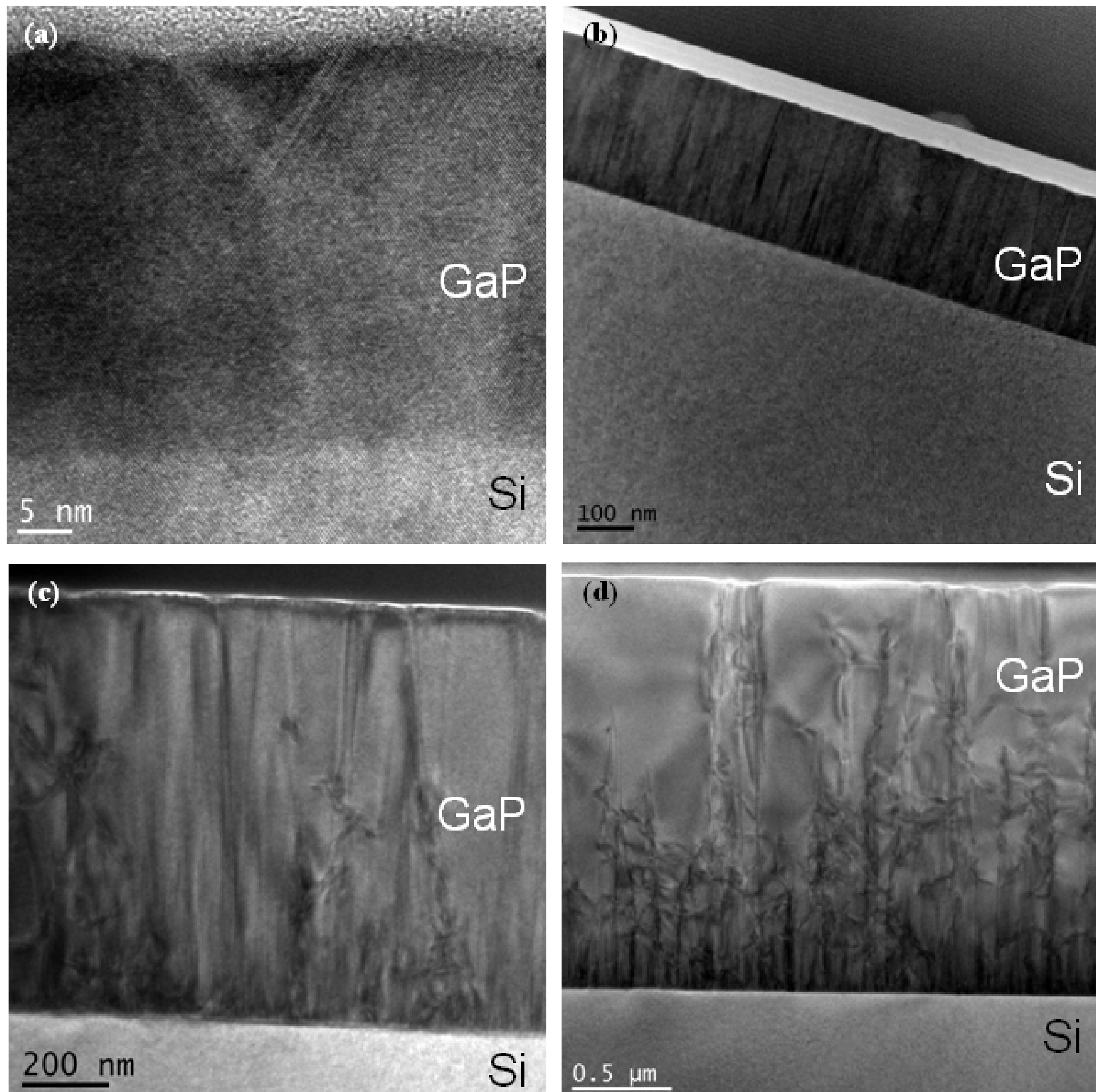

Figure 3.2: XTEM images of GaP/Si samples with GaP layer thicknesses of: a) 37nm, b) 250nm, c) 1000nm, and d) 2μm.

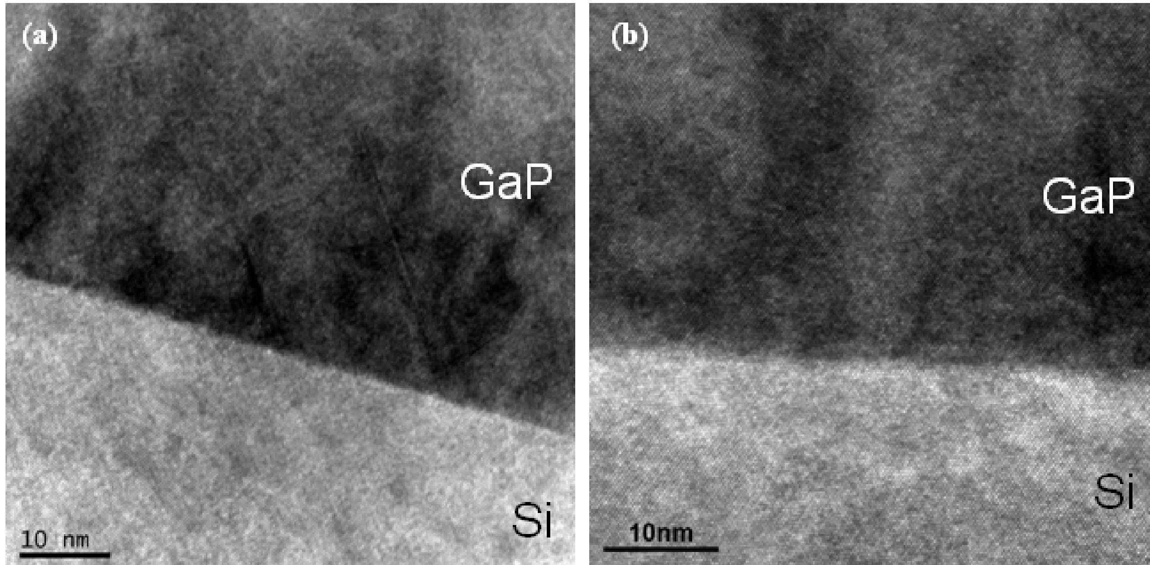

Figure 3.3: XTEM images of the GaP/Si interface of samples with GaP layer thicknesses: a) 250nm, and b) 1000nm.

Results from XRD examination are shown in figure 3.4. The DC RCs shown in figures 3.4a and c reveal that the relative positions of the GaP peak are only shifted for GaP layer thicknesses of 500nm and greater. These results indicate that the GaP is fully strained for layer thicknesses up to and including 250nm, and that partial relaxation has occurred for layer thicknesses of 500nm and greater. In addition, the TC RCs in figures 3.4b and d show a gradual increase in FWHM as the GaP layer thickness is increased, corresponding to decreased crystal quality with increasing layer thickness, which is in agreement with the TEM results. Taken together, figures 3.2 and 3.4 indicate that the critical thickness to transition from Stage Two to Stage Three relaxation likely occurs between 250nm and 500nm. It is noteworthy that the defect density in the 37-nm layer is low, but that is apparently not the case for the 250-nm layer. Thus it may be that net strain relaxation (Stage Three) requires a large number of defects.

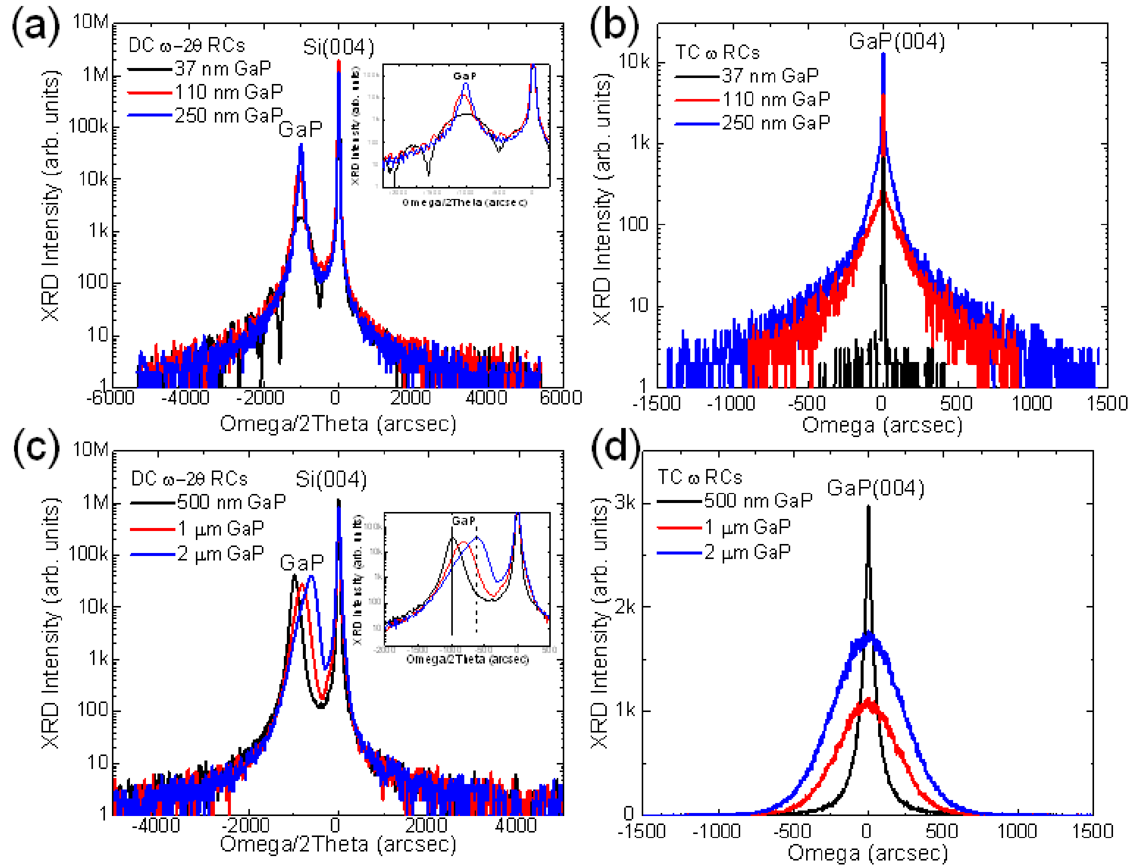

Figure 3.4: DC ω-2θ RCs for Si substrate and GaP layer thicknesses of: a) 37nm, 110nm, and 250nm; and c) 500nm, 1μm, and 2μm. TC ω RCs for: b) 37nm, 110nm, and 250nm; and d) 500nm, 1μm, and 2μm.

Most defects in all samples are observed to propagate upwards through the GaP layer from the GaP/Si interface, although figure 3.2a shows one defect that seems to originate at the top surface. Defects originating at the surface have been observed previously in metamorphic III-P/Si systems that are fully relaxed.[6] It was observed here only in the GaP layer of lowest thickness, which is most likely fully strained and where the growth is presumed to still be pseudomorphic. This observation indicates that these defects are not caused by strain relaxation.

Some defects originating at the interface terminate in the GaP layer before they reach the top surface. However, there are some threading dislocations visible in figure 3.2 b, c, and d that propagate through the entire thickness of the respective 250-nm, 1-µm, and 2-µm GaP layers. Thus, samples with these thicknesses may be unsuitable for applications as buffer layers. Alternately, it has been found that threading dislocation densities for the large lattice-mismatched GaAs/Si system have been reduced by subjecting the system to alternating tensile and compressive strain, which was accomplished through thermal expansion and contraction by taking the system through annealing at high and low temperatures.[6] If this annealing treatment were performed on the nearly-lattice matched GaP/Si system, it might possibly yield suitable GaP buffer layers of larger thicknesses. Another solution could be to grow layers of the dilute nitride GaP_xN_{1-x} rather than GaP, where the nitrogen concentration could be tuned to provide an exact lattice-match with Si and thereby reduce or even eliminate threading dislocations.

3.3.2 Observation of anti-phase boundaries

Anti-phase boundaries (APBs) are a common growth defect for polar-nonpolar epitaxial systems, and were commonly observed in GaP layers in high-resolution images during this study. Aberration-corrected STEM images of the 37-nm GaP/Si sample are shown in figure 3.5. Ga atomic columns appear with much brighter contrast than P atomic columns in dark-field STEM images, since the atomic number of Ga is more than double that of P. Thus, the growth polarity is easily determined from an intensity profile of a single column in the azimuthal direction, as clearly shown in figures 3.5b and c. The GaP layer is identified as P-polar in the top part of the image and Ga-polar in the bottom

part of the image. The APB visible in figure 3.5 lies along the {110} direction, and its actual location can be narrowed to within two rows of atoms, as shown by the yellow box in figure 3.5d. This appearance may indicate that the APB has a sideways step along the beam direction in this region.

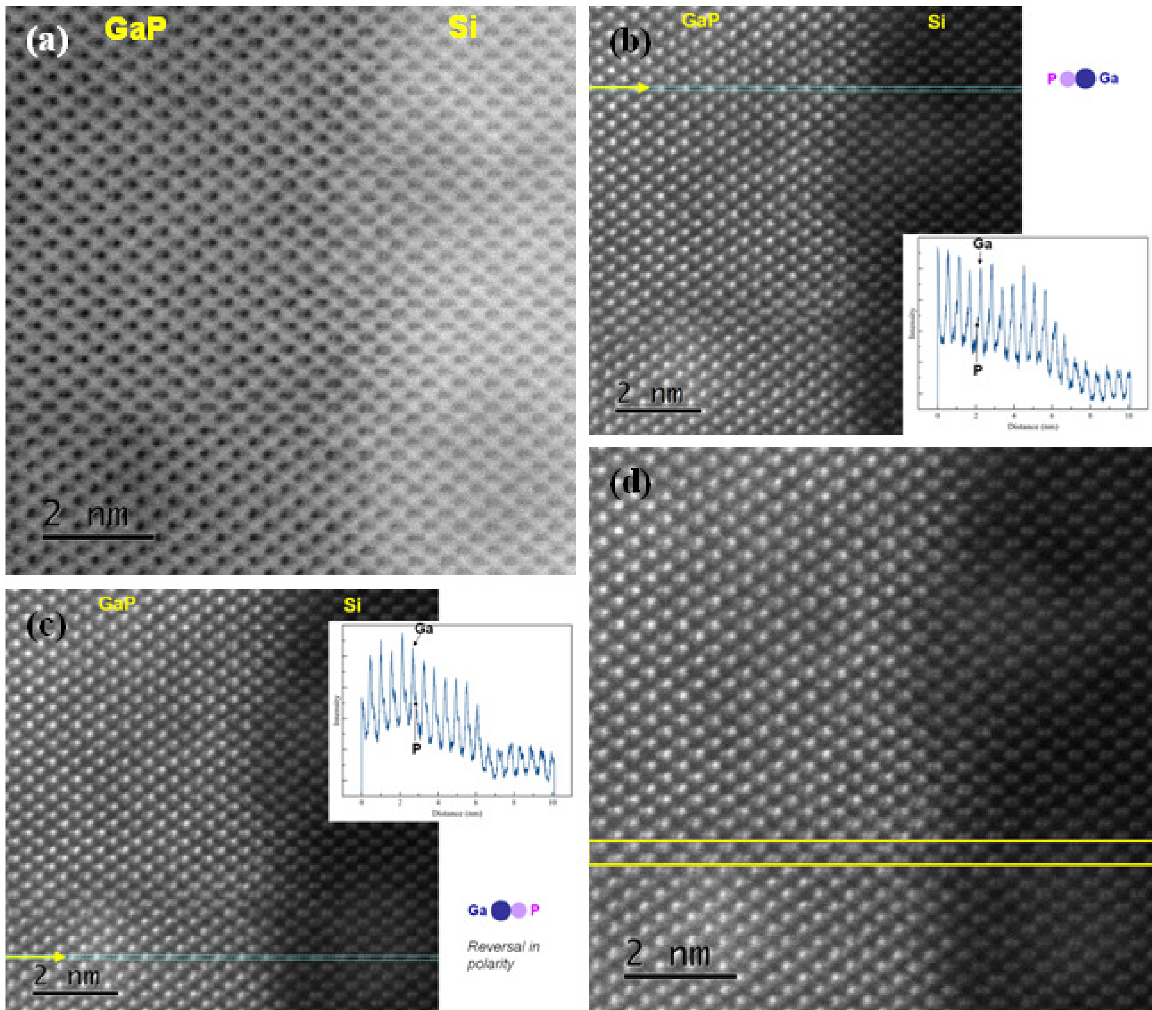

Figure 3.5: a) Large-angle BF STEM of GaP/Si interface for sample with GaP layer thickness 37nm, b), c) DF STEM images of same area, with GaP polarity and line profiles along the indicated rows, d) DF STEM of same area with APB location indicated.

Careful observation shows that the GaP/Si interface is not atomically flat across the interface, while the layer of intermediate intensity between the Si substrate and GaP layer also suggests that the interface is not flat along the beam direction through the sample thickness. This appearance could be due to an uneven Si substrate surface, but it could also indicate Si, Ga, or P interdiffusion across the interface, as seen in other III-V/IV heterostructures.[26] Moreover, there appears to be a possible thickness gradient in the GaP layer, as seen in figures 3.5b and c. Though not as evident in figure 3.5, other profiles of this same sample also showed a thickness gradient in the Si layer. This gradient complicates interpretation of line profiles and makes it more difficult to accurately estimate the interface width. In contrast, line profiles of the 250-nm GaP sample revealed that the projected thickness appeared to be relatively constant, so this latter sample was used to make an estimate of the interface width.

Figure 3.6a shows a HAADF image of the 250-nm GaP/Si sample. This and other images of the same sample were analyzed as follows. Five individual line profiles were taken, skipping a row of atomic columns so that the pairs of atomic columns, or "dumbbells," coincide. These profiles were selected from an area where the Si surface appeared to be relatively flat laterally, and were labeled a1-a5. One such arrangement is shown in figure 3.6b, and the average of these five intensity profiles is shown in figure 3.6c. This profile was fitted to a logistic "S" curve, given by the following equation:

$$y = \frac{L}{\left(1+e^{-k(x-z)}\right)} + b \qquad (5.1)$$

where y is intensity, x is position, z is the position of the midpoint of the interface, b is the y-intercept, k is related to the steepness of the curve/abruptness of the interface, and L

is the average intensity (minus the y-intercept) of the GaP layer. Zero percent intensity was set to the value of b, and one hundred percent was set to the value of b+L. The y-values of 10% and 90% intensity were estimated, followed by the corresponding x-values. The interface width was then identified as Δx, which is shown approximately by the gray boxes in figure 3.6c,d.

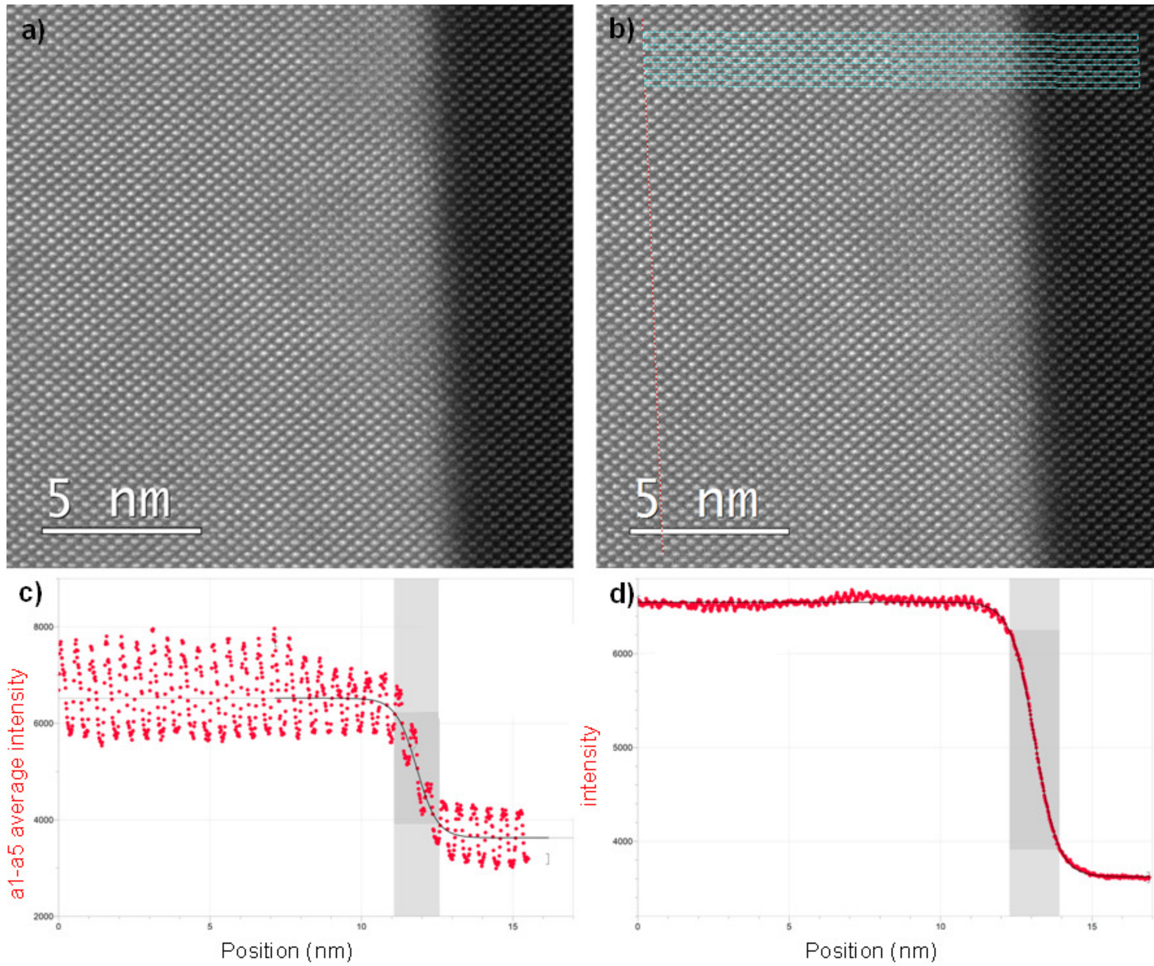

Figure 3.6: a) HAADF image of GaP/Si interface for GaP layer thickness 250nm, b) locations of intensity line profiles with average shown in c) and fitted to an S-curve. d) average intensity line profile across most of a), also fitted to an S-curve.

The process used to produce figures 3.6b,c was repeated by shifting each “a” profile down by one line, labeled b1-b5. Then profiles a6-a10 and b6-b10 were taken from another region in the same image. Each set (a1-a5, b1-b5, a6-a10, and b6-b10) was averaged, and each average was fit to an S-curve. These four average profiles were each taken from three HAADF images, and the results are shown in table 3.2. The similarly labeled profiles from different images have no relation to each other. The uncertainty displayed in the table is propagated from the error in the fitting parameters, but the actual uncertainty is unclear since this work did not attempt to quantify elemental composition, but only to estimate the diffusion width. One significant figure may be most appropriate, leading to a result of 1.7±0.3nm interface width for this sample.

	a1-a5 (±0.2nm)	b1-b5 (±0.2nm)	a6-a10 (±0.2nm)	b6-b10 (±0.2nm)	(almost) entire image
HAADF 1 Δx (nm)	1.6	1.5	1.8	1.6	1.8
HAADF 2 Δx (nm)	1.4	1.3	1.8	1.8	1.7
HAADF 3 Δx (nm)	1.6	1.4	1.6	1.6	1.7
HAADF 4 Δx (nm)					1.7
HAADF 5 Δx (nm)					1.7
HAADF 7 Δx (nm)					1.7
HAADF 19 Δx (nm)					2.1
HAADF 23 Δx (nm)					1.8

Table 3.2: Interface widths calculated from 10%-90% intensity of S-curve fits of HAADF images of GaP/Si of 250nm GaP layer.

Figure 3.6d shows an intensity profile averaged across almost the entire image in figure 3.6a. The profile was again fitted to an S-curve and the interface width calculated in the same way as the previous profiles. The widths from this and 7 other images are also listed in table 3.2. The interface widths resulting from profiles taken across the entire image are slightly larger than those from smaller regions in the same images, indicating that the Si surface is not completely flat.

Even in profiles taken from smaller regions, specifically chosen where the Si surface appeared to be relatively flat, the interface is not atomically abrupt. From table 3.2, diffusion causes an estimated interface width of 1.7±0.3nm. This estimate directly contradicts theoretical predictions that Si intermixes only into the next immediate layer above the original substrate surface.[4] However, sigmoidal composition profiles at III-V/III-V interfaces across growth methods have been reported previously, suggesting finite diffusion and finite minimum interface widths as fundamental growth properties, at least for materials with similar crystal structure.[26] The S-curve and finite diffusion lengths observed in this chapter suggest that this finding of a finite interface width extends to the GaP/Si system. Despite diffusion and an uneven Si surface, no evidence has been observed for a pyramidal structure at the interface, as was previously proposed.[22]

Even with a 0.1° miscut in a [110] direction, anti-phase boundaries are liable to be produced that may propagate differently in different directions.[9] Thus, the sample grown by MEE was prepared for cross-sectional AC-STEM observations in orthogonal directions. Figures 3.7 and 3.8-3.9 compare HAADF images of the GaP/Si interfaces for the nominally flat Si surface and for the 4° miscut, respectively. No APBs were observed

for the projection corresponding to a flat interface, and each image showed a P-polar GaP layer. In contrast, the interface for the miscut Si was revealed as primarily Ga-polar, but with several APBs (figure 3.9). It is noteworthy that in both orientations, the Si surface is not atomically flat, and the interface is not abrupt, as was the case in the MBE-grown samples. The MEE growth method should prevent thermodynamically driven atomic rearrangements, so the lack of abruptness for both MEE and MBE growth is evidence in favor of the hypothesis that some interdiffusion is unavoidable for the GaP/Si system.

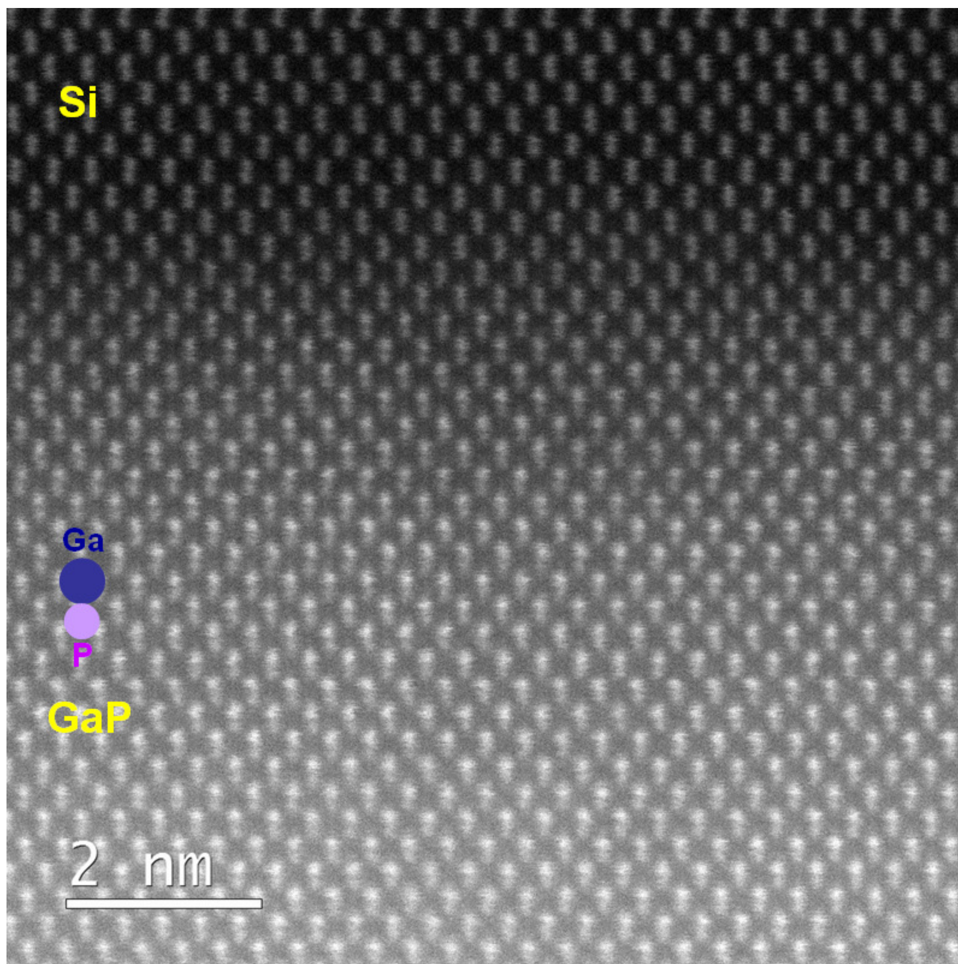

Figure 3.7: HAADF image of GaP/Si sample grown by MEE. In this projection, the Si surface was nominally flat. The GaP layer was P-polar in all observed images.

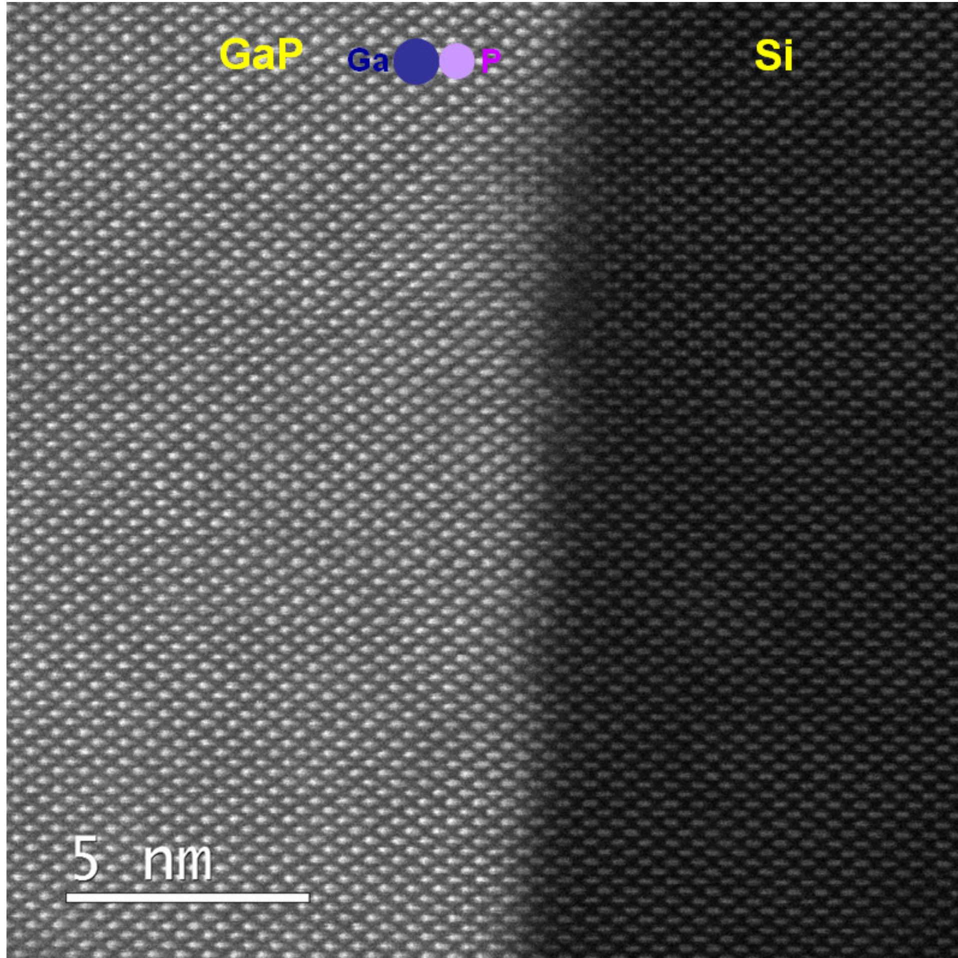

Figure 3.8: HAADF image of GaP/Si sample grown by MEE showing the Si surface miscut by 4º in this projection.

Figure 3.9a shows a HAADF image of a region of the MEE sample clearly showing the 4º miscut. Several APBs are visible in this region. Intensity line profiles were taken to determine the local polarity, as shown in figures 3.9b-d. The locations of these profiles are shown in figure 3.9a. As shown in figure 3.9b and d, the right and left sides of the image show Ga-polarity, as visible in figure 3.8. The intensity line profile in

figure 3.9c shows that the GaP is P-polar near the interface (circled in red on the profile), while it is Ga-polar farther from the interface (circled in green on the profile). Between these two clearly opposite polarities is a region of unclear polarity (between the red and green circles on the profile). The APB exists within this region.

Further analysis was performed on the entire image, and the result is shown in figure 3.9e. The boxed areas indicate regions between opposite polarity in which APBs exist. There seem to be parallel {110} APBs extending from the interface. From the literature, APBs in zincblende materials are expected to kink to {111}, {112}, or {113} planes.[15,16] GaP has the zincblende structure, so its lattice constant should be equal in x, y, and z directions. Therefore, in a two-dimensional image which is a projection of a {110} plane, the ratio of orthogonal distances should be 1:1.41 for {111} APBs, 2:1.41 or 2.82:1 for {112}, and 3:1.41 or 4.23:1 for {113}. In figure 3.9e, the minimum ratio for an APB kinking from the {110} on the right-hand side of the image is approximately 4:1, achieved if the APB followed the hypotenuse of the red dashed triangle. (On the left-hand side, {111}, {112}, or {113} kinking may be possible.) This result indicates that the APB on the right-hand side is kinking to either {113} or higher-order planes to annihilate.

3.4 Conclusions

TEM and XRD results of GaP/Si samples grown by MBE with increasing GaP layer thickness indicate that growth defects form even with a layer thickness as thin as 37nm, and that strain relaxation starts to occur for thicknesses somewhere between 250nm and 500nm. A large density of defects, as observed in the 250nm sample, may be necessary before strain relaxation starts to occur in this system. The presence of these

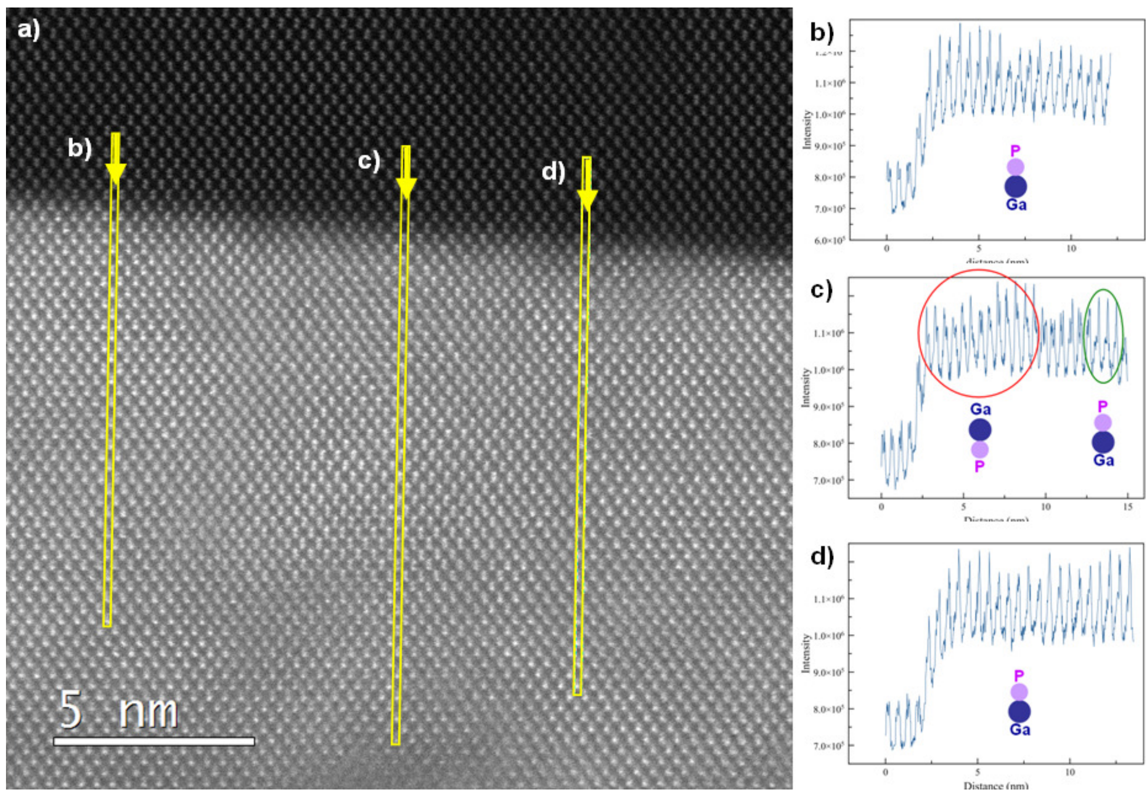
a)
b)
c)
d)
5 nm
b)
P
Ga
c)
Ga
P
P
Ga
d)
P
Ga
Intensity
Distance (nm)

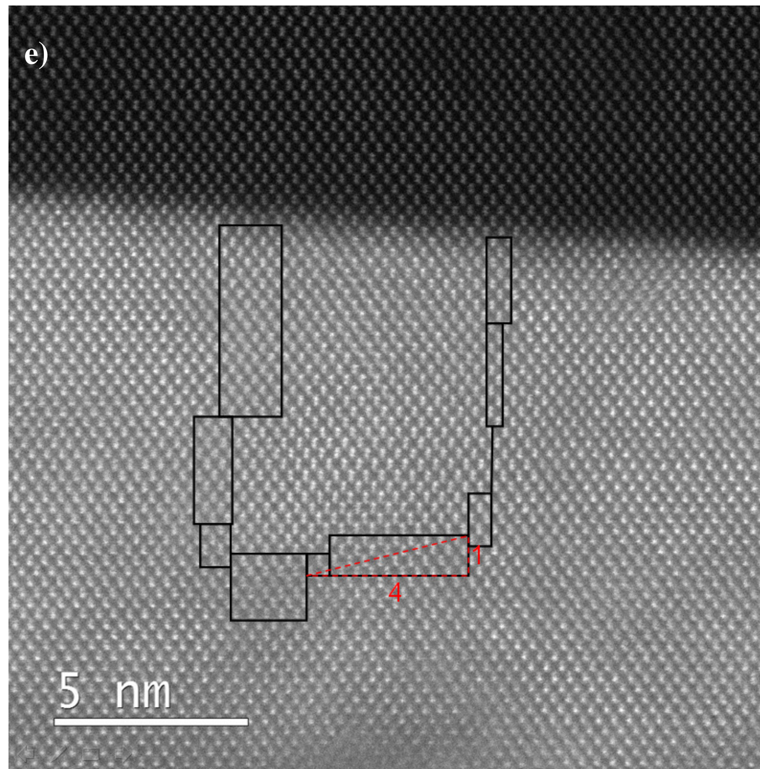
e)
1
4
5 nm

Figure 3.9: a) HAADF image of GaP/Si sample grown by MEE. In this direction, the Si surface was intentionally miscut by 4º. b) and d) also show line profiles which reveal the GaP to be Ga-polar. The line profile in c) shows a P-polar region near the interface followed by an APB followed by a Ga-polar region. e) boxes that contain APBs as determined by the method shown in c). The red dashed triangle in e) indicates the minimum ratio of horizontal to vertical distance of an APB in this region, with the APB given by the hypotenuse of the triangle.

defects should preclude GaP layers of thicknesses ≥250nm from being used as buffer layers for III/V growth on Si. Anti-phase boundaries were observed propagating along {110} planes in both MBE- and MEE-grown GaP/Si.

The GaP/Si interface in both MBE- and MEE- grown samples was not compositionally abrupt. Diffusion producing an interface width of ~1.7nm was observed in an MBE-grown sample with a 250-nm GaP layer. Diffusion was observed to occur across growth methods and layer thicknesses indicating that interdiffusion is a fundamental property of GaP/Si growth. The Si surface was also not flat, possibly indicating that the substrate may not have been atomically flat to begin with, or that Si surface rearrangement had occurred, the latter previously predicted to produce double steps on the Si surface that prevented APBs.[10]

References

1. Zhang, C., Boley, A., Maroc, A., Faleev, N., Smith, D.J., and Honsberg, C.B. 2018. *Journal of Crystal Growth* **503**: 36.

2. New Semiconductor Materials Characteristics and Properties. 2001. Ioffe Physico-Technical Institute.

3. Németh, L., Kunert, B., Stolz, W., and Volz, K. 2008. *Journal of Crystal Growth* **310**: 4763.

4. Romanyuk, O., Supplie, O., Susi, T. May, M.M., and Hannappel, T. 2016. *Physical Review B* **94**: 155309.

5. Maros, A., Faleev, N., King, R.R., Honsberg, C.B., Convey, D., Xei, H., and Ponce, F.A. 2016. *Journal of Vacuum Science and Technology B* **34**: 02L113.

6. Li, Q. and Lau, K.M. 2017. *Progress in Crystal Growth and Characterization of Materials* **63**: 105.

7. Tsao, J.Y., Dodson, B.W., Picraux, S.T., Cornelison, D.M. 1987. *Physical Review Letters* **59**: 2455.

8. Beyer, A., Ohlmann, J., Liebich, S., Heim, H., Witte, G., Stolz, W., and Volz, K. 2012. *Journal of Applied Physics* **111**: 083534.

9. Beyer, A., Németh, I., Liebich, S., Ohlmann, J., Stolz, W., and Voltz, K. 2011. *Journal of Applied Physics* **109**: 083529.

10. Kroemer, H. 1987. *Journal of Crystal Growth* **81**: 193.

11. Feifel, M., Ohlmann, J., Benick, J., Rachow, T., Janz, S., Hermle, M., Dimroth, F., Belz, J., Beyer, A., Volz, K., and Lackner, D. 2017. *IEEE Journal of Photovoltaics* **7**: 502.

12. Tea, E., Vidal, J., Pedesseau, L., Cornet, C., Jancu, J.-M., Even, J., Laribi, S., Guillemoles, J.-F., and Durand, O. 2014. *Journal of Applied Physics* **115**: 063502.

13. Döscher, H., Supplie, O., Brückner, S., Hannappel, T., Beyer, A., Ohlmann, J., and Voltz, K. 2011. *Journal of Crystal Growth* **315**: 16.

14. Németh, I., Kunert, B., Stolz, W., and Voltz, K. 2008. *Journal of Crystal Growth* **310**: 1595.

15. Prohl, C., Döscher, H., Kleinschmidt, P., Hannappel, T., and Lenz, A. 2016. *Journal of Vacuum Science & Technology A: Vacuum, Surface, and Films* **34**: 031102.

16. Voltz, K., Beyer, A., Witte, W., Ohlmann, J., Németh, I., Kunert, B. and Stolz, W. 2011. *Journal of Crystal Growth* **315**: 37.

17. Rubel, O. and Baranovskii, S.D. 2009. *International Journal of Molecular Sciences* **10**: 5104.

18. Dixit, V.K., Ganguli, T., Sharma, T.K., Singh, S.D., Kumar, R., Porwal, S., Twiari, P., Ingale, A., and Oak, S.M. 2008. *Journal of Crystal Growth* **310**: 3428.

19. Yamane, K., Kawai, T., Furukawa, Y., Okada, H., and Wakahara, A. 2010. *Journal of Crystal Growth* **312**: 2179.

20. Ratcliff, C., Grassman, T.J., Carlin, J.A., and Ringel, S.A. 2011. *Applied Physics Letters* **99**: 141905.

21. Lucci, I., Charbonnier, S., Pedesseau, L., Vallet, M., Cerutti, L., Rodriguez, J.-B., Tournié, E., Bernard, R., Létoublon, A., Bertru, N., Le Corre, A., Rennesson, S., Semond, F., Patriarche, G., Largeau, L., Turban, P., Ponchet, A., and Cornet, C. 2018. *Physical Review Materials* **2**: 060401(R).

22. Beyer, A., Stegmüller, A., Oelerich, J.O., Jandieri, K., Werner, K., Mette, G., Stolz, W., Baranovskii, S.D., Tonner, R., and Voltz, K. 2016. *Chemistry of Materials* **28**: 3265.

23. Ping Wang, Y., Stodolna, J., Bahri, M., Kuyyalil, J., Thanh, T.N., Almosni, S., Bernard, R., Tremblay, R., Da Silva, M., Léroublon, A., Rohel, T., Tavernier, K., Largeau, L., Patriarche, G., Le Corre, A., Ponchet, A., Magen, C., Corent, C., and Durand, O. 2015. *Applied Physics Letters* **107**: 191603.

24. Cohen, D., McKernan, S., and Carter, C.B. 1999. *Microscopy & Microanalysis* **5**: 173.

25. Wang, Y.P., Letoublon, A., Thanh, T.N., Bahri, M., Largeau, L., Patriarche, G., Cornet, C., Bertru, N., Le Corre, A., and Durand, O. 2015. *Journal of Applied Crystallography* **48**: 702.

26. Luna, E., Guzmán, A., Trampert, A., and Álvarez, G. 2012. *Physical Review Letters* **109**: 126101.

CHAPTER 4

MICROCRYSTALLINE Si FOR PASSIVATED Si SOLAR CELLS

This chapter describes the characterization of microcrystalline Si (μc-Si) grown as an alternative to *c*-Si-passivated by *a*-Si. This work was carried out in collaboration with the research group of Professor Zachary Holman at Arizona State University, who performed sample growth, UV Raman spectroscopy, and ellipsometry. Results of this work have been published.[1]

4.1 Role of microcrystalline Si in Si heterojunction solar cells

Silicon heterostructures have achieved the highest efficiencies of all Si-based solar cells, with a current record efficiency of 27.6%.[2] The structure of a typical Si heterojunction (SHJ) solar cell is shown in figure 4.1a.[3] Light enters at the top surface of the cell and travels downward through into the crystalline Si (*c*-Si) layer. Dangling bonds at the *c*-Si surface can act as recombination centers, so Si solar cells of high efficiency need *a*-Si layers to passivate the *c*-Si surfaces.[4] However, the front *a*-Si (*p*+) layer and transparent conductive oxide (TCO) suffer from parasitic absorption,[5] when a photon is absorbed without generating an electron-hole pair. As illustrated in figure 4.1b, doped μc-Si has been proposed as an alternative material to the *p*+-type *a*-Si in SHJs.[6,7] Microcrystalline Si consists of crystallites, either interconnected or segregated, which are surrounded by amorphous Si.[8] Because of its lower absorption coefficient, a thin layer of μc-Si at the front end of the cell does not absorb as many photons as *a*-Si. Thus, substituting μc-Si (*p*+) for *a*-Si (*p*+), as illustrated in figure 4.1, reduces the parasitic absorption and should increase both the current density and the fill factor of the cell.[6]

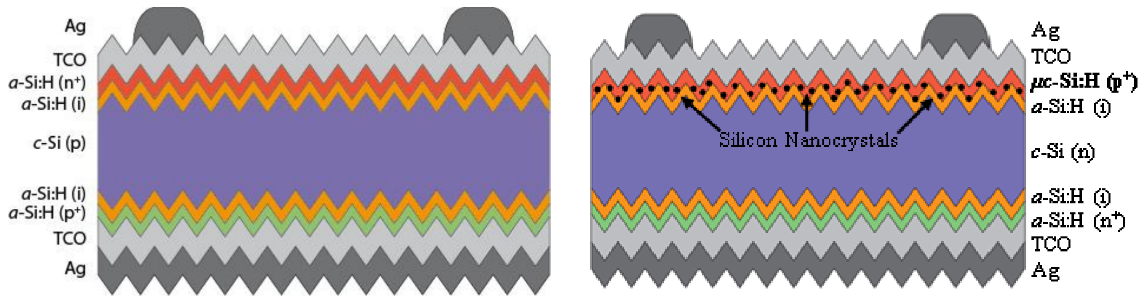

Figure 4.1: Structures of (a) typical SHJ solar cell,[3] and (b) modified SHJ solar cell with a *μc*-Si (*p*+) layer replacing the *a*-Si (*p*+) layer.[7]

4.2 Growth and characterization of microcrystalline Si

The growth of *μc*-Si on *a*-Si, as illustrated in figure 4.1b, is expected to result in crystallites that are conical in shape. The process generally exhibits two main transitions: (1) from purely amorphous to a mixture of amorphous and microcrystalline, and (2) from the mixture to single-phase *μc*-Si.[9] The exact reason for the nucleation of crystalline material from amorphous is not yet known: it may be due to diffusion of H [9] or due to stress resulting from the higher number of nearest neighbors in the amorphous material.[8,9] However, it has been shown to follow roughening of the amorphous layer immediately before crystalline formation.[9] The layer thicknesses at which these transitions occur depend on the ratio of H_2 to SiH_4 gases during deposition, as well as total gas pressure, plasma power, substrate material, and substrate temperature. The ratio of gases also affects the open-circuit voltage of the resulting structure.[9]

It is important to determine the fraction of Si crystallinity in the microcrystalline material. An increasing percent of *μc*-Si_xC_{1-x}:H has been correlated with increasing dark current, and the percent crystallinity was even believed to influence the mechanism of conductivity.[8] To determine percent crystallinity, Raman spectroscopy and ellipsometry

are attractive methods because measurements can be performed quickly, even *in situ*.[1] However, when investigating percent crystallinity of thin films with Raman spectroscopy, the customary laser wavelength of 532nm is not appropriate. Figure 4.2 shows the penetration depths of this wavelength of light in various types of Si. The penetration depths in all but amorphous crystalline are near or above 100nm, which is too large to characterize thin layers. A 325-nm laser, in the ultraviolet (UV) region of the electromagentic spectrum, is a better choice for thin-film characterization since the penetration depths are all less than 10nm.[1]

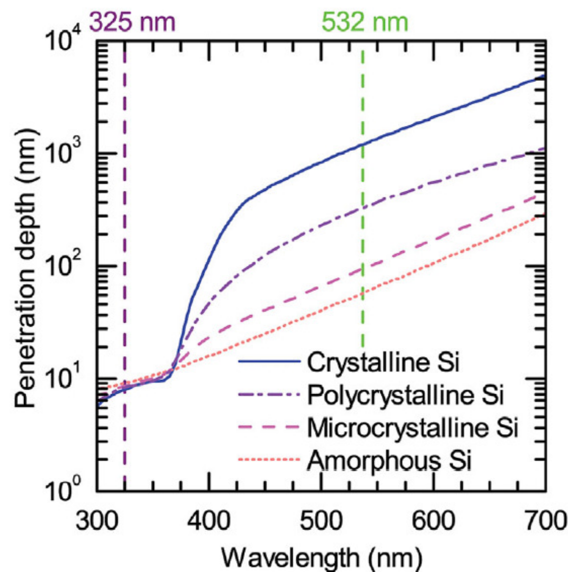

Figure 4.2: Laser light penetration depths for crystalline, polycrystalline, microcrystalline, and amorphous Si as a function of wavelength. 532nm is the customary wavelength used in Raman spectroscopy. However, due to the reduced penetration depth, light of wavelength 325nm is more appropriate to probe thin films such as those in this study.[1]

4.3 Experimental details

Three *μc*-Si/ *a*-Si/ *c*-Si samples (A, B, and C) with different layer thicknesses, were grown using plasma-enhanced chemical vapor deposition (PECVD) at 250ºC.[1] A fourth sample (D) was grown using a nanoparticle seed layer deposited on the *a*-Si. Cross-sectional transmission electron microscope (TEM) specimens of samples A-C were prepared using an FEI Nova200 focused-ion beam (FIB), and a similar specimen of sample D was prepared using the standard polishing, dimpling, and ion milling technique. All four samples were imaged using an FEI-Phillips CM200 FEG TEM. UV Raman spectroscopy was performed on sample C at a laser wavelength of 325nm. Ellipsometry was also performed on sample C. The results of TEM, UV Raman spectroscopy, and ellipsometry were compared to determine the percent crystallinity of the *μc*-Si in sample C.

4.4 Results and discussion

Figures 4.3 (a) and (b) show low-magnification images of the two microcrystalline samples. The initial part of the microcrystalline layer seems to be purely amorphous, although a thin brighter layer is present between the *a*-Si and *c*-Si, which is likely to be native oxide. Layer thicknesses were measured. In both cases, the amorphous layer exhibited a thickness that was uniform throughout the sample, while the microcrystalline layer had an uneven surface and its thickness was not constant. However, this surface could undergo further texturing, which reduces reflectance, and the photons experience total internal reflection once inside the material.[2]

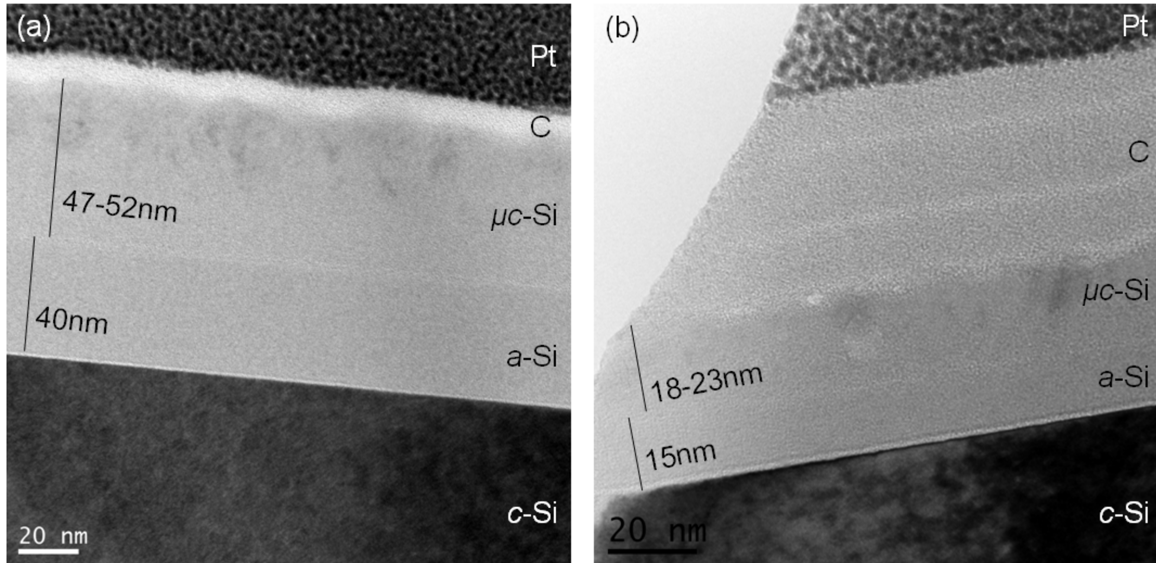

Figure 4.3: Microcrystalline Si samples (a) A and (b) B, grown on *a*-Si on *c*-Si. The C and Pt layers were deposited in the FIB to protect the surface.

Figure 4.4 shows high-resolution TEM images of samples A and B. The *μc*-Si is multigrain, with amorphous regions sometimes separating grains, which thus provide passivation. The distinction between the amorphous and microcrystalline layers is not as distinct as it appears in figure 4.3, but the onset of crystallinity in figure 4.4b occurs at a distance greater than 15nm from the *c*-Si interface, confirming the initial purely amorphous growth of the microcrystalline layer.

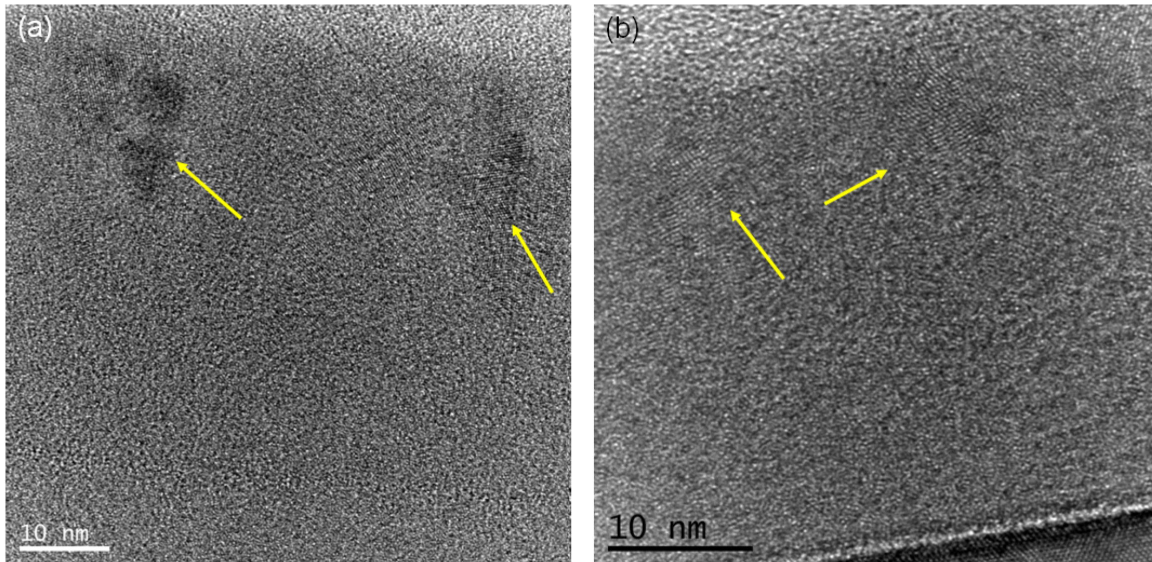

Figure 4.4: HRTEM images of the μc-Si layer of samples (a) A and (b) B. Multiple nanocrystalline grains, some of which are indicated by yellow arrows, are visible above amorphous material.

This appearance of amorphous material before the microcrystalline growth could be due to the random location of the TEM cross section within the bulk sample. If the crystalline growth is conical, then only a cross section which sliced directly through the base tip of the cone would reveal where the crystalline growth began. However, this explanation alone seems unlikely to account for the sheer amount of amorphous material at the initial *μc*-Si layer growth, since all the crystallites seem to originate at approximately the same height about halfway up the nominally microcrystalline layer. In an attempt to achieve microcrystalline growth throughout the entire layer in sample D, nanoparticles were deposited on top of the *a*-Si layer, in order to seed the growth of the crystallites. Figure 4.5 shows the growth structure and cross-sectional TEM images of sample D.

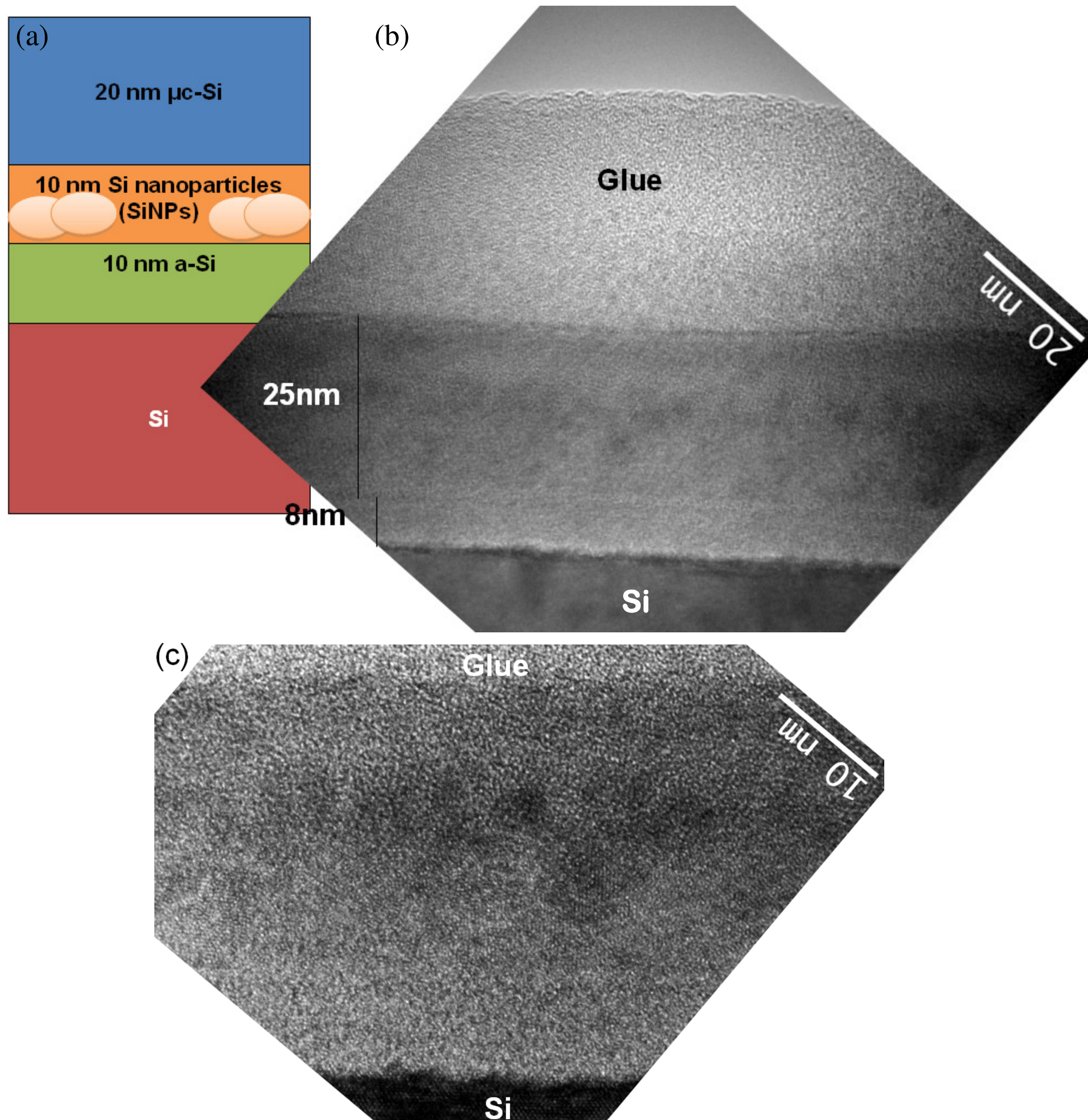

Figure 4.5: (a) Nominal growth structure and (b), (c) cross-sectional TEM images of sample D, with nanoparticle seed layer to induce microcrystalline growth immediately at the μc-Si/a-Si interface.

The microcrystalline growth seems to originate at the μc-Si/a-Si interface, as expected. However, the crystallites do not extend through the entire thickness of the layer, and amorphous material now occupies the upper half of the layer instead of the lower half,

as in samples A and B. The nanocrystal seeding seems to be an effective method to induce microcrystalline growth, but further optimization of growth parameters appears to be necessary to tune the thickness of the microcrystalline layer.

To determine the percent crystallinity in μc-Si, TEM is not a suitable bulk measurement tool. TEM provides two-dimensional observation, so making three-dimensional conclusions requires additional measurement tools. Thus, it is necessary to identify another suitable tool to provide that information. TEM can play a helpful role in this determination. Comparing measurements from other tools with results from TEM images can still provide a rough guide to the accuracy of these other tools. Figure 4.6(a) shows UV Raman spectroscopy and ellipsometry measurements at depths corresponding to the TEM image of sample C in figure 4.6(b). Ellipsometry clearly does not follow the general pattern of crystallinity in the TEM image. It indicates a region of 70% crystallinity sandwiched between two regions of 0% crystallinity, both only 10nm away from the 70% region. Furthermore, the 0% crystallinity measurement at 30nm is in direct contradiction with the apparent crystallinity visible in the TEM image at that depth location. For this sample, it was difficult to find a model whose fit to the ellipsometry data produced a low root-mean-square error (RMSE). For these reasons, it appears that ellipsometry is unsuitable for measuring percent crystallinity of thin-film μc-Si samples, such as those being studied in this work.

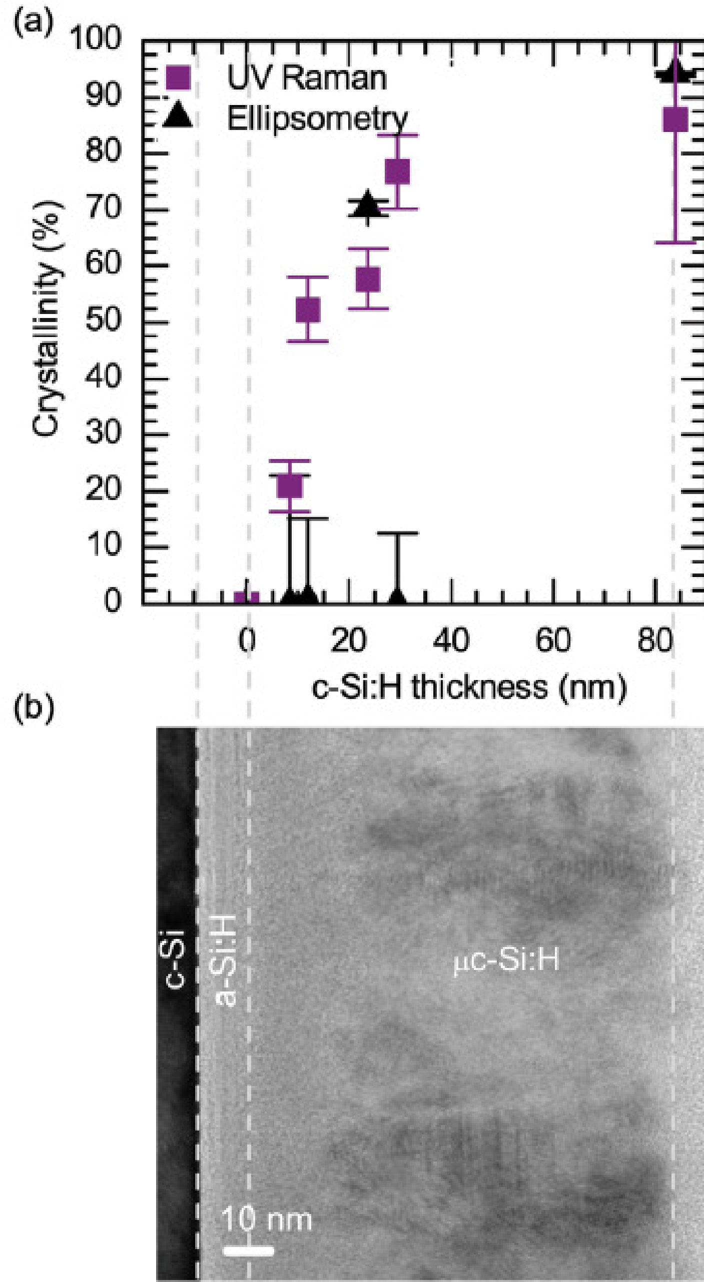

Figure 4.6: (a) UV Raman and ellipsometry measurements of percent crystallinity as a function of location corresponding to (b) cross-sectional TEM image of sample C. UV Raman spectroscopy provides a better qualitative match than ellipsometry to the TEM image.

Raman spectroscopy at a wavelength of 325nm provided a better qualitative match to the crystallinity observed in the TEM image in figure 4.5b. The onset of crystallinity according to Raman is slightly before TEM. However, it is possible that crystallinity would occur closer to the amorphous layer in other cross sections at different locations along the beam direction. If the microcrystalline growth is conical, then this imaged cross section clearly does not cut through the base point of the cone. Thus, the onset of crystallinity might be expected to be closer to the amorphous layer in another cross section, as indicated by the UV Raman results.

Although it is not possible from the single image in figure 4.6b to determine whether the crystallinity indeed gradually increases as suggested by Raman, and as would be the case if the growth were indeed conical, the TEM image shows that the sample is at least crystalline in the same regions suggested by Raman. For these reasons of qualitative agreement, while the accuracy of UV Raman spectroscopy is not directly confirmed by TEM, the results seem promising. It is also noteworthy that using parameters measured by Raman in the ellipsometry fit resulted in a lower RMSE, further indicating the accuracy of Raman measurements.

4.5 Conclusions

Using nanoparticles to seed the growth of *μc*-Si on *a*-Si produced a microcrystalline phase immediately, whereas samples grown without nanocrystals first produced amorphous growth with an eventual transition to microcrystalline material. However, the microcrystalline growth seeded by nanoparticles was followed by

amorphous growth. A finer tuning of growth parameters is necessary to optimize microcrystalline growth.

Relative qualitative agreement between TEM and UV Raman spectroscopy measurements indicates that the latter is a promising technique to determine the percent crystallinity in μc-Si thin films. Clear disagreement between TEM and ellipsometry indicates the unsuitability of ellipsometry for the same task.

References

1. Carpenter, J.V. III, Bailly, M., Boley, A., Shi, J., Minjares, M., Smith, D.J., Bowden, S., and Holman, Z.C. 2017. *Physica Status Solidi B* **254**: 1700204.

2. National Renewable Energy Laboratory. 2017. Best Research-Cell Efficiencies.

3. Ballif, C., Descoeudres, A., and DeWolf, S. 2012. Reproduced in Ecole Polytechnique Federale de Lausanne, “Using amorphous and monocristalline silicon together, researchers set new efficiency record for photovoltaic cells.” Omnicron Tech Ltd: Phys.org.

4. Ganapati, V., Miller, O.D., and Yablonovitch, E. 2014. *IEEE Journal of Photovoltaics* **4**: 175.

5. Holman, Z.C., Descoeudres, A., Barraud, L., Fernandez, F.Z., Seif, J.P., De Wolf, S., and Ballif, C. 2012. *IEEE Journal of Photovoltaics* **2**: 7.

6. Seif, J.P., Descoeudres, A., Nogay, G., Hänni, S., de Nicolas, S.M., Holm, N., Geissbühler, J., Hesser-Wyser, A., Duchamp, M., Dunin-Borkowski, R.E., Ledinsky, M., De Wolf, S., and Ballif, C. 2016. *IEEE Journal of Photovoltaics* **6**: 1132.

7. Carpenter, J., Bailly, M., Bowden, S., and Holman, Z. 2015. “Characterization of Microcrystalline Silicon in Heterojunction Solar Cells” [Poster]. QESST Site Visit, Arizona State University.

8. Demtchelis, F., Pirri, C.F., and Tresso, E. 1993. *Philosophical Magazine B* **67**: 331.

9. Collins, R., Ferlauto, A., Ferreira, G., Chi Chen, J.K., Kova, R., Lee, Y., Pearce, J., and Wronski, C. 2003. *Solar Energy Materials & Solar Cells* **78**: 143.

CHAPTER 5

Al-INDUCED CRYSTALLIZATION OF a-Ge AND LAYER EXCHANGE

This chapter describes structural and chemical characterization of Al/Ge and Ge/Al systems deposited on glass substrates. This work was carried out in collaboration with the group of Professor Freundlich at University of Houston, where Kaveh Shervin performed the sample growth and x-ray diffraction (XRD) measurements.

5.1 Utility of Ge-based solar cells and metal-induced crystallization

Germanium has been utilized as a semiconductor for decades, and was initially preferred over silicon because its lower melting point made it possible to attain greater purity than for silicon.[1] Even though use of Si has since overtaken Ge for device applications, Ge still offers advantages. It is an excellent candidate for tandem solar cells or as the substrate material in GaAs solar cells, in large part because of its small lattice mismatch with GaAs. The indirect band-gap energy of Ge (0.66 eV) also allows absorption of longer-wavelength photons than Si (1.12 eV) and GaAs (1.42 eV).[2] The hole mobility in Ge is also more than four times greater than for Si or GaAs.[2]

Both *c*-Ge and *c*-Si can be grown at relatively low expense via metal-induced crystallization (MIC) and layer exchange. In this approach, amorphous Ge or Si is deposited on a metal, often Al.[3] Upon heating, the metal and amorphous layer exchange places, and the amorphous layer is crystallized. The metal is then removed with an etchant. MIC and layer exchange enable *c*-Ge and *c*-Si growth even on glass substrates, substantially reducing the cost of production.[3]

Recently, a quantum efficiency of 70% was achieved in GaAs thin films grown epitaxially on Ge(111) layers which had been crystallized by Al and had undergone layer exchange.[4] When compared with the ~80% quantum efficiency for GaAs grown on standard *c*-Ge, growth on MIC Ge seems appealing as a less expensive alternative for photovoltaic device applications.[4]

5.2 Mechanisms of metal-induced crystallization and layer exchange

Metal-induced crystallization is a solid-state process that occurs below the eutectic temperature, which is approximately 420ºC in the Al-Ge system.[5] While the driving force for the MIC reaction is widely accepted as the lower free energy of *c*-Ge compared with *a*-Ge,[6] the mechanism remains controversial. It was first observed that Si crystallizes at a lower temperature in the presence of Al, and early studies focused on Si rather than Ge. In one proposed mechanism, free electrons at Al grain boundaries weaken the amorphous Si bonds, and Si crystallizes while diffusing through the grain boundaries.[7] Another theory involves a reactive grain boundary, in which Si reacts with metal atoms trapped at the grain boundary to form a metal-silicide.[3] In metal-induced crystallization/ layer exchange studies of Si, regardless of the proposed mechanism, the crystallization and layer exchange occur simultaneously.

While metal-induced crystallization is sometimes considered as a single process, experimental results indicate that the mechanism proceeds differently for Ge than for Si. The crystallization rates of Ge and Si have been contrasted, and it was found that Ge crystallized quickly and completely, while Si crystallized gradually over a longer period of time.[8] From calculations of the critical nucleation thicknesses of Ge and Si, it was

determined that Ge can crystallize at the Al interface, while Si and SiGe alloys require Al grain boundaries to crystallize.[8,9] However, if Ge does not crystallize at and diffuse through the grain boundary, then Al-Ge layer exchange must occur separately from Ge crystallization, and the mechanism must differ from the proposed mechanisms for Al-Si layer exchange and Si crystallization. The exact mechanism is yet unknown, which is the motivation for the samples studied in this work. The research described here is an investigation into the mechanism of Al-Ge crystallization and layer exchange.

5.3 Experimental details

The samples studied were grown by evaporating either Al or Ge onto SiO_2, then leaving the sample in air for varying lengths of time to form a surface oxide, then evaporating the remaining layer (Ge or Al) onto the oxide. These structures were then annealed at different temperatures for various lengths of time. Table 5.1 summarizes the layer thicknesses and annealing conditions for each sample, plus specific oxidation

Sample Name	Al Thickness (nm)	Ge Thickness (nm)	Oxidizing Time	Annealing Time (h)	Annealing Temperature (ºC)
BEG1A8 A1	100	300		1	400
BEG2A5 as grown	100	100		N/A	N/A
BEG2A5 A8	85	110		2	400
BEG2A8 A30	215-250	215-250	3 hours	4	400
BEG3A9 A1	350-620	385-560		1	400
BEG3A9 A30	300 (nominal)	100 (nominal)	10 days	4	400
BEG5A12 Quartz	60 (nominal)	40 (nominal)		19	360
SiGe8Al15	45-65	200	6 days	4	400

Table 5.1: Measured thicknesses (except where noted) of Al and Ge layers, as well as annealing and oxidizing conditions.

conditions used for three of these samples. XRD was performed to confirm the crystallization of Ge and determine crystal orientation. Cross-sectional samples were prepared for transmission electron microscopy (TEM) observation using a Nova200 focused-ion beam (FIB). Diffraction contrast and high-resolution TEM images and scanning transmission electron microscopy/energy dispersive x-ray spectroscopy (STEM EDX) line profiles were taken using an FEI-Phillips CM200 FEG TEM. High-angle annular-dark-field (HAADF) images and EDX line profiles and maps were taken with a JEOL ARM200F TEM/STEM.

5.4 Results and discussion

Figure 5.1 shows a cross-sectional TEM image of the as-grown sample and a schematic of the corresponding nominal structure. The Al and Ge layers both exhibit

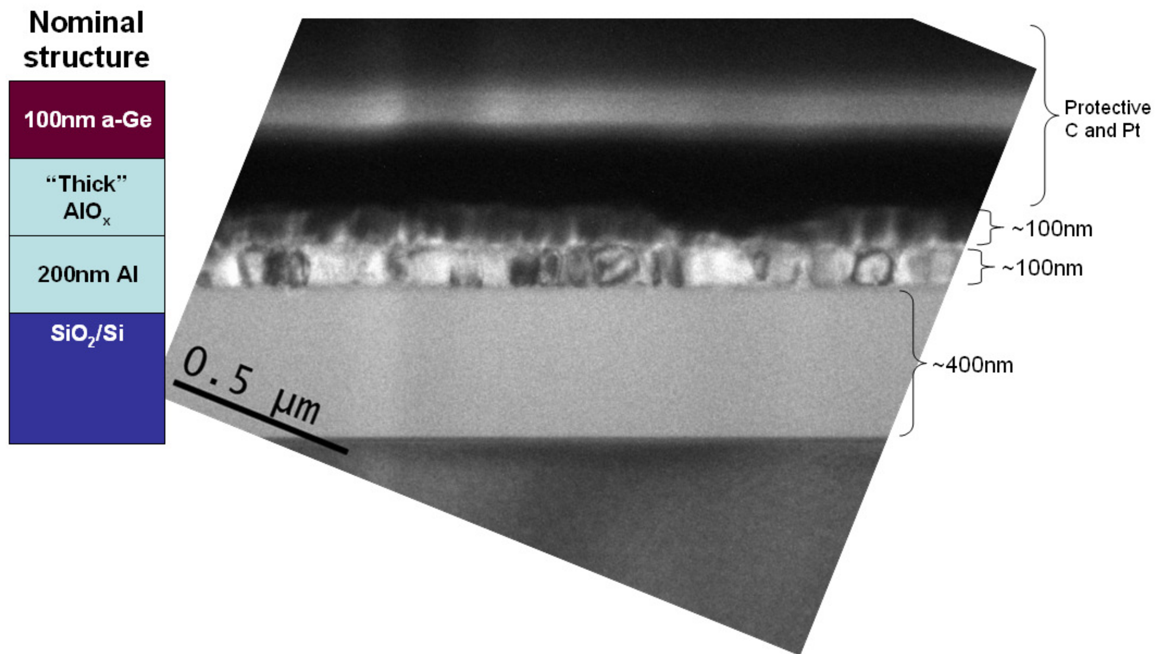

Figure 5.1: Nominal structure and TEM image of as-grown *a*-Ge/Al/SiO_2/Si sample.

columnar structures. The observed Al layer thickness is half of the nominal value, but the nominal and observed Ge layer thicknesses match. Aluminum oxide, though labeled "thick" in the nominal structure, is not visible in the image as a distinct layer. The C and Pt layers were deposited during FIB sample preparation to protect the top surface.

Figure 5.2 shows (a) and (b) TEM images, (c) STEM image, and (d) EDX line profile of the same initial structure after annealing for 2 hours at 400ºC. The *a*-Ge layer

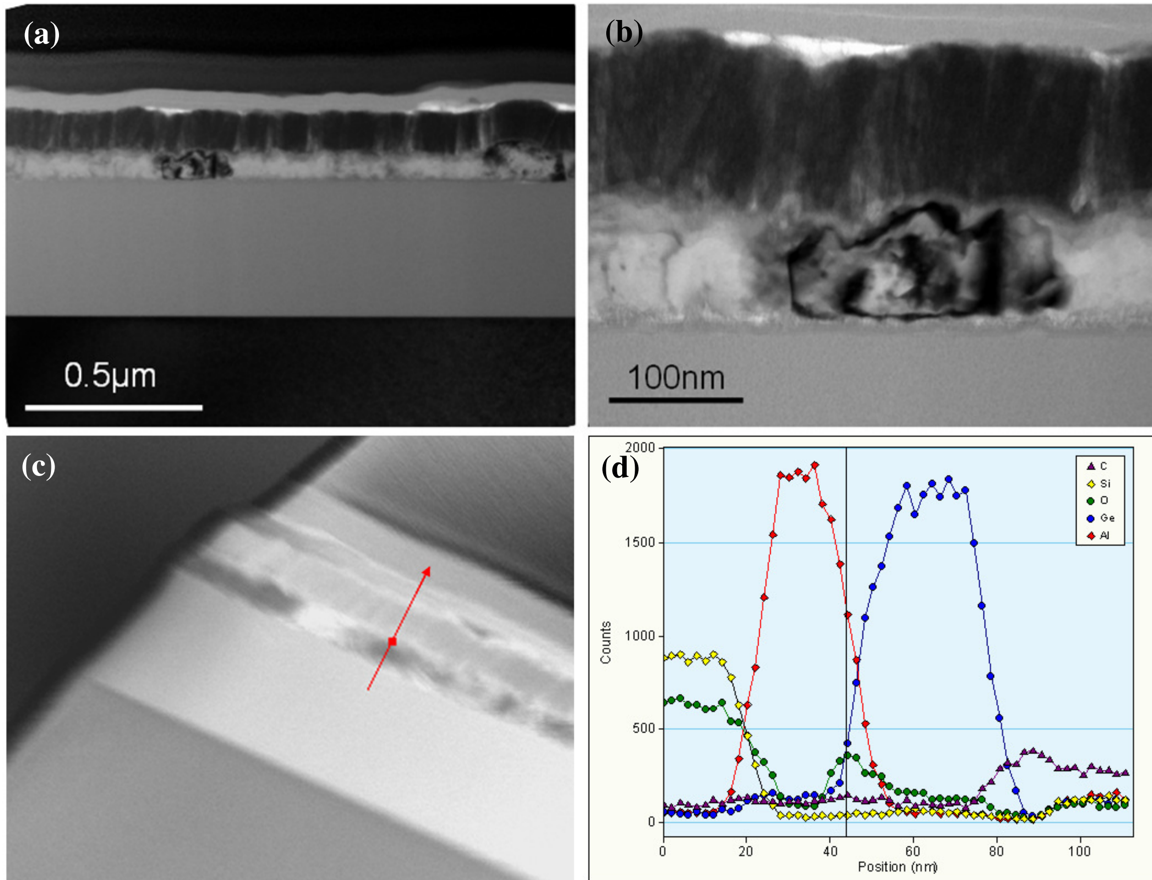

Figure 5.2: (a) and (b) TEM images of *a*-Ge/Al/SiO_2/Si sample in Figure 5.1 after annealing at 400ºC for 2 hours. (c) STEM image showing location of EDX line scan in (d). The direction of the arrow in (c) indicates the direction of the scan, and the black line in (d) marks the position of the red dot in (c).

still appears columnar, but the layer is about 10nm thicker than in the as-grown sample, and the Al layer is about 15nm less than in the as-grown sample. Neither layer appears to have crystallized any further, and layer exchange has clearly not occurred. However, there is a small increase in oxygen concentration just below the Ge layer, where the Al concentration is decreasing, indicating the presence of a thin oxide layer between the Al and Ge layers.

Some annealed samples, however, did show crystallization within the Ge layer. All three samples which had been annealed at 400ºC for 4 hours resulted in Ge crystallization, despite their different structures. In figure 5.3, both XRD (a) and HRTEM (b) of sample BEG 3A9 A30 reveal that the Ge layer is polycrystalline. Peaks corresponding to 3 different Ge spacings are present in the XRD scan, and lattice fringes in 3 different directions are also visible in the TEM image.

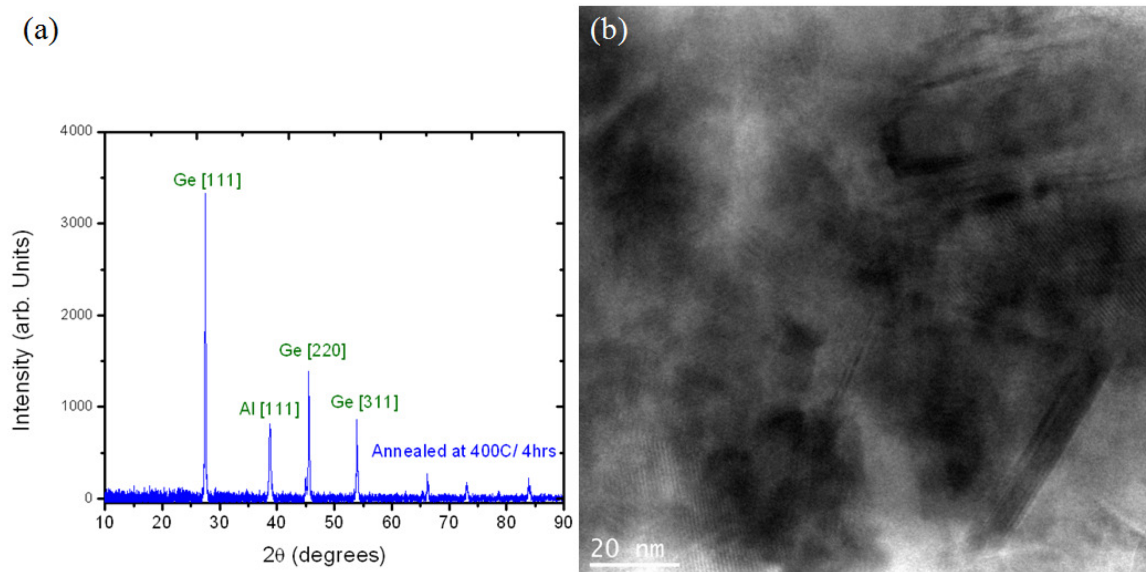

Figure 5.3: (a) XRD scan of BEG 3A9 A30, annealed at 400ºC for 4 hours, and (b) TEM image showing polycrystalline Ge layer.

These same annealing conditions (400ºC for 4 hours) also seemed to result in at least partial layer exchange in two out of the three samples. Sample BEG3A9 A30 demonstrated diffusion/ layer exchange. However, this layer exchange was not uniform across the sample. Figures 5.4(a)-(c) shows EDX line profiles from locations shown on

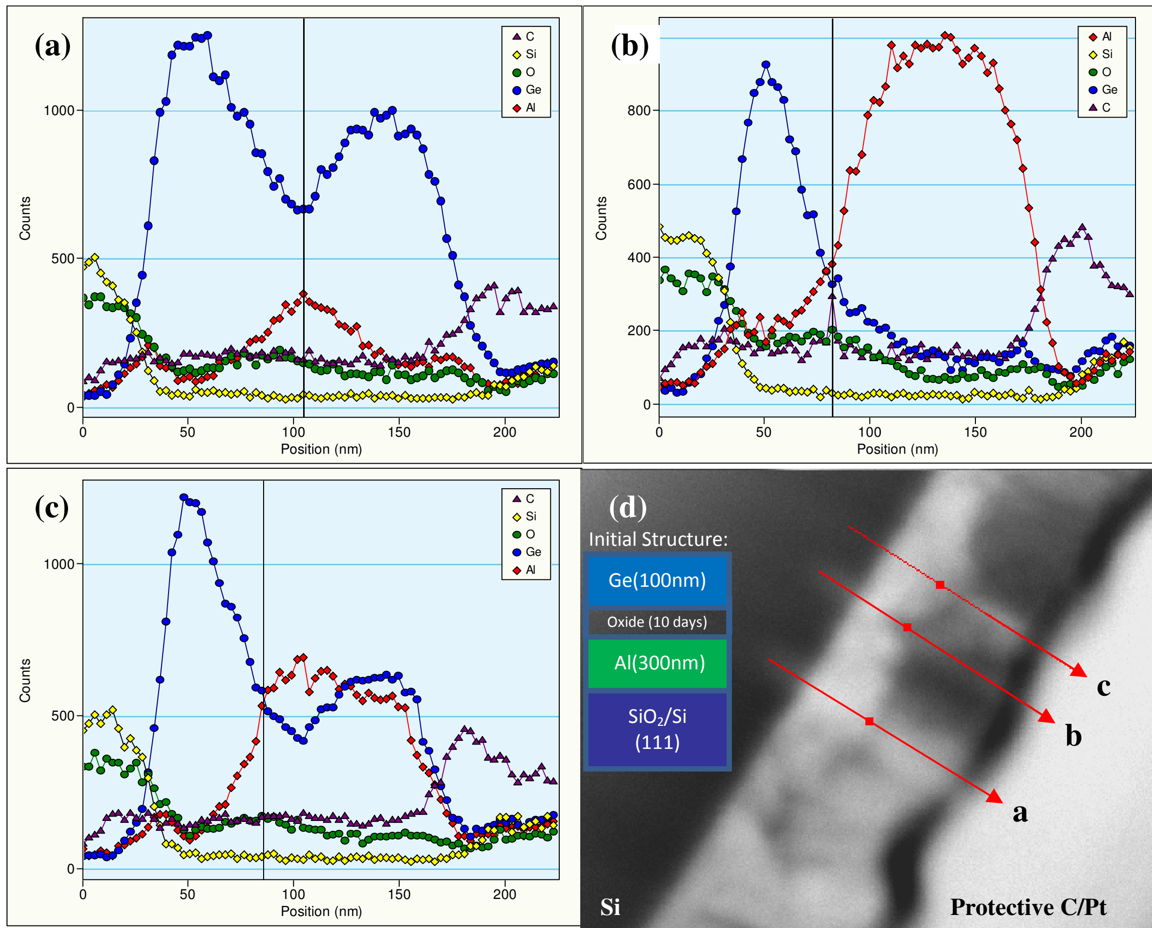

Figure 5.4: (a)-(c) EDX line profiles of sample BEG3A9 A30 taken at the locations indicated by the arrows in (d) dark-field STEM image. The arrowheads indicate the end of the scan, and the red squares on the arrows in (d) indicate the positions of the black lines in (a)-(c). The initial structure before annealing is inset in (d).

the dark field STEM image in figure 5.4(d). The arrowhead indicates the location of the end of the scan. When compared to the initial structure inset in (d), the profile in (b) shows clearly that layer exchange has occurred at this location. However, it is also clear that large compositional differences are present over a small region.

Bright-field TEM images of BEG2A8 A30, as shown in figure 5.5a, suggested that this sample may have undergone more uniform layer exchange than BEG3A9 A30. The Ge layer (Z=32) should appear darker in bright-field TEM than the Al (Z=13) layer. Thus, the image suggests that the Al layer is above the Ge layer. Comparing the image to the initial structure inset suggests that layer exchange may have occurred. However,

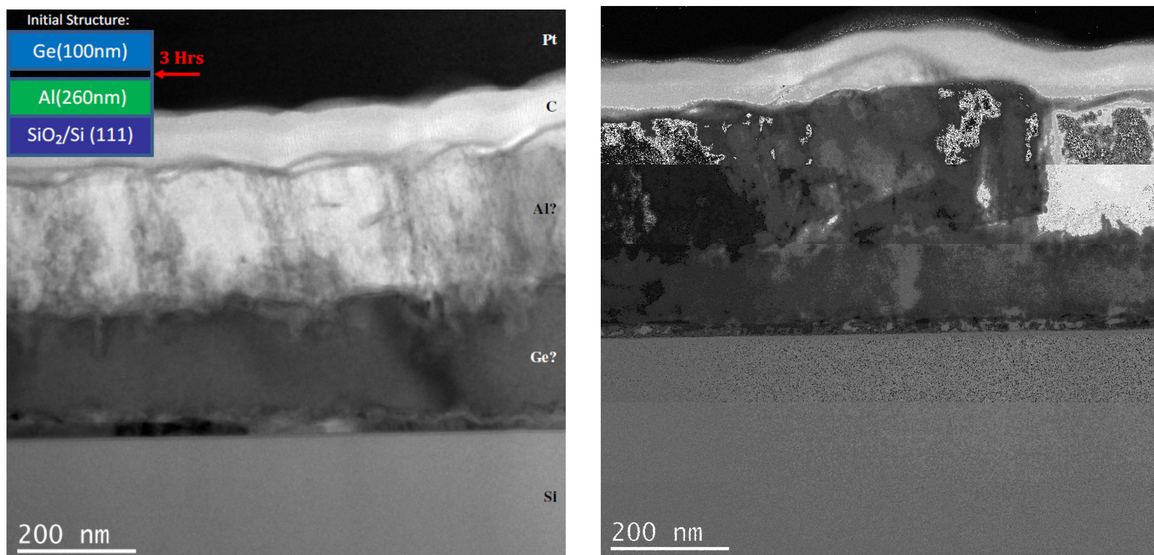

Figure 5.5: (a) XTEM image of sample BEG2A8 A30, with initial, pre-annealing structure inset. The top layers are protective carbon and platinum layers deposited during focused-ion-beam sample preparation. (b) XTEM image of the same sample in a different lateral location, where the image contrast is different from that in (a).

figure 5.5b shows a different lateral location in the sample, where the thickness in the beam direction is greater than in figure 5.5(a). The contrast has changed, which could be a result of composition or thickness.

To further investigate the composition of BEG2A8 A30, a HAADF image of a thin region of the sample is shown in figure 5.6a. HAADF is also known as Z-contrast imaging because of its strong dependence on the atomic number of the elements in the sample. Lighter contrast should correspond to a larger atomic number in dark field, so Ge

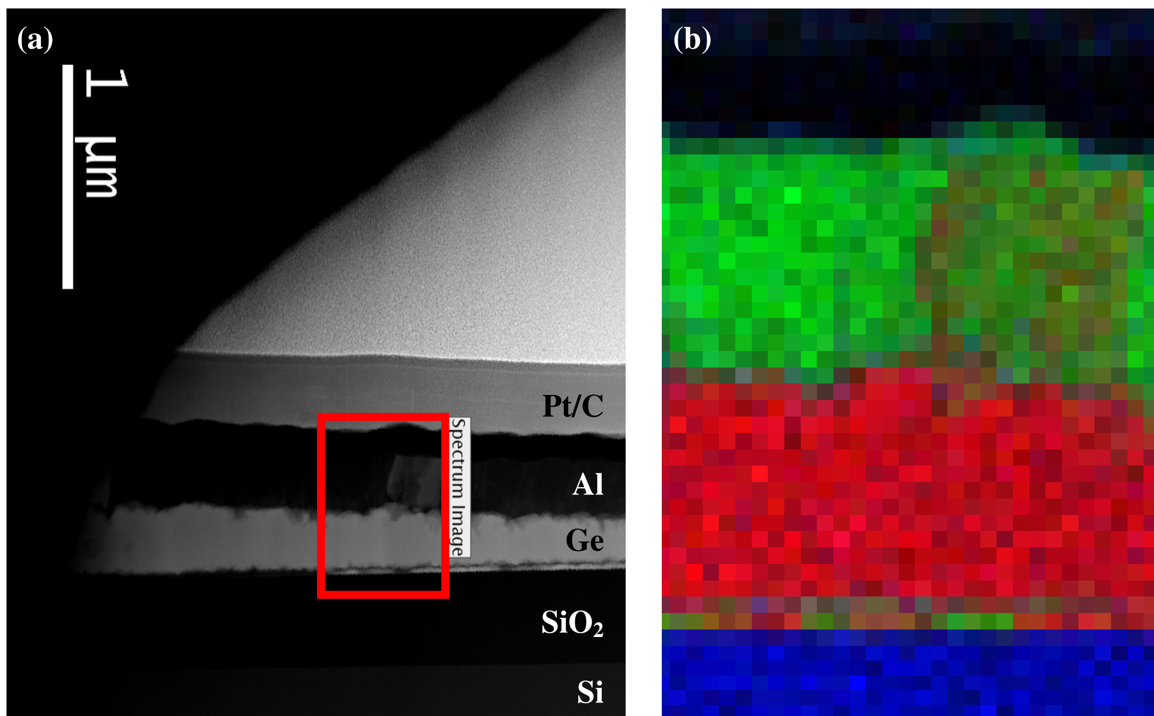

Figure 5.6: (a) HAADF image of thin region of BEG2A8 A30, indicating layer exchange, with the exception of the lighter region within the Al layer in the red box. (b) An EDX map of the region in the red box in (a). Red represents Ge, green Al, and blue O. The lighter region in the Al layer in (a) is shown by (b) to be an Al/Ge mixture.

should appear brighter in HAADF images. The lower layer is brighter and most of the upper layer is darker, confirming layer exchange. However, there is also a bright region within the Al layer, which could be an Al/Ge mixture, indicating incomplete layer exchange. The darkest layer above the Al is protective C, followed by a Pt/C mixture and finally Pt. To determine whether the brightness in this region was due to Ge or another element, an EDX map was taken of the region indicated by the red box in figure 5.6a, and the map is shown in figure 5.6b. In the EDX map, red represents Ge, green is Al, and blue is O. The lighter region in the Al layer in the HAADF image is confirmed to be an Al/Ge mixture because there is both red and green in the EDX map. This result indicates layer exchange did not proceed to completion.

Additional HAADF images of other locations in sample BEG2A8 A30 are shown in figure 5.7a and b. The Z-contrast in these images further indicates that layer exchange is incomplete in some regions of the sample. In fact, in figure 5.7b, the Ge seems to disappear from the lower layer altogether, and then possibly reappear in very small concentrations. It can also be seen that the thickness of the Ge layer is not constant.

The two samples that experienced layer exchange had the same annealing conditions (4hrs at 400ºC), but SiGe8Al15 also shared these conditions without showing layer exchange. One difference between these samples is oxidation time. However, the samples with layer exchange were left in air for 3 hours and 10 days, respectively, while the sample that did not exhibit layer exchange was left in air 6 days. Thus, it cannot be concluded that shorter or longer oxidation time leads to layer exchange. If oxidation time does not play a role in layer exchange, then this points to layer thicknesses as a possible contributing factor. It is difficult to make this conclusion definitively, however, because it

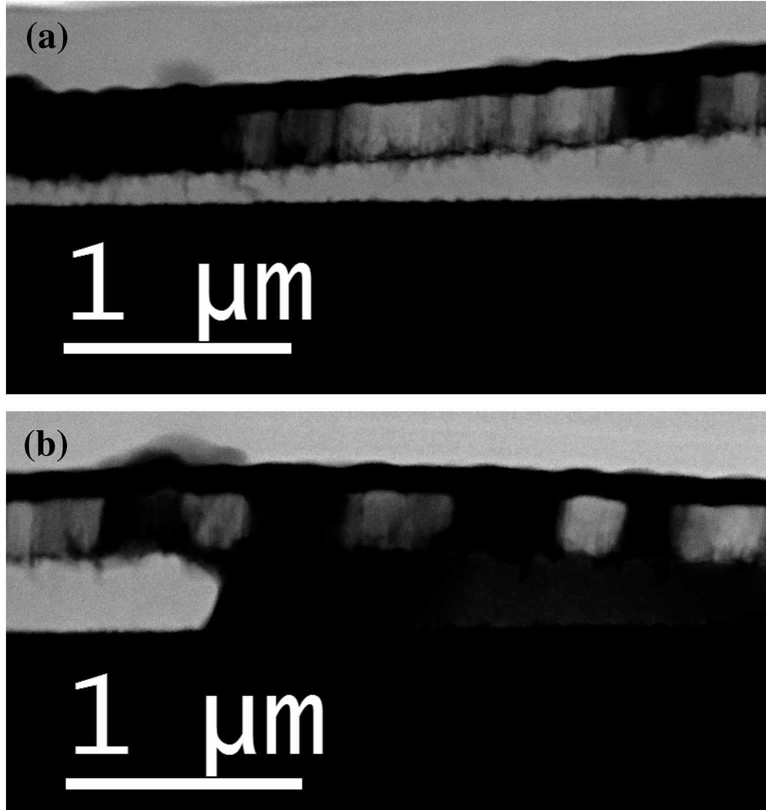

Figure 5.7: (a) and (b) HAADF images of sample BEG2A8 A30. The Z-contrast indicates that layer exchange is incomplete in some regions.

is difficult to determine the layer thicknesses of sample BEG3A9 A30. After annealing, TEM showed that BEG3A9 A30 did not have well-defined layers, which requires relying on the nominal thicknesses. Unfortunately, the nominal layer thicknesses differed significantly from the measured thicknesses in all samples, so that it is not possible to state precisely from the results for these samples what factors lead to Al/Ge layer exchange.

Table 5.2 summarizes the TEM and EDX results of Ge crystallization and layer exchange of each sample studied.

Sample Name	Ge Crystallization	Layer Exchange
BEG1A8 A1	N (DP)	N
BEG2A5 as grown	N	N
BEG2A5 A8	N	N
BEG2A8 A30	Y	Some
BEG3A9 A1	N	N
BEG3A9 A30	Y	Some
BEG5A12 Quartz	N?	N
SiGe8Al15	Y?	N

Table 5.2: Ge layer crystallization as observed by TEM and layer exchange as observed by EDX.

5.5 Conclusions

Two samples annealed at 400°C for 4 hours exhibited partial Ge crystallization and partial layer exchange. A third sample annealed under the same conditions may have experienced Ge crystallization but did not show layer exchange. Ultimately, since no reliable path to MIC or layer exchange was established, no definitive conclusions could be made about the mechanism of either process.

References

1. McCluskey, M.D. and Haller, E.E. 2012. *Dopants and Defects in Semiconductors*. Boca Raton: CRC Press.

2. Bosi, M. and Attolini, G. 2010. *Progress in Crystal Growth and Characterization of Materials* **56**: 146.

3. Slaoui, A., Pathi, P. and Tuzun, Ö. 2015. "Aluminum-Induced Crystallization: Applications in Photovoltaic Technologies" in Wang, Z. et al., Eds. *Metal-Induced Crystallization: Fundamentals and Applications*. Singapore: Pan Stanford Publishing.

4. Nishida, T., Mmoto, K., Saitoh, N., Yoshizawa, N., Suemasu, T., and Toko, K. 2019. *Applied Physics Letters* **114**: 142103.

5. McAlister, A.J. and Murray, J.L. 1984. *Bulletin of Alloy Phase Diagrams* **5**: 341.

6. He, D., Wang, J.Y., and Mittemeijer, E.J. 2006. *Scripta Materialia* **54**: 559.

7. Wang, J.Y., He, D., Zhao, Y.H., and Mittemeijer, E.J. 2006. *Applied Physics Letters* **88**: 061910.

8. Wang, Z.M., Wang, J.Y., Jeurgens, L.P.H., and Mittemeijer, E.J. 2006. *Scripta Materialia* **55**: 987.

9. Sain, T., Singh, C.K., Ilango, S., and Mathews, T. 2019. *Journal of Applied Physics* **126**: 125303.

CHAPTER 6

InAs QUANTUM DOTS FOR INTERMEDIATE BAND SOLAR CELLS

This chapter describes structural characterization of multiple stacks of InAs quantum dots with GaAsSb spacer layers which were being investigated for possible solar-cell applications. The work was carried out in collaboration with Yeongho Kim and Keun-Yong Ban in the group of Professor Christiana Honsberg at Arizona State University, who performed sample growth as well as carrying out photoluminescence (PL) and x-ray diffraction (XRD) measurements. The major results of this study have been published.[1]

6.1 Introduction

Lattice mismatch at an interface between two crystalline materials produces strain, which is the underlying cause of many types of structural defects.[2] Since high defect density can adversely impact device performance, an important goal for growth of high quality material is to reduce the amount of strain. In some cases, however, strain is desirable. For example, piezoelectric polarization resulting from either compressive or tensile in-plane strain can produce a two-dimensional electron gas, which is an interfacial reservoir of charge that leads to high mobility without the need for doping.[3] Another intentional usage of lattice strain is in the formation of quantum dots (QDs). These pseudomorphic nanostructures often form as a result of strain at interfaces between two lattice-mismatched materials. The interfacial free energy is minimized either as a kinetic (non-equilibrium) process during crystal growth or as a thermodynamic (equilibrium) process occurring apart from growth.[4]

Semiconductor quantum dots are finding a wide variety of useful applications. One possibility attracting increased attention is to produce an intermediate-band solar cell (IBSC).[5] The primary function of the IBSC is to collect additional photons, with energies that are less than the band gap, which would otherwise pass through the cell. As illustrated in figure 6.1, the band structure of an IBSC consists of the usual valence and conduction bands, but it also contains an additional intermediate band. This band is partially filled so that photons with energy $E_H=E_{IB}-E_V$, as depicted by photon (1) in figure 6.1, can excite electrons from the valence band to the intermediate band, and photons with energy $E_L=E_C-E_{IB}$, as depicted by photon (2), can excite electrons from the intermediate band to the conduction band. The normal valence band to conduction band transition also occurs, utilizing photons of the band-gap energy E_G, as depicted by photon (3).[5] Quantum dots confine electrons in a similar way as particles in a box[5] because the size of the dot is smaller than the de Broglie electron wavelength,[6] and the intermediate

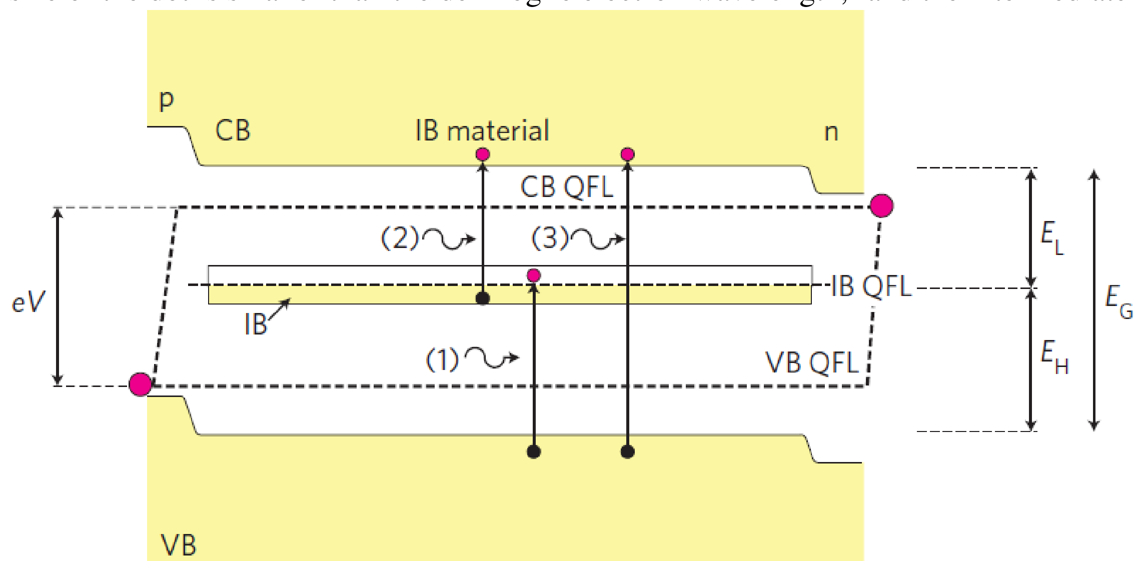

Figure 6.1: Energy diagram of an IBSC, with possible electronic transitions labeled by (1), (2), and (3).[5]

band can be thought of as the (1,1,1) ground state of the electron as a 3D particle in a box.[5] The additional electronic transitions result in increased photon absorption, which in turn offers the possibility of increased solar-cell efficiency. The maximum theoretical efficiency of an IBSC, using the Schockley-Queisser approach, was calculated to be 63%.[7] A total band-gap energy of 1.93eV, and a valence-band-to-intermediate-band energy of approximately 0.7eV, the latter corresponding to transition 1 in figure 6.1, are predicted to produce the maximum efficiency.[7] In order to optimize device performance, materials and structures should be chosen to match these energy-transition values as closely as possible.

Although the concept of an intermediate band was initially proposed in 1960,[8] and solar-cell technology research has sought to take advantage for more than a decade,[9,10] the potential of this higher efficiency approach has yet to be fully realized. As researchers strive to overcome various obstacles in realizing this potential, the TEM represents a powerful tool for direct structural imaging of possible IBSC combinations, as well as providing related chemical analysis on the nanometer and even atomic scale.

In order to increase overall collection efficiency, multiple layers of QDs could be grown above one another.[11] However, in the case of $GaAs_xSb_{1-x}/InAs$ QDs, it was previously determined that an increasing number of layers, in conjunction with increasing Sb concentration, led to higher defect densities.[11] The origin of the defects was unclear but might have been due to changes in QD morphology. TEM observations revealed triangular-shaped QDs in the first layer, but the QDs exhibited more elongated structures in successive layers. However, these samples were only grown with 10-nm spacer

layers.[11] It is possible that different spacer-layer thicknesses might lead to more uniform QD morphology and possibly lower defect densities.

6.2 Experimental Details

In these experiments, ten layers of $GaAs_{0.83}Sb_{0.17}$/InAs QDs with GaAsSb layer thicknesses (d_s) of 2, 5, 10, and 15nm were grown by solid-source molecular beam epitaxy (MBE) on n-type GaAs (001) substrates with a 400-nm GaAs buffer layer and 50-nm GaAs capping layer, as shown in figure 6.2. A nominal 2 monolayers of InAs were deposited on the spacer layers at 500ºC, resulting in the growth of InAs QDs via the Stranski-Krastanov mode.[1]

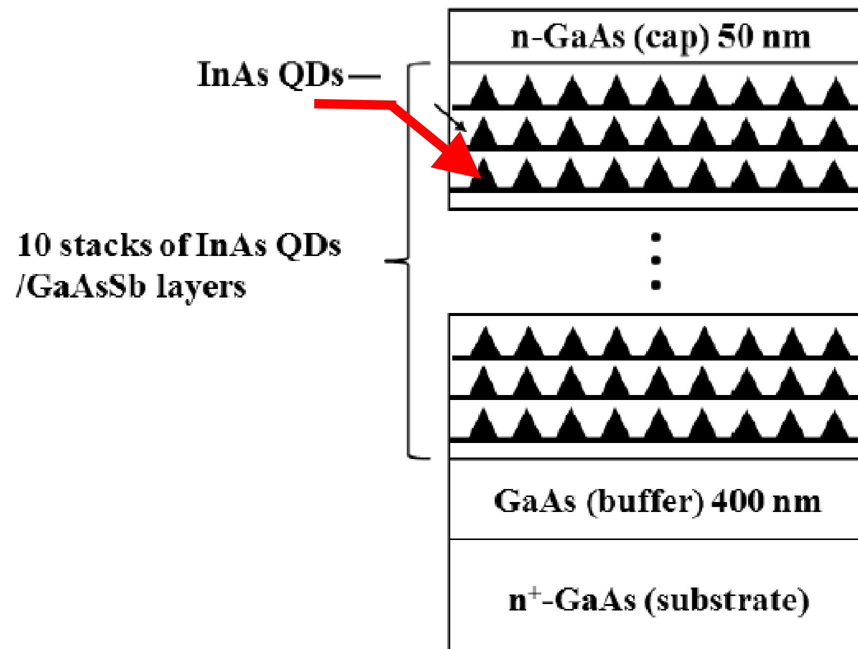

Figure 6.2: Structure of samples, with varying thicknesses of $GaAs_{0.83}Sb_{0.17}$ spacer layers.

An X'Pert MRD diffractometer was used to perform XRD measurements. Photoluminescence measurements were performed in a closed-cycle He cryostat using a semiconductor laser with a wavelength of 405nm to excite the samples and a liquid nitrogen-cooled Ge detector and lock-in amplifier to process the signals. Diffraction contrast and high-resolution TEM images were obtained using an FEI-Phillips CM200 FEG TEM operated at 200keV and a JEOL JEM-4000 EX TEM operated at 400keV.

6.3 Results and Discussion

Figure 6.3 shows triple-crystal (TC) *ω* rocking curves (RCs) taken around the (004) symmetrical reflections of the GaAs capping layers and the GaAsSb spacer layers. The full-width-at-half-maximum (FWHM) of the RCs for GaAs gradually increase as d_s is increased from 2nm to 10nm, but show a dramatic increase for 15nm. This observation suggests that the crystal quality of the *capping* layer of the sample with 2-nm spacer

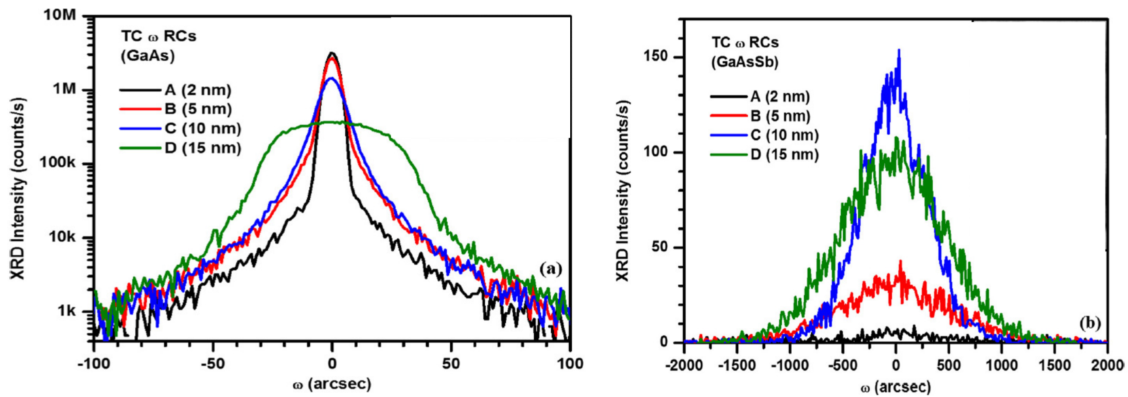

Figure 6.3: XRD TC ω RCs for: (a) GaAs capping layers, and (b) GaAsSb spacer layers of $GaAs_{0.83}Sb_{0.17}$/InAs QD samples.[1] The FWHMs of RCs of the capping layers in (a) show small increases from 2-nm to 5-nm to 10-nm spacer layers, and a dramatic increase for the 15-nm spacer layer. The FWHM of the RC of the 10-nm spacer layer is the smallest in (b).

layers is greatest, with 5nm and 10nm not far behind, while that of the sample with 15-nm layer spacing is considerably worse. The FWHM of the RCs for the *spacer* layers is smallest for 10-nm layers, indicating highest overall quality in that sample.

Plan-view TEM images of the samples with spacer layer thicknesses of 2nm and 15nm are shown in figures 6.4 (a) and (b), respectively. While the termination of some threading dislocations are visible in the image of the sample with 2-nm spacer layers, the surface of the sample with 15-nm spacer layers shows a dense cross-hatched pattern, which is interpreted as corresponding to an array of in-plane edge dislocations. From figure 6.4(a), the defect density of the sample with the 2-nm spacer layers was calculated to be on the order of 10^{10}cm^{-2}. These observations support the conclusion that the quality of the sample with spacer layers of 15nm is significantly worse than that of the sample with spacer layers of 2nm.

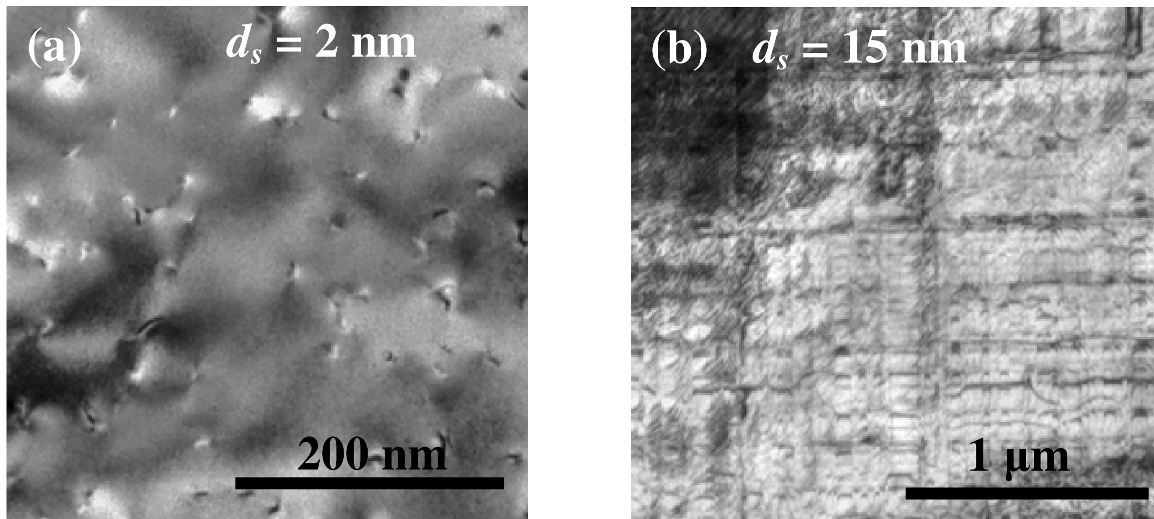

Figure 6.4: Plan-view TEM images of $GaAs_{0.83}Sb_{0.17}$/InAs QD samples with spacer layer thicknesses of: (a) 2nm, and (b) 15nm.

Cross-sectional TEM images of the samples with 5- and 10-nm spacer layer thicknesses are shown in figures 6.5 (a) and (b), respectively. The undulation of the layers is demonstrably less in the sample with 10-nm spacer layers than with 5-nm spacer layers, which also supports the XRD results which showed that the 10-nm spacer layer had the highest growth quality, most likely due to optimal balance of the strain in the GaAsSb layers, which originates from compressive strain from the GaAs substrate and from tensile strain from the InAs wetting layers.

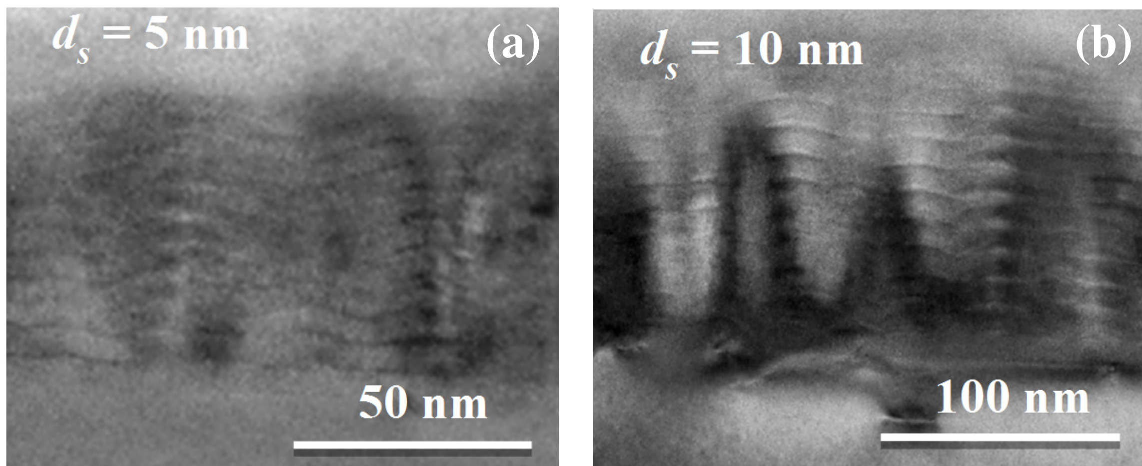

Figure 6.5: XTEM images of $GaAs_{0.83}Sb_{0.17}$/InAs QD samples with spacer layers: (a) 5nm and (b) 10nm.

Figure 6.6 compares the temperature dependence of photoluminescence (PL) spectra from the four samples.[1] The PL intensities remain effectively constant below 60K, and then show a steady falloff as the temperature is further increased, presumably as a result of enhanced thermal escape of the carriers into the InAs wetting layers and the GaAsSb/GaAs barriers. The significant point here, however, is the clearly superior performance of the 10-nm stack over the entire temperature range, which is consistent with the microstructural details visible in the cross-sectional electron micrographs.

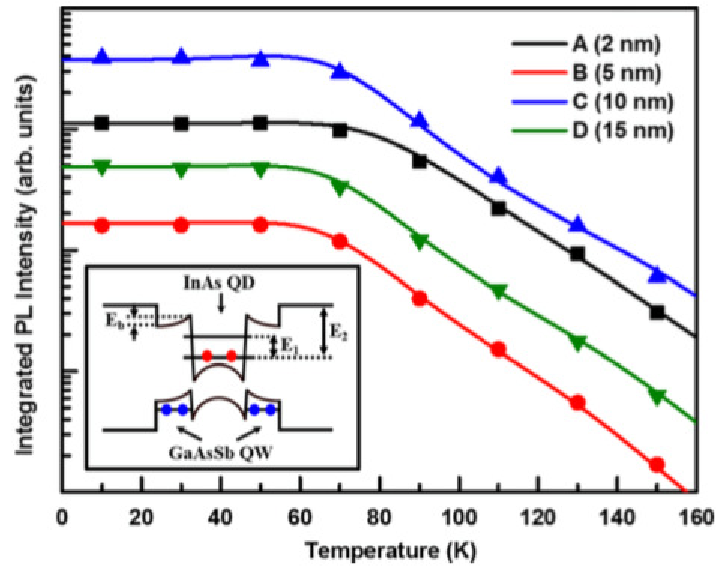

Figure 6.6: Integrated PL intensities vs. temperature for multi-stack QD samples.[1] Inset illustrates schematic band diagram for Type-II InAs/GaAsSb QD structure.

6.4 Conclusions

Potential IBSC materials consisting of multilayered $GaAs_{0.83}Sb_{0.17}$/InAs QD samples with spacer-layer thicknesses of 2nm, 5nm, 10nm, and 15nm were investigated using XRD and TEM. A 10-nm GaAsSb layer thickness resulted in the highest crystal quality. The quality of the capping layer also depended on the spacer layer thickness, increasing slightly from 2nm to 10nm, but decreased dramatically from 10nm to 15nm. Taking both the spacer layer quality and capping layer quality into account indicates that a GaAsSb spacer-layer thickness of 10nm would be preferable over that of 2nm, 5nm, and 15nm when growing arrays of InAs QDs for solar-cell device purposes. These structural results were in good agreement with the corresponding optical properties of the same set of samples.

References

1. Kim, Y., Ban, K.-Y., Boley, A., Smith, D.J., and Honsberg, C.B. 2015. *Applied Physics Letters* **107**: 173109.

2. McCluskey, M.D. and Haller, E.E. 2012. *Dopants and Defects in Semiconductors*. Boca Raton: CRC Press.

3. Smith, D.J., Cullen, D.A., Zhou, L., and McCartney, M.R. 2010. *Microelectronics Reliability* **50**: 1514.

4. Ledentsov, N.N., Ustinov, V.M., Shchukin, V.A., Kop'ev, P.S., Alferov, Z.I., and Bimberg, D. 1998. *Semiconductors* **32**: 343.

5. Luque, A., Martí, A., and Stanley, C. 2012. *Nature Photonics* **6**, 146.

6. Nozik, A.J. 2002. *Physica E* **14**, 115.

7. Luque, A. and Martí, A. 1997. *Physical Review Letters* **78**, 5014.

8. Wolf, M. 1960. *Proceedings of the IRE* **48**, 1246.

9. Luque, A., Martí, A., Stanley, C., Lopez, N., Cuadra, L., Zhou, D., Pearson, J.L., and McKee, A. 2004. *Journal of Applied Physics* **96**, 903.

10. Wahnón, P. and Tablero, C. 2002. *Physical Review B* **65**, 155115.

11. Tang, D. 2014. *Characterization of MBE-grown Semiconductor Materials for Photovoltaic Applications* [Thesis]. Arizona State University.

CHAPTER 7

INVESTIGATION OF PLASMA-ASSISTED Si SURFACE PASSIVATION

This chapter describes an investigation of plasma-treated amorphous/crystalline Si interfaces, with and without oxide capping layers. The work was carried out in collaboration with Jianwei Shi in the group of Professor Zachary Holman at Arizona State University, who performed the sample growth and lifetime measurements.

7.1 Introduction

Dangling bonds at the surfaces of crystalline materials can act as recombination centers.[1] The two primary methods that are used to passivate these dangling bonds are: (1) field-effect passivation, in which an electric field at the surface repels charges; and (2) deposition of a thin layer which forms chemical bonds with the surface atoms so that the original dangling bonds no longer exist.[2] In the case of Si-based solar cells, an *a*-Si layer is commonly used to chemically passivate the *c*-Si surface.[1] However, in order to avoid epitaxial growth above the original *c*-Si surface, the *a*-Si layer must be grown at low temperature with additional non-ideal parameters.[2] This difficulty is compounded by the necessity for a series of thin *a*-Si layers (total thickness of ~15-20nm) for photovoltaic applications.[3]

Hydrogen plasma treatment (HPT) after deposition of the amorphous layers can improve the *a*-Si passivation and minority carrier lifetimes by improving hydrogen diffusion to the *a*-Si/*c*-Si interface[2,4,5] and approaching the amorphous-to-crystalline transition.[3,4] The hydrogen in-diffusion caused by HPT changes the type of Si-H bonding in the *a*-Si layer without increasing strain between Si atoms.[2] Specifically, disorder

within the *a*-Si layer is increased due to the formation of voids[2,4,6] and shift in composition from primarily SiH to SiH_2.[4] Despite the presence of vacancies, the disorder and increased hydrogen content are associated with higher material quality close to an amorphous-to-crystalline transition.[4] In addition, because the strain remains unchanged, HPT should not affect the sample stability.[2] The H_2 flow rate used during HPT is a balance between competing concerns – high enough to increase the hydrogen content in the *a*-Si:H layer, but not sufficient to generate mobility of surface atoms so that they locate more stable bonding sites and thus increase the order of the layer.[7]

Hydrogen plasma treatments have been shown to produce a greater percentage improvement for minority carrier lifetimes within *a*-Si/*c*-Si(111) than *a*-Si/*c*-Si(100), but the effect is still observed in both substrate orientations.[4] After HPT, minority carriers within Si solar cell structures have reached lifetimes of ~6-8ms.[3,4] A combination of HPT followed by one minute of annealing further increased lifetimes up to approximately 11ms,[2,4] although additional annealing had little effect.[4] HPT has also been shown to increase the band-gap energy of the *a*-Si layer by lowering the valence band minimum, thereby reducing parasitic absorption and creating opportunities for band-gap engineering.[2,4,6]

One of the major drawbacks of HPT is etching of the *a*-Si surface.[6,8] If too much amorphous material is etched, then defects are introduced into the underlying crystalline material, and the amount of *c*-Si surface roughness is increased.[6] This damage to the crystalline layer can reduce minority carrier lifetime within the material,[9] and consequently negatively impact the solar-cell performance. This current study involves

the characterization of several *a*-Si/*c*-Si(100) samples subjected to H_2 plasma treatments for the purpose of optimizing minority carrier lifetimes.

7.2 Experimental details

The samples that were studied were prepared as follows: A nominally 8-12nm layer of *a*-Si was grown on *c*-Si(100) using PECVD at 250°C, and some samples were then capped with a layer of SiO_x. Samples underwent H_2 plasma treatments at 60W for varying lengths of time, and carrier lifetimes were then measured. The results are shown plotted in figure 7.1.

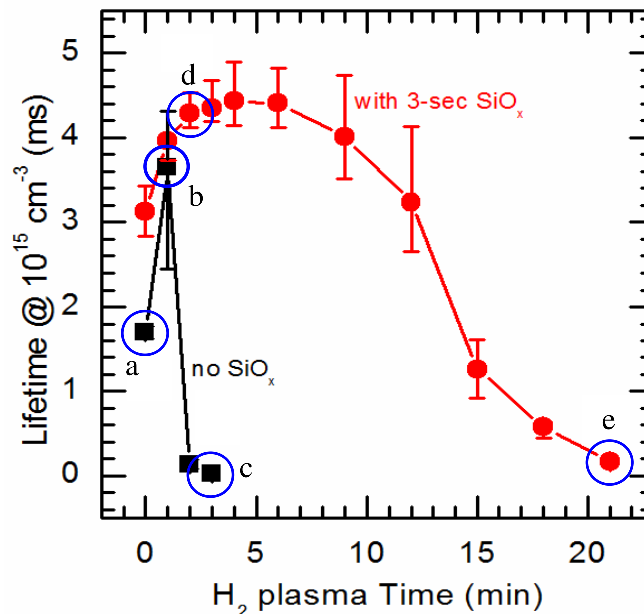

Figure 7.1: Carrier lifetimes of plasma-treated *a*-Si/*c*-Si samples. The solid red circles represent samples with a SiO_x capping layer, and the solid black squares represent samples with no capping layer. Samples a-e circled in blue were examined by TEM.

It was anticipated that samples with short lifetimes would have defects in the crystalline layer associated with the plasma treatment. Thus, five samples, which are circled in blue and labeled a-e in figure 7.1, were selected for cross-sectional TEM observation. These were prepared first by FIB milling (FEI Nova 200) and then using plasma trimming, a technique where the plasma both removes material sputtered on the sample surface by the FIB, and also further thins the sample. The samples labeled a and c-e were subsequently examined by XTEM using an FEI-Phillips CM200 FEG TEM operated at 200kV, and Sample b was examined using an aberration-corrected FEI Titan 80-300 operated at 300kV.

7.3 Results and discussion

Figure 7.2 compares diffraction-contrast XTEM images of the *a*-Si/*c*-Si interfaces of Samples a and c-e. A thin (~4nm) layer at the top of the *c*-Si is visible in all samples. Samples had not been chemically etched prior to HPT, which suggests that this layer is most likely a native oxide because the samples were exposed to air before the *a*-Si deposition took place. All four samples, even the untreated Sample a, exhibit uneven *c*-Si surfaces. Samples a and c appear visually to have greater surface roughness than the other two. However, when carefully measured, the surface roughness of all samples was ≤ 2nm and seemed roughly equivalent.

The surface roughness of each sample was determined from high-magnification images, by measuring the distance between the highest point of the crystalline lattice-fringes to the lowest within a single image (~40nm lateral distance), and averaging across 3-4 images for each sample. Figure 7.3 shows three such measurements of the untreated

Sample a. These images reveal that the amount of surface roughness varied locally, which was an effect observed in all samples. This variation explains why some of the samples shown in figure 7.2 might appear to have greater roughness than others when in fact they are measured to be almost the same.

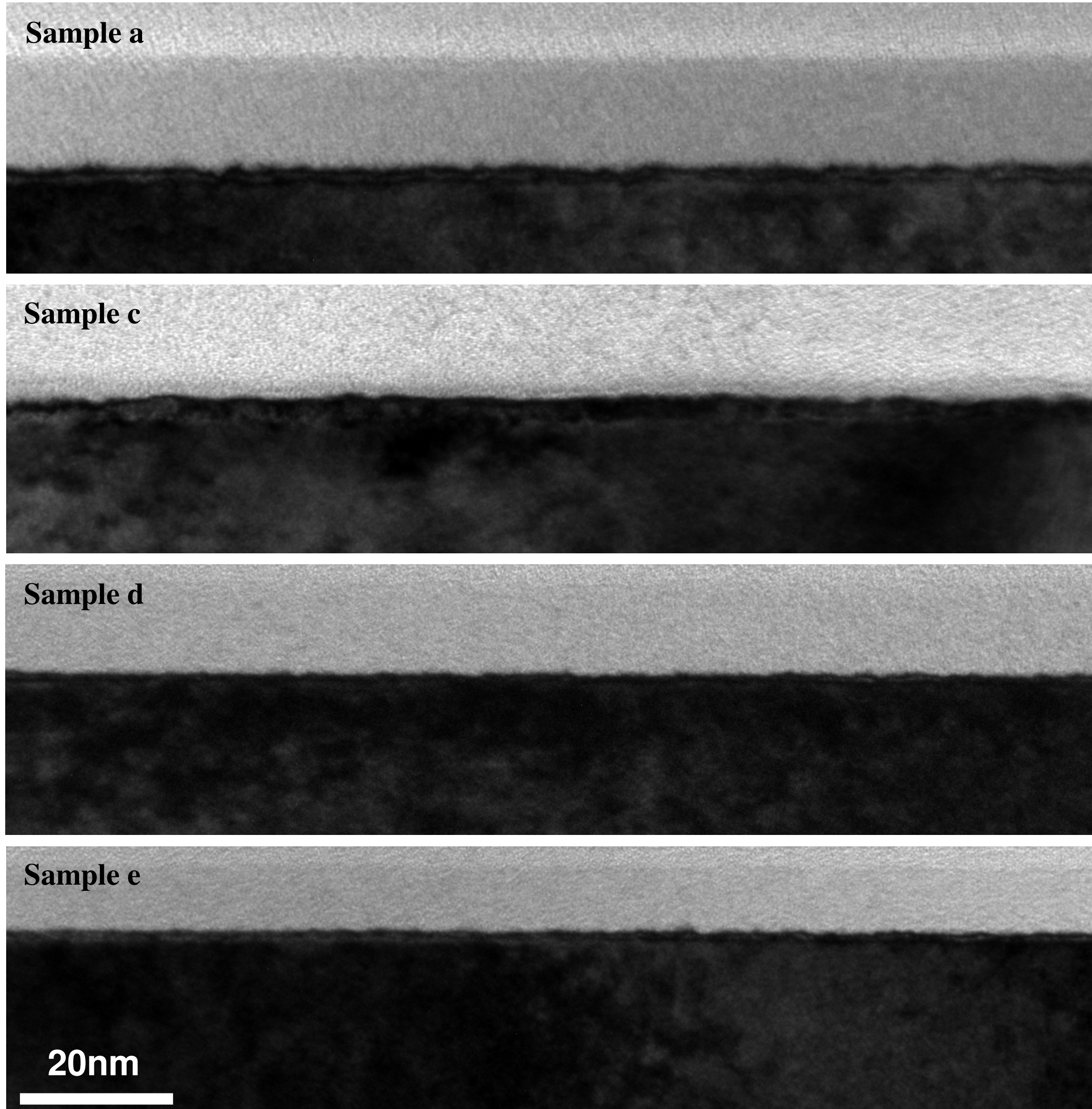

Figure 7.2: Diffraction-contrast TEM micrographs of Samples a and c-e. Samples d and e were grown with an SiO_x capping layer, and Samples a and c were not. A thin layer can

be distinguished above the *c*-Si surface before the *a*-Si layer. The *c*-Si surface of each sample is uneven, and the local regions imaged in this figure show greater surface roughness in Samples a and c relative to Samples d and e.

Figure 7.4 shows high-magnification TEM images of Samples a-e. All samples show high crystalline quality, and no visible crystal defects. The images in figure 7.4 also show the surface roughness, even in the untreated sample. If the surface morphology were a direct result of plasma treatment, then the untreated sample should look different. Since the surfaces of all the samples seem equally uneven, this feature is also likely due to a lack of chemical etching prior to deposition. Figures 7.2-7.4 would indicate that the differences in lifetime of these samples are not associated either with etching or with introduction of defects in the crystalline layer.

Figure 7.5 shows high-magnification images of the amorphous layer of Samples a, c and e. Because of the difference in atomic number, the difference in image contrast reveals the interface between the *a*-Si layer and the protective carbon layer that was deposited during TEM sample preparation. This interface was discernable in all samples except Sample b. As shown in figure 7.5, the thickness of the amorphous layer in Sample c, approximately 4nm, is considerably less than in the other samples. It has been reported that a minimum thickness of the amorphous layer (~8nm for a hydrogen plasma RF power of 100mW) is necessary to prevent a sharp decline in minority carrier lifetime, an observation which was attributed to etching of the crystalline surface.[6] However, the crystalline surface in Sample c does not appear to be etched. It is possible the lifetime reduction lifetime for Sample c may be correlated with the thinner amorphous layer, but

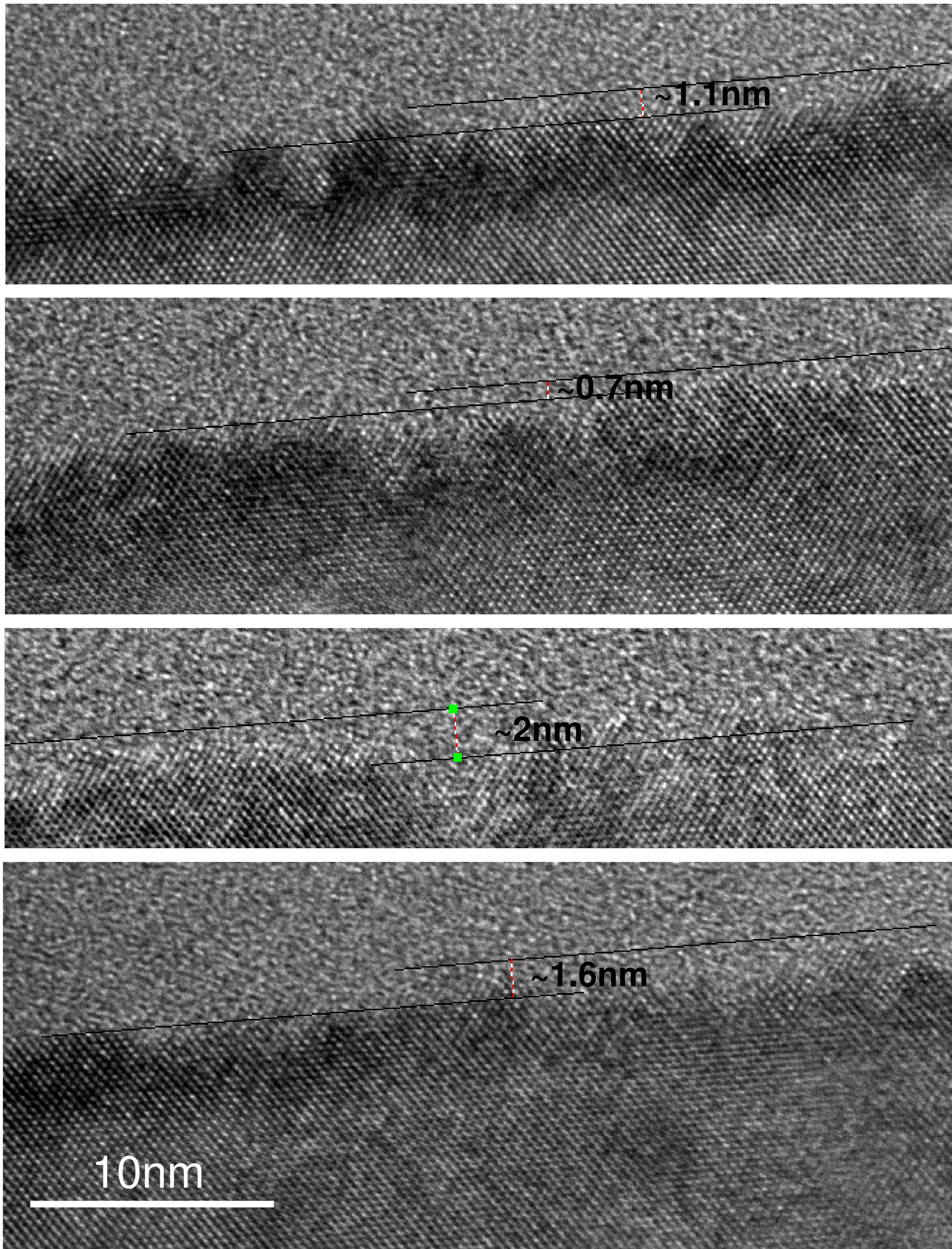

Figure 7.3: High-magnification images of Sample a, the untreated sample, illustrating local variability in surface roughness.

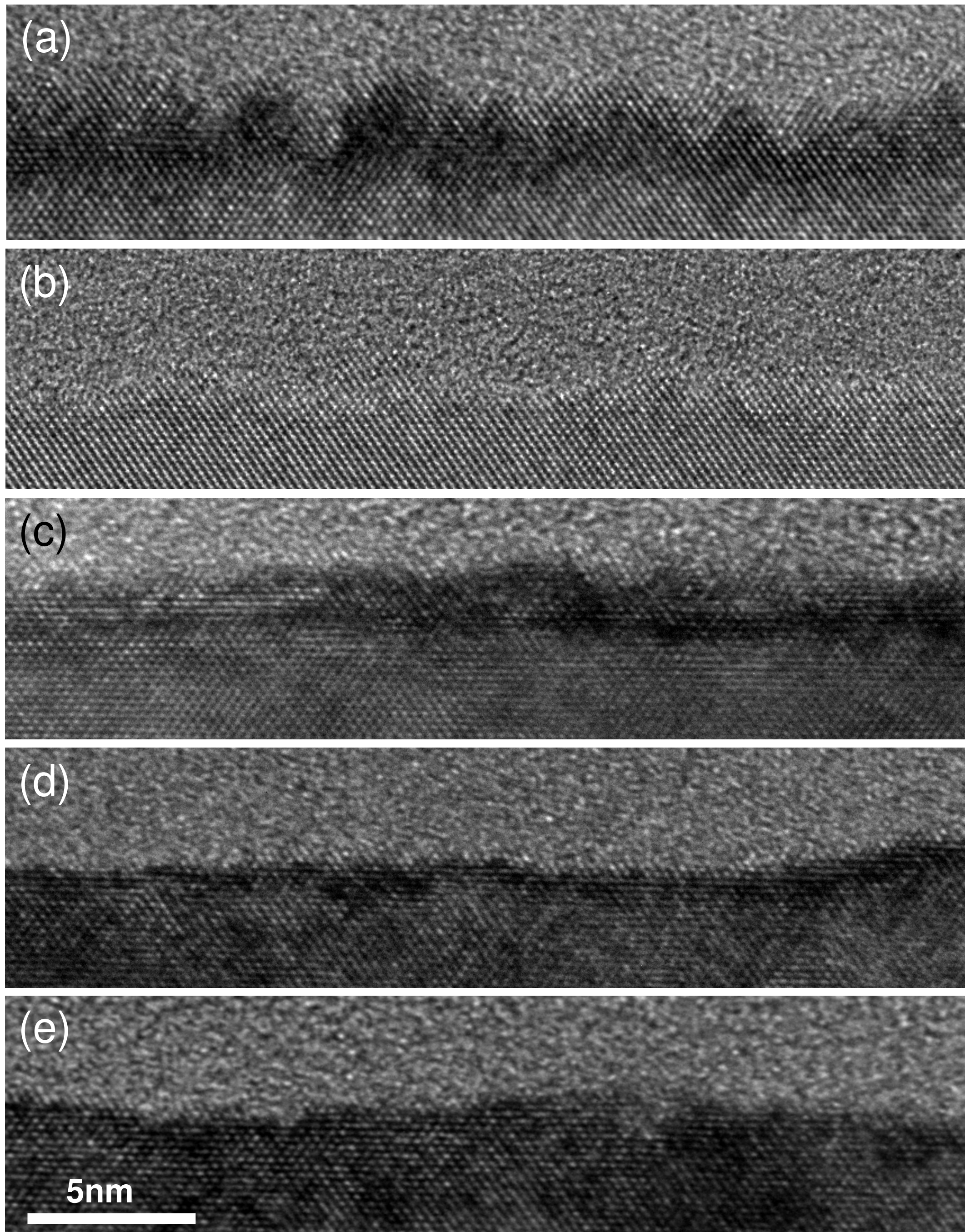

Figure 7.4: High resolution XTEM images of *a*-Si/*c*-Si interface for Samples a-e. The *c*-Si surface in each sample is uneven but without visible defects, indicating no significant differences between the crystalline layers that might possibly correlate with the observed differences in carrier lifetimes.

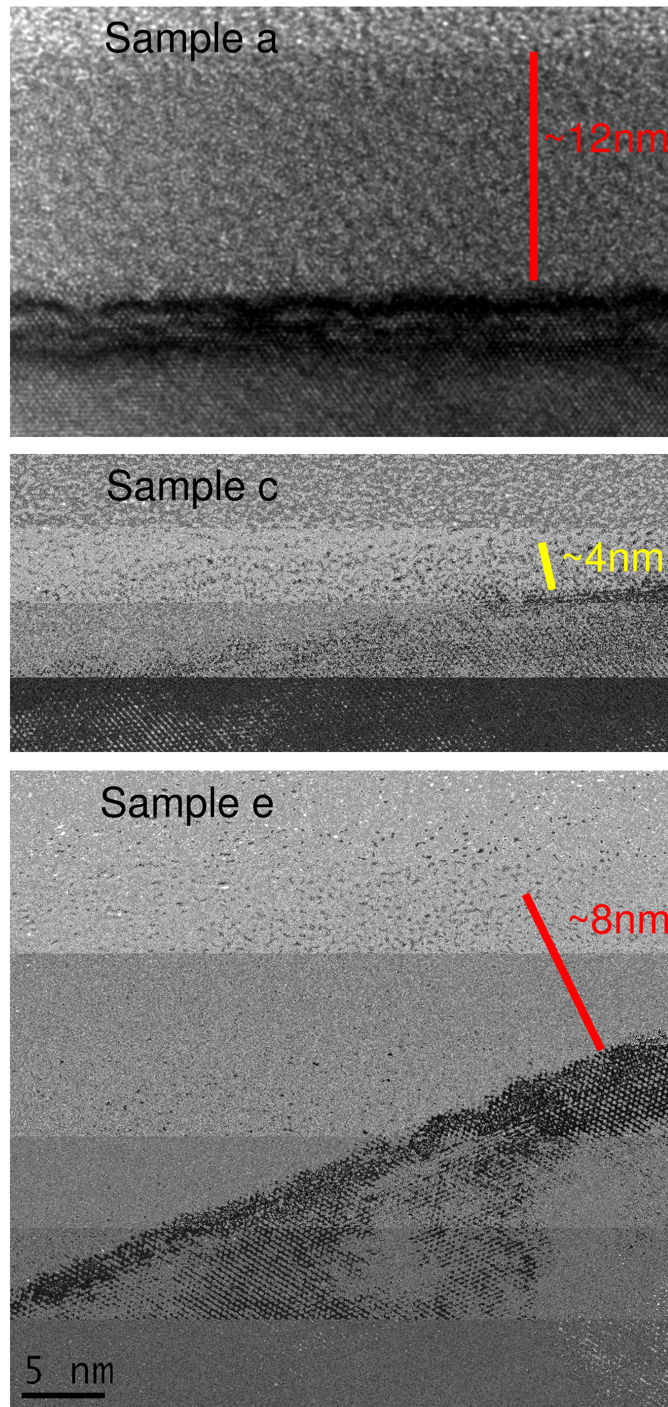

Figure 7.5: Amorphous Si layer thicknesses of Samples a, c, and e. The thickness is greatly reduced for Sample c. However, Sample e, with minority carrier lifetimes the same as for Sample c, has a thickness equal to the nominally deposited thickness.

comparable lifetimes in Sample e are observed despite an amorphous layer of approximately 8-10nm, which is within the nominal range of the deposited thickness.

The carrier lifetimes of this set of samples are not clearly correlated with any structural properties observable by XTEM. This may be due to any one of several reasons. First, it is possible that the crystalline layer contains point defects,[9] which would not be expected to show up in images of these relatively thick (~25-50nm) TEM specimens. Another possible explanation for the varying lifetimes may lie not in the crystalline layer, but the amorphous layer. The hydrogen content and bonding within the amorphous layer should be determined, possibly by using infrared spectroscopy.[4] The increased hydrogen content at the a-Si/c-Si interface has been correlated with increased lifetime,[2] but it would also increase the disorder and the concentration of nanovoids within the amorphous layer.[2,4,6] Perhaps as the HPT time increases, the concentration of voids exceeds a critical point in which the deleterious effects of the vacancies on the sample are no longer outweighed by the commensurate disorder in the sample. It is also possible that the hydrogen content within the amorphous layer reaches saturation, and that further HPT simply serves to increase the concentration of voids. Regarding this latter point, it is noteworthy in figure 7.1, that the length of HPT needed to reach maximum carrier lifetime is different for samples with and without the SiO_x capping layer. If hydrogen is reaching saturation at or near the point of maximum carrier lifetime, then it may well be that hydrogen in-diffusion occurs more easily in samples without the SiO_x capping layer.

Finally, the role of interface charge on passivation, and consequently on lifetime, could be investigated, possibly using electron holography. The lifetimes within samples with the SiO_x capping layer were higher than those without the capping layer. Physical

protection from etching the amorphous layer is not a readily apparent explanation since the thickness of the amorphous layer does not appear to have been reduced by HPT in samples with the capping layer. However, SiO_x is an insulator, so it may be relevant to determine whether there is a component of field-effect passivation in addition to the chemical passivation.

7.4 Conclusions

a-Si/*c*-Si samples with and without SiO_x capping layers were treated by hydrogen plasma for different amounts of time and then investigated using XTEM. The amorphous layer of the uncapped sample with the smallest minority carrier lifetime was thinner than observed for the other samples, but no apparent crystalline damage was observed. No other differences between the samples were identified that could explain the differences in lifetimes. Next steps should include infrared spectroscopy to determine the hydrogen content and bonding structure within the amorphous layer, and electron holography could be used to estimate the interface charge.

References

1. Płaczek-Popko, E. 2017. *Opto-Electronics Review* **25**: 55.

2. Mews, M., Schulze, T.F., Mingirulli, N., and Korte, L. 2013. *Applied Physics Letters* **102**: 122106.

3. Descoeudres, A., Barraud, L., Bartlome, R., Choong, G., De Wolf, S., Zicarelli, F., and Ballif, C. 2010. *Applied Physics Letters* **97**: 183505.

4. Descoeudres, A., Barraud, L., De Wolf, S., Strahm, B., Lachenal, D., Guerin, C., Holman, Z.C., Zicarelli, F., Demaurex, B., Seif, J., Holovsky, J. and Ballif, C. 2011. *Applied Physics Letters* **99**: 123506.

5. Guo, Y., Ong, T.M.B., Levchenko, I., and Xu, S. 2018. *Applied Surface Science* **427**: 486.

6. Geissbühler, J., De Wolf, S., Demaurex, B., Seif, J.P., Alexander, D.T.L., Barraud, L., and Ballif, C. 2013. *Applied Physics Letters* **102**: 231604.

7. He, J., Li, W., Wang, Y., Mu, J., An, K., and Chou, X. 2015. *Materials Letters* **161**: 175.

8. Kaïl, F., Fontcuberta I Morral, A., Hadjadj, A., Roa I Cabarrocas, P., and Beorchia, A. 2006. *Philosophical Magazine* **84**: 595.

9. Simoen, E., Radhakrishnan, H.S., Uddin, M.G., Gordan, I., Poortmans, J., Wang, C., and Li, W. 2018. *Journal of Vacuum Science & Technology B* **36**: 041201.

CHAPTER 8

SUMMARY AND FUTURE WORK

The research in this dissertation has involved the characterization of several materials combinations that offer much potential for improving the overall efficiency of photovoltaic solar cells. The material systems investigated include Si, Ge, and combinations of III-V semiconductors. This chapter summarizes the major results of these studies and discusses promising avenues for future research.

8.1 Summary

Two studies revolved around the improvement of passivation in silicon heterojunction (SHJ) solar cells. Hydrogen plasma treatment (HPT) has been shown to improve the passivation of *a*-Si layers in SHJ solar cells,[1] but material can also be etched away during processing.[2] High-resolution TEM observations revealed no obvious structural differences between specimens that would account for the strong differences in minority carrier lifetimes. This key result suggested that other factors such as point defects, hydrogen content, or interface charge must be affecting these minority carrier lifetimes. In a second related study, *μc*-Si was used as an alternative to the usual *a*-Si passivation layer in SHJ solar cells in an attempt to reduce parasitic absorption.[3] The TEM images revealed that the *μc*-Si layer in samples grown by plasma-enhanced CVD followed undesired amorphous growth. Seeding the *μc* growth with nanoparticles initiated the growth at the interface with the underlying layer. However, amorphous material was observed above the crystallites, indicating that further adjustments to the growth procedure would be necessary. Correlation of TEM images with three-

dimensional techniques to determine the percent crystallinity of the *μc*-Si layer eliminated ellipsometry as a reliable method for this task, although qualitative agreement was found between TEM and UV Raman spectroscopy.[4]

In addition to Si-based solar cells, the growth of III-V materials for photovoltaic applications was also investigated. Epitaxial layers of the compound semiconductor GaP can be grown on bulk Si substrates with a lattice mismatch of only 0.36%, and additional III-V materials could then be grown on the composite GaP/Si, enabling the possibility of multijunction solar cells covering a range of band-gap energies.[5-7] The crystallinity and defect structures in GaP layers of varying thickness grown on Si were examined by cross-sectional TEM for comparison with results from Xray diffraction (XRD). Defects were present in all examined layers, even for GaP thicknesses as small as 37nm. Defect density increased significantly as layer thickness was increased from 37nm to 250nm, indicating that GaP layers with thicknesses of 250nm and above should not be considered as viable virtual substrates for further III-V growth.[8] Radiative recombination in photovoltaic materials can occur not only at dislocations, but also at antiphase boundaries (APBs), which appear within III-V layers grown on IV substrates.[9,10] Observations by aberration-corrected STEM revealed antiphase boundaries arising from GaP/Si interfaces that were neither atomically flat nor abrupt for samples grown either by molecular beam epitaxy or by migration-enhanced epitaxy. Traditional understanding of APB formation allows for Si migration into only one atomic layer above the original Si surface,[11] an idea which was strongly contradicted by these atomically-resolved images.

A second study involving III-V photovoltaic materials investigated InAs quantum dots with GaAsSb spacer layers of differing thicknesses for applications as intermediate-

band solar cells (IBSC).[12] An IBSC has the potential to increase solar-cell efficiency by absorbing photons with energies lower than the traditional band gap.[13] TEM images were used in conjunction with photoluminescence (PL) and XRD to determine the optimum thickness of the spacer layers. Plan-view images revealed the termination of some threading dislocations in a sample with spacer-layer thicknesses of 2nm, with an estimated defect density of ~10^{10}cm^{-2}. In contrast, a sample with 15-nm-thick spacer layers showed a dense, cross-hatched pattern, indicating much poorer quality growth overall. Corresponding cross-sectional TEM images of samples with 5-nm and 10-nm spacer-layer thicknesses showed less undulation in the layers in the latter sample. These TEM observations supported PL and XRD results, which had indicated that GaAsSb spacer layers with thicknesses of 10nm, between InAs quantum dots, yielded the highest quality material for device purposes.[12]

Finally, metal-induced crystallization (MIC) of Ge and Al/Ge layer exchange were studied. Ge has a lower band-gap energy than Si, and a hole mobility more than four times greater.[14] MIC and layer exchange promise an inexpensive way to grow high quality Ge layers.[15] However, the details of the exchange mechanism are still largely unknown, providing motivation for the investigation. Several Al/Ge samples were annealed under different conditions with the goal of initiating MIC and layer exchange. However, only two of the samples definitively exhibited both Ge crystallization and layer exchange, and both processes were incomplete in both samples. Both had been annealed at 400°C for 4 hours, yet a third sample annealed under these exact same conditions did not exhibit layer exchange, and crystallization of this sample was inconclusive. Moreover, neither MIC nor layer exchange could be correlated with oxidation before annealing,

since the samples in which layer exchange occurred had been oxidized for 3 hours and 10 days, respectively, while a third sample that had been oxidized for 6 days did not exhibit layer exchange, and crystallization of this third sample was inconclusive. Ultimately, the results of this study were inconclusive since no reliable path towards layer exchange and crystallization had been established.

8.2 Future work

These studies suggest several opportunities for improvements in solar-cell materials that would be worthwhile pursuing in the future.

8.2.1 Dilute nitrides

The epitaxial GaP layers grown Si substrates exhibited structural defects such as dislocations even in layers that were only 37nm thick, despite the lattice mismatch with Si of only 0.36%. In order to grow higher quality III/V material on Si, it would be preferable to eliminate the mismatch altogether. One way to accomplish zero mismatch is by using what are often called dilute nitrides. Basically, these are tertiary III/V materials in which there are two group V elements, with one of them being nitrogen in small quantities (~2-3%). Incorporation of nitrogen would affect the band structure, specifically the conduction band, of the composite material due to the smaller size and greater electronegativity of nitrogen relative to other group V materials.[16]

In order to predict and control the effect of doping with any level of confidence, it is essential to accurately quantify the nitrogen concentration. One as-yet-unanswered question is the determination of the relative concentrations of interstitial and

substitutional nitrogen in these nitrides. In previous work, it was found that HAADF images showed brighter $GaAs_{1-x}N_x$ layer than neighboring GaAs layers.[17] Because intensities in HAADF increase proportionally with Z raised to some exponential power, typically between 1.5 and 2, a $GaAs_{1-x}N_x$ layer in which the N is purely substitutional should appear less bright than GaAs. The observed brighter layer would seem to indicate the presence of nitrogen in interstitial positions. This hypothesis was furthered by the observation of microcracking in the dilute nitride with the highest N concentration, which was attributed to the strain due to excessive interstitial nitrogen.[17]

Other workers have attempted to explain the unexpected contrast by appealing to strain instead of interstitial nitrogen.[18,19] One study reported a reversal in expected relative intensities for inner ADF detector semi-angles of up to 65 mrad.[18] Misfit strain alone could not account for this phenomenon since simulated images that included local strain, arising from the smaller volume occupied by substitutional nitrogen than its arsenide counterpart, reasonably matched experimental image contrast.[18] In another study, nitrogen concentration was measured by imaging at different camera lengths, taking strain into account using smaller collection angles and using that information to quantify nitrogen concentration from intensities in images using larger collection angles.[19] However, these studies only addressed the effects of substitutional nitrogen, leaving unexplored the possibility that interstitial nitrogen could account for much of the difference remaining between simulated and experimental results.

Determining the respective concentrations of substitutional and interstitial nitrogen is far from trivial. If spectroscopy could be used, it would appear that the subsequent calculations would be simple. For example, subtracting the As concentration

from the Ga concentration should yield the substitutional N concentration, and subtracting this value from the total N concentration should then yield the interstitial N concentration. However, the concentration of nitrogen in dilute nitrides is sufficiently small (~1-3%) and the uncertainty in spectroscopic measurements is sufficiently large (± 1-3%) that it does not appear realistic to determine N concentrations by this method.

It might be possible for density functional theory (DFT) calculations to predict whether the electronic structure of substitutional nitrogen is sufficiently different from interstitial nitrogen to detect the difference using EELS. If the two structures are different, then the concentrations could be determined directly by comparing EELS spectra to DFT simulations.

Another possible method to determine how much nitrogen is substitutional and how much is interstitial is through measurement of strain. Strain was measured in dilute InAsBi ternary alloys by using the Geometric Phase Analysis (GPA) software to analyze TEM images, and then comparing the lattice constant of the dilute Bi to a reference material.[19] In that case, the GPA study was possible because Bi atoms were larger than As atoms, which increased the lattice constant and created tensile strain.[20] In the case of dilute nitrides, N atoms are smaller than As, and the altered lattice constant should create compressive strain. This strain could also be analyzed using GPA in a fashion similar to the dilute bismide measurements, and amount of substitutional nitrogen quantified.

Finally, large-angle bright-field (LABF) STEM images have been shown to exhibit atomic-number (Z) contrast, similar to HAADF images. Although the Z-dependence is less for LABF than for HAADF, the visibility of lower-Z elements such as nitrogen in LABF would be improved relative to HAADF.[21] It is not yet known whether

LABF would exhibit the same relative contrast reversal as previous HAADF studies, but such an experiment would add to the body of knowledge about LABF, and the results should also contribute to a better determination of interstitial and substitutional nitrogen in dilute nitrides.

8.2.2 Electron holography characterization of *a*-Si/*c*-Si

Structural differences were expected between *a*-Si/*c*-Si samples undergoing hydrogen plasma treatments to account for differences in minority carrier lifetimes. This was based in part on the expectation that chemical passivation was the primary driver of lifetime differences. Since no structural differences were observed, it would be of interest to determine whether field-effect passivation plays a role. Electron holography could be used in this determination.

In the off-axis electron holography technique, part of the incoming coherent electron wave is incident on a sample while the other part passes through the neighboring vacuum.[22] A biased electrostatic biprism located farther down the microscope lens column causes these waves to overlap, producing an interference pattern. The phase change of the part of the wave passing through the sample relative to vacuum provides quantitative information about the local electrostatic potential within the sample.[22]

The energy-band structure of an insulator-semiconductor interface is curved in the semiconductor layer at and near the interface.[23] Since energy is proportional to electrostatic potential, and the derivative of potential is electric field, the changing slope of curved energy bands would indicate a changing electric field. The presence of this field could imply field-effect passivation. If electrostatic potential profiles generated from

electron holograms showed curves at the SiO_x/*a*-Si interface of samples with capping layers but not at the *a*-Si surface of samples without capping layers, then field-effect passivation would be even more likely.

References

1. Mews, M., Schulze, T.F., Mingirulli, N., and Korte, L. 2013. *Applied Physics Letters* **102**: 122106.

2. Geissbühler, J., De Wolf, S., Demaurex, B., Seif, J.P., Alexander, D.T.L., Barraud, L., and Ballif, C. 2013. *Applied Physics Letters* **102**: 231604.

3. Seif, J.P., Descoeudres, A., Nogay, G., Hänni, S., de Nicolas, S.M., Holm, N., Geissbühler, J., Hesser-Wyser, A., Duchamp, M., Dunin-Borkowski, R.E., Ledinsky, M., De Wolf, S., and Ballif, C. 2016. *IEEE Journal of Photovoltaics* **6**: 1132.

4. Carpenter, J.V. III, Bailly, M., Boley, A., Shi, J., Minjares, M., Smith, D.J., Bowden, S., and Holman, Z.C. 2017. *Physica Status Solidi B* **254**: 1700204.

5. New Semiconductor Materials Characteristics and Properties. 2001. Ioffe Physico-Technical Institute.

6. Németh, L., Kunert, B., Stolz, W., and Volz, K. 2008. *Journal of Crystal Growth* **310**: 4763.

7. Romanyuk, O., Supplie, O., Susi, T. May, M.M., and Hannappel, T. 2016. *Physical Review B* **94**: 155309.

8. Zhang, C., Boley, A., Maroc, A., Faleev, N., Smith, D.J., and Honsberg, C.B. 2018. *Journal of Crystal Growth* **503**: 36.

9. Beyer, A., Németh, I., Liebich, S., Ohlmann, J., Stolz, W., and Voltz, K. 2011. *Journal of Applied Physics* **109**: 083529.

10. Kroemer, H. 1987. *Journal of Crystal Growth* **81**: 193.

11. Romanyuk, O., Supplie, O., Susi, T. May, M.M., and Hannappel, T. 2016. *Physical Review B* **94**: 155309.

12. Kim, Y., Ban, K.-Y., Boley, A., Smith, D.J., and Honsberg, C.B. 2015. *Applied Physics Letters* **107**: 173109.

13. Luque, A., Martí, A., and Stanley, C. 2012. *Nature Photonics* **6**, 146.

14. Bosi, M. and Attolini, G. 2010. *Progress in Crystal Growth and Characterization of Materials* **56**: 146.

15. Slaoui, A., Pathi, P. and Tuzun, Ö. 2015. "Aluminum-Induced Crystallization: Applications in Photovoltaic Technologies" in Wang, Z. et al., Eds. *Metal-*

Induced Crystallization: Fundamentals and Applications. Singapore: Pan Stanford Publishing.

16. O'Reilly, E.P., Lindsay, A., Klar, P.J., Polimeni, A., and Capizzi, M. 2009. *Semiconductor Science and Technology* **24**: 033001.

17. Tang, D. 2014. *Characterization of MBE-grown Semiconductor Materials for Photovoltaic Applications* [Thesis]. Arizona State University.

18. Wu, X., Robertson, M.D., Gupta, J.A., and Baribeau, J.-M. 2008. *Journal of Physics: Condensed Matter* **20**: 075215.

19. Grieb, T., Müller, K., Fritz, R., Grillo, V., Schowalter, M., Voltz, K., and Rosenauer, A. 2013. *Ultramicrocsopy* **129**: 1.

20. Lu, J. 2017. *Evaluation of Compound Semiconductors for Infrared Photo-Detection Applications* [Thesis]. Arizona State University.

21. Aoki, T., Lu, J., McCartney, M.R., and Smith, D.J. 2016. *Semiconductor Science and Technology* **31**: 094002.

22. McCartney, M.R. and Smith, D.J. 2007. *Annu. Rev. Mater. Res.* 37:729-67.

23. Misra, V. and Öztürk, M.C. 2005. "Field Effect Transistors" in Chen, W.-K. *The Electrical Engineering Handbook*. Burlington: Elsevier Academic Press.

LIST OF REFERENCES

Abate, A. 2017. *Joule* **1**: 659.

Anderson, R. and Klepeis, S.J. 2005. "Practical aspects of FIB TEM specimen preparation," in Eds. Giannuzzi, L.A. and Stevie, F.A. *Introduction to Focused Ion Beams: Instrumentation, Theory, and Practice*. Boston: Springer.

Aoki, T., Lu, J., McCartney, M.R., and Smith, D.J. 2016. *Semiconductor Science and Technology* **31**: 094002.

Ayers, J. E. 2007. *Heteroepitaxy of Semiconductors: Theory, Growth, and Characterization*. Boca Raton: CRC Press.

Ballif, C., Descoeudres, A., and DeWolf, S. 2012. Reproduced in Ecole Polytechnique Federale de Lausanne, "Using amorphous and monocristalline silicon together, researchers set new efficiency record for photovoltaic cells." Omnicron Tech Ltd: Phys.org.

Beyer, A., Németh, I., Liebich, S., Ohlmann, J., Stolz, W., and Voltz, K. 2011. *Journal of Applied Physics* **109**: 083529.

Beyer, A., Ohlmann, J., Liebich, S., Heim, H., Witte, G., Stolz, W., and Volz, K. 2012. *Journal of Applied Physics* **111**: 083534.

Beyer, A., Stegmüller, A., Oelerich, J.O., Jandieri, K., Werner, K., Mette, G., Stolz, W., Baranovskii, S.D., Tonner, R., and Voltz, K. 2016. *Chemistry of Materials* **28**: 3265.

Bosi, M. and Attolini, G. 2010. *Progress in Crystal Growth and Characterization of Materials* **56**: 146.

Bosi, M. and Pelosi, C. 2007. *Progress in Photovoltaics: Research and Applications* **15**: 51.

Brown, M. 2017. "Solar Lanterns Serve as Beacon of Hope for Puerto Rico," Sierra. Sierra Club.

Bruice, P.Y. 2004. *Organic Chemistry, 4th Edition*. Upper Saddle River: Prentice Hall.

Buller, S. and Strunk, J. 2016. *Journal of Energy Chemistry* **25**: 171.

Bye, G. and Ceccaroli, B. 2014. *Solar Energy Materials & Solar Cells* **130**: 634.

Carlsson, J.-O., Martin, P.M. 2009. "Chemical vapor deposition," in Ed. Martin, P.M. *Handbook of Deposition Technologies for Films and Coatings: Science, Applications and Technology*. Elsevier.

Carpenter, J.V. III, Bailly, M., Boley, A., Shi, J., Minjares, M., Smith, D.J., Bowden, S., and Holman, Z.C. 2017. *Physica Status Solidi B* **254**: 1700204.

Carpenter, J., Bailly, M., Bowden, S., and Holman, Z. 2015. "Characterization of Microcrystalline Silicon in Heterojunction Solar Cells" [Poster]. QESST Site Visit, Arizona State University.

Chen, M. and Blankenship, R.E. 2011. *Trends in Plant Science* **16**: 427.

Cohen, D., McKernan, S., and Carter, C.B. 1999. *Microscopy & Microanalysis* **5**: 173.

Collins, R., Ferlauto, A., Ferreira, G., Chi Chen, J.K., Kova, R., Lee, Y., Pearce, J., and Wronski, C. 2003. *Solar Energy Materials & Solar Cells* **78**: 143.

Correa-Baena, J.P., Abate, A., Saliba, M., Tress, W., Jacobsson, T.J., and Grätzel, M., Hagfeldt, A. 2017. *Energy & Environmental Science* **10**: 710.

Cowley, J.M. 1988. "Imaging," in Ed. Cowley, J.M. *High-Resolution Transmission Electron Microscopy and Associated Techniques.* New York: Oxford University Press.

Demtchelis, F., Pirri, C.F., and Tresso, E. 1993. *Philosophical Magazine B* **67**: 331.

Descoeudres, A., Barraud, L., Bartlome, R., Choong, G., De Wolf, S., Zicarelli, F., and Ballif, C. 2010. *Applied Physics Letters* **97**: 183505.

Descoeudres, A., Barraud, L., De Wolf, S., Strahm, B., Lachenal, D., Guerin, C., Holman, Z.C., Zicarelli, F., Demaurex, B., Seif, J., Holovsky, J. and Ballif, C. 2011. *Applied Physics Letters* **99**: 123506.

Diodes, LEDs and Solar Cells. 2015. *Inorganic Chemistry LibreTexts*

Dixit, V.K., Ganguli, T., Sharma, T.K., Singh, S.D., Kumar, R., Porwal, S., Twiari, P., Ingale, A., and Oak, S.M. 2008. *Journal of Crystal Growth* **310**: 3428.

Döscher, H., Supplie, O., Brückner, S., Hannappel, T., Beyer, A., Ohlmann, J., and Voltz, K. 2011. *Journal of Crystal Growth* **315**: 16.

Environmental Defense Fund. 2017. Now Hiring: The Growth of America's Clean Energy & Sustainability Jobs. p 4.

Executive Office of the President. 2013. The Presdient's Climate Action Plan. p 6.

Fahrenbruch, A.L. and Bube, R.H. 1983. *Fundamentals of Solar Cells*. New York: Academic Press.

Feifel, M. 2017. *IEEE Journal of Photovoltaics* **7**: 502.

Feifel, M., Ohlmann, J., Benick, J., Rachow, T., Janz, S., Hermle, M., Dimroth, F., Belz, J., Beyer, A., Volz, K., and Lackner, D. 2017. *IEEE Journal of Photovoltaics* **7**: 502.

"Flow Rate Modulated Vapor Epitaxy." 2001. In *Encyclopedia of Materials: Science and Technology*. Elsevier.

Franchi, S. 2013. "Molecular beam epitaxy: fundamentals, historical background and future prospects," in Ed. Henini, M. *Molecular Beam Epitaxy*. Elsevier.

Friedman, D.J. 2010. *Current Opinion in Solid State and Materials Science* **14**: 131.

Fu, R., et al. 2017. U.S. Solar Photovoltaic System Cost Benchmark: Q1 2017. National Renewable Energy Laboratory. p 49.

Ganapati, V., Miller, O.D., and Yablonovitch, E. 2014. *IEEE Journal of Photovoltaics* **4**: 175.

Garcia, I., France, R.M., Geisz, J.F., McMahon, W.E., Steiner, M.A., Johnston, S., and Friedman, D.J. 2016. *IEEE Journal of Photovoltaics* **6**: 366.

Geissbühler, J., De Wolf, S., Demaurex, B., Seif, J.P., Alexander, D.T.L., Barraud, L., and Ballif, C. 2013. *Applied Physics Letters* **102**: 231604.

Gianuzzi, L.A., Kempshall, B.W., Schwartz, S.M., Lomness, J.K., Prenitzer, B.I., and Stevie, F.A. 2005. "FIB lift-out specimen preparation techniques: ex-situ and in-situ methods," in Eds. Giannuzzi, L.A. and Stevie, F.A. *Introduction to Focused Ion Beams: Instrumentation, Theory, and Practice*. Boston: Springer.

Gilliland, G.D. 1997. *Materials Science and Engineering* **R18**: 99.

Grieb, T., Müller, K., Fritz, R., Grillo, V., Schowalter, M., Voltz, K., and Rosenauer, A. 2013. *Ultramicrocsopy* **129**: 1.

Griffiths, D.J. 2017. *Introduction to Electrodynamics, 4th Edition*. Cambridge: Cambridge University Press.

Guo, Y., Ong, T.M.B., Levchenko, I., and Xu, S. 2018. *Applied Surface Science* **427**: 486.

Halliday, D., et al. 2008. *Fundamentals of Physics, 8th Edition*. [city]: John Wiley & Sons, Inc.

He, D., Wang, J.Y., and Mittemeijer, E.J. 2006. *Scripta Materialia* **54**: 559.

He, J., Li, W., Wang, Y., Mu, J., An, K., and Chou, X. 2015. *Materials Letters* **161**: 175.

Hess, D.W. 1986. *Annual Review of Materials Research* **16**: 163.

Holdford, B. 2005. “Uses of dualbeam FIB in microelectronic failure analysis,” in Eds. Giannuzzi, L.A. and Stevie, F.A. *Introduction to Focused Ion Beams: Instrumentation, Theory, and Practice*. Boston: Springer.

Holman, Z.C., Descoeudres, A., Barraud, L., Fernandez, F.Z., Seif, J.P., De Wolf, S., and Ballif, C. 2012. *IEEE Journal of Photovoltaics* **2**: 7.

Honsberg, C. and Bowden, S. 2017. Absorption Coefficient. PVEducation.org

Ibach, H. and Lueth, H. *Solid-State Physics*. Springer Verlag, 2003

John, N., and George, S. 2017. “Raman Spectroscopy,” in Eds. Thomas, S., Thomas, R., Zachariah, A.K., and Mishra, R.K. *Spectroscopic Methods for Nanomaterials Characterization*. Cambridge: Elsevier.

Kaïl, F., Fontcuberta I Morral, A., Hadjadj, A., Roa I Cabarrocas, P., and Beorchia, A. 2006. *Philosophical Magazine* **84**: 595.

Kim, S., Jung, Y., Kim, J.J., Lee, S., and Lee, H. 2015. *Journal of Alloys and Compounds* **518**: 545.

Kim, Y., Ban, K.-Y., Boley, A., Smith, D.J., and Honsberg, C.B. 2015. *Applied Physics Letters* **107**: 173109.

Kroemer, H. 1987. *Journal of Crystal Growth* **81**: 193.

Ledentsov, N.N., Ustinov, V.M., Shchukin, V.A., Kop’ev, P.S., Alferov, Z.I., and Bimberg, D. 1998. *Semiconductors* **32**: 343.

Leng, Y. 2013. *Materials Characterization: Introduction to Microscopic and Spectroscopic Methods, 2nd Ed.* Weinheim: Wiley-VCH.

Li, Q. and Lau, K.M. 2017. *Progress in Crystal Growth and Characterization of Materials* **63**: 105.

Lu, J. 2017. *Evaluation of Compound Semiconductors for Infrared Photo-Detection Applications* [Thesis]. Arizona State University.

Lucci, I., Charbonnier, S., Pedesseau, L., Vallet, M., Cerutti, L., Rodriguez, J.-B., Tournié, E., Bernard, R., Létoublon, A., Bertru, N., Le Corre, A., Rennesson, S., Semond, F., Patriarche, G., Largeau, L., Turban, P., Ponchet, A., and Cornet, C. 2018. *Physical Review Materials* **2**: 060401(R).

Luna, E., Guzmán, A., Trampert, A., and Álvarez, G. 2012. *Physical Review Letters* **109**: 126101.

Luque, A. 2011. *Journal of Applied Physics* **110**: 031301.

Luque, A. and Martí, A. 1997. *Physical Review Letters* **78**, 5014.

Luque, A., Marti, A., and Stanley, C. 2012. *Nature Photonics* **6**, 146.

Luque, A., Martí, A., Stanley, C., Lopez, N., Cuadra, L., Zhou, D., Pearson, J.L., and McKee, A. 2004. *Journal of Applied Physics* **96**, 903.

Maros, A., Faleev, N., King, R.R., Honsberg, C., Convey, D., Xie, H., and Ponce, F.A. 2016. *Journal of Vacuum Science and Technology* **34**: 02L113.

McAlister, A.J. and Murray, J.L. 1984. *Bulletin of Alloy Phase Diagrams* **5**: 341.

McCartney, M.R. and Smith, D.J. 2007. *Annu. Rev. Mater. Res.* 37:729-67.

McCluskey, M.D. and Haller, E.E. 2012. *Dopants and Defects in Semiconductors*. Boca Raton: CRC Press.

Mews, M., Schulze, T.F., Mingirulli, N., and Korte, L. 2013. *Applied Physics Letters* **102**: 122106.

Misra, V. and Öztürk, M.C. 2005. "Field Effect Transistors" in Chen, W.-K. *The Electrical Engineering Handbook*. Burlington: Elsevier Academic Press.

National Renewable Energy Laboratory. Reference Solar Spectral Irradiance: Air Mass 1.5.

National Renewable Energy Laboratory. 2017. Best Research-Cell Efficiencies.

Nellist, P.D. 2011. In Eds. Pennycook, S.J. and Nellist, P.D. *Scanning Transmission Electron Microscopy: Imaging and Analysis*. New York: Springer.

Nelson, J. 2003. *The Physics of Solar Cells*. London: Imperial College Press.

Németh, I., Kunert, B., Stolz, W., and Voltz, K. 2008. *Journal of Crystal Growth* **310**: 1595.

New Semiconductor Materials Characteristics and Properties. 2001. Ioffe Physico-Technical Institute.

Nishida, T., Mmoto, K., Saitoh, N., Yoshizawa, N., Suemasu, T., and Toko, K. 2019. *Applied Physics Letters* **114**: 142103.

Nozik, A.J. 2002. *Physica E* **14**, 115.

Office of Chief Financial Officer. 2015. Department of Energy FY 2016 Congressional Budget Report. p 15.

Office of Chief Financial Officer. 2018. Department of Energy FY 2018 Congressional Budget Request. p 1.

O'Reilly, E.P., Lindsay, A., Klar, P.J., Polimeni, A., and Capizzi, M. 2009. *Semiconductor Science and Technology* **24**: 033001.

Pagliaro, M., Palmisano, G., and Ciriminna. R. 2008. *Flexible Solar Cells*. Palermo: Wiley-VGH, Weinheim.

Park, N.-G. 2015. *Materials Today* **18**: 65.

Pennycook, S.J. 2012. *Ultramicroscopy* **123**: 28.

Phaneuf, M.W. 2005. "FIB for materials science applications – a review," in Eds. Giannuzzi, L.A. and Stevie, F.A. *Introduction to Focused Ion Beams: Instrumentation, Theory, and Practice*. Boston: Springer.

Ping Wang, Y., Stodolna, J., Bahri, M., Kuyyalil, J., Thanh, T.N., Almosni, S., Bernard, R., Tremblay, R., Da Silva, M., Léroublon, A., Rohel, T., Tavernier, K., Largeau, L., Patriarche, G., Le Corre, A., Ponchet, A., Magen, C., Corent, C., and Durand, O. 2015. *Applied Physics Letters* **107**: 191603.

Płaczek-Popko, E. 2017. *Opto-Electronics Review* **25**: 55.

Podraza, N.J. and Jellison, G.E., Jr. 2017. In Eds. Lindon, J.C., Tranter, G.E., and Koppenaal, D.W. *Encyclopedia of Spectrsocopy and Spectrometry, 3rd Ed.* Oxford: Elsevier Ltd.

Prohl, C., Döscher, H., Kleinschmidt, P., Hannappel, T., and Lenz, A. 2016. *Journal of Vacuum Science & Technology A: Vacuum, Surface, and Films* **34**: 031102.

Ramanujam, J., 2016. *Progress in Materials Science* **82**: 294.

Ratcliff, C., Grassman, T.J., Carlin, J.A., and Ringel, S.A. 2011. *Applied Physics Letters* **99**: 141905.

Romanyuk, O., Supplie, O., Susi, T. May, M.M., and Hannappel, T. 2016. *Physical Review B* **94**: 155309.

Rubel, O. and Baranovskii, S.D. 2009. *International Journal of Molecular Sciences* **10**: 5104.

Sain, T., Singh, C.K., Ilango, S., and Mathews, T. 2019. *Journal of Applied Physics* **126**: 125303.

Seif, J.P., Descoeudres, A., Nogay, G., Hänni, S., de Nicolas, S.M., Holm, N., Geissbühler, J., Hesser-Wyser, A., Duchamp, M., Dunin-Borkowski, R.E., Ledinsky, M., De Wolf, S., and Ballif, C. 2016. *IEEE Journal of Photovoltaics* **6**: 1132.

Shockley, W. and Queisser, H.J. 1961. *Journal of Applied Physics* **32**: 510.

Shockley, W. and Read, W.T., Jr. 1952. *Physical Review* **87**: 835.

Siebentritt, S. 2017. In Eds. Reinders, A., Verlinden, P., van Sark, W., and Freundlich, A. *Photovoltaic Solar Energy: From Fundamentals to Applications*. West Sussex: Wiley.

Simoen, E., Radhakrishnan, H.S., Uddin, M.G., Gordan, I., Poortmans, J., Wang, C., and Li, W. 2018. *Journal of Vacuum Science & Technology B* **36**: 041201.

Slaoui, A., Pathi, P. and Tuzun, Ö. 2015. "Aluminum-Induced Crystallization: Applications in Photovoltaic Technologies" in Wang, Z. et al., Eds. *Metal-Induced Crystallization: Fundamentals and Applications*. Singapore: Pan Stanford Publishing.

Smith, D.J. 2008. *Microscopy & Microanalysis* **14**: 2.

Smith, D.J., Aoki, T., Mardingly, J., Zhou, L., and McCartney, M.R. 2013. *Microscopy* **62**(Supplement 1): S65.

Smith, D.J., Cullen, D.A., Zhou, L., and McCartney, M.R. 2010. *Microelectronics Reliability* **50**: 1514.

Song, Z., Watthage, S.C., Phillips, A.B., and Heben, M.J. 2016. *Journal of Photonics for Energy* **6**: 022001.

Spence, J.C.H. 2013. *High Resolution Electron Microscopy. 3rd Ed.* Oxford: Oxford University Press.

Stephen, M., Genevicius, K., Juska, G., Arlauskas, K., and Hiorns, R.C. 2017. *Polymer International* **66**: 13.

Tang, D. 2014. *Characterization of MBE-grown Semiconductor Materials for Photovoltaic Applications* [Thesis]. Arizona State University.

Tea, E., Vidal, J., Pedesseau, L., Cornet, C., Jancu, J.-M., Even, J., Laribi, S., Guillemoles, J.-F., and Durand, O. 2014. *Journal of Applied Physics* **115**: 063502.

Tiwari, G.N. and Mishra, R.K. 2011. *Advanced Renewable Energy Sources*. Cambridge: Royal Society of Chemistry.

Toudert, J. 2014. *Nanotechnology Reviews* **3**: 223.

Tsao, J.Y., Dodson, B.W., Picraux, S.T., Cornelison, D.M. 1987. *Physical Review Letters* **59**: 2455.

U.S. Energy Information Administration. 2017. Monthly Energy Review, December 2017. p 3.

U.S. Energy Information Administration. 2018. Monthly Energy Review, March 2018. p 3.

U.S. Energy Information Administration. 2016. International Energy Outlook 2016. pp 7-9.

Voltz, K., Beyer, A., Witte, W., Ohlmann, J., Németh, I., Kunert, B. and Stolz, W. 2011. *Journal of Crystal Growth* **315**: 37.

Wahnón, P. and Tablero, C. 2002. *Physical Review B* **65**, 155115.

Wang, J.Y., He, D., Zhao, Y.H., and Mittemeijer, E.J. 2006. *Applied Physics Letters* **88**: 061910.

Wang, Y.P., Letoublon, A., Thanh, T.N., Bahri, M., Largeau, L., Patriarche, G., Cornet, C., Bertru, N., Le Corre, A., and Durand, O. 2015. *Journal of Applied Crystallography* **48**: 702.

Wang, Z.M., Wang, J.Y., Jeurgens, L.P.H., and Mittemeijer, E.J. 2006. *Scripta Materialia* **55**: 987.

Williams, D.B., and Carter, C.B. 2009. *Transmission Electron Microscopy*. New York: Springer.

Wolf, M. 1960. *Proceedings of the IRE* **48**, 1246.

World Food Programme. mobile Vulnerability Analysis Mapping (mVAM).

Wu, J.-B., Lin, M.-L., Cong, X., Liu, H.-N., and Tan, P.-H. 2018. *Royal Society of Chemistry* **47**: 1822.

Wu, X., Robertson, M.D., Gupta, J.A., and Baribeau, J.-M. 2008. *Journal of Physics: Condensed Matter* **20**: 075215.

Würfel, P. and Würfel, U. 2016. *Physics of Solar Cells: From Basic Principles to Advanced Concepts*. Weinheim: Wiley-VCH Verlag GmbH & Co.

Yamane, K., Kawai, T., Furukawa, Y., Okada, H., and Wakahara, A. 2010. *Journal of Crystal Growth* **312**: 2179.

Youth with a Mission Medical Ships. 2013. Using Solar Power to Bring Light and Life into the Delivery Room.

Youth with a Mission Medical Ships. 2013. Solar Powered Dental Chair.

Yu, M., Long, Y.-Z., and Sun, B. 2012. *Nanoscale* **4**: 2783.

Zhang, C., Boley, A., Maroc, A., Faleev, N., Smith, D.J., and Honsberg, C.B. 2018. *Journal of Crystal Growth* **503**: 36.

Zhang, J., Zhu, L., and Wei, Z. 2017. *Small Methods* **1**: 1700258.

Zhang, X., Tan, Q.-H., Wu, J.-B., Shi, W., and Tan, P.-H. 2016. *Nanoscale* **8**: 6435.